

NUCLEOSYNTHESIS AND EVOLUTION OF MASSIVE METAL-FREE STARS

ALEXANDER HEGER

Theoretical Astrophysics Group, MS B227, Los Alamos National Laboratory, Los Alamos, NM 87545;
and Department of Astronomy and Astrophysics, University of California, Santa Cruz, CA 95064

AND

S. E. WOOSLEY

Department of Astronomy and Astrophysics, University of California, Santa Cruz, CA 95064

Draft for ApJ, October 23, 2018

ABSTRACT

The evolution and explosion of metal-free stars with masses $10 - 100 M_{\odot}$ are followed, and their nucleosynthetic yields, light curves, and remnant masses determined. Such stars would have been the first to form after the Big Bang and may have left a distinctive imprint on the composition of the early universe. When the supernova yields are integrated over a Salpeter initial mass function (IMF), the resulting elemental abundance pattern is qualitatively solar, but with marked deficiencies of odd- Z elements with $7 \leq Z \leq 13$. Neglecting the contribution of the neutrino wind from the neutron stars that they make, no appreciable abundances are made for elements heavier than germanium. The computed pattern compares favorably with what has been observed in metal-deficient stars with $[Z] \lesssim -3$. The amount of ionizing radiation from this generation of stars is ~ 2.16 MeV per baryon (4.15 B per M_{\odot} ; where 1 B = 1 Bethe = 10^{51} erg) for a Salpeter IMF, and may have played a role in reionizing the universe. Most of the stars end their lives as blue supergiants and make supernovae with distinctive light curves resembling SN 1987A, but some produce primary nitrogen by dredge up and become red supergiants. These make brighter supernovae like typical Type IIp's. For the lower mass supernovae considered, the distribution of remnant masses clusters around typical modern neutron star masses, but above $20 M_{\odot}$ to $30 M_{\odot}$, with the value depending on explosion energy, black holes are copiously formed by fallback, with a maximum hole mass of $\sim 40 M_{\odot}$. A novel automated fitting algorithm is developed for determining optimal combinations of explosion energy, mixing, and initial mass function in the large model data base to agree with specified data sets. The model is applied to the low metallicity sample of Cayrel et al. (2004) and the two ultra-iron-poor stars HE0107-5240 and HE1327-2326. Best agreement with these low metallicity stars is achieved with very little mixing, and none of the metal-deficient data sets considered show the need for a high energy explosion component. To the contrary, explosion energies somewhat less than 1.2 B seem to be preferred in most cases.

Subject headings: stars-supernovae, stars-metal poor, nucleosynthesis, supernova - light curves, black holes, neutron stars, abundances - observations

1. INTRODUCTION

There must have been a first generation of stars whose initial composition, reflecting that of the Big Bang, was essentially metal free. The term Population III is often applied to such stars (e.g., O'Shea et al. 2008). To the extent that lines of heavy elements and dust are responsible for mass loss, and in the absence of deep mixing, such stars would have lived their lives with near constant mass. As a result, the average mass at death of such stars would have been larger, even for a metallicity-independent IMF. They would also typically have been bluer stars, especially at death, and their supernovae might have been fainter. Their nucleosynthesis would also differ, at least for the many elements that are in any sense "secondary".

Such stars have been of interest for a long time (e.g., Ezer & Cameron 1971), but recent measurements suggesting the existence of stars at a very early epoch in the universe (Spergel et al. 2003; Kogut et al. 2003) have invigorated their study. So, too, have new observational data sets that highly constrain the nucleosynthe-

sis of the first few generations of stars (e.g., Cayrel et al. 2004; Lai et al. 2008) and the discovery of ultra-iron poor stars (e.g., Depagne et al. 2002; Christlieb et al. 2002; Frebel et al. 2005) which may be providing clues as to how the first generation of stars formed and exploded (e.g., Umeda & Nomoto 2003).

Zero metal stars are also a limiting case of low metallicity stars. While this is the first in a series of papers that will treat the evolution and explosion of all stars up to solar metallicity and beyond, it is expected that many of the results will apply equally well to stars of $10^{-4} Z_{\odot}$ or even $10^{-2} Z_{\odot}$, so long as mass loss remains negligible. An open issue is whether and when forms of mass loss not dependent upon atomic lines of heavy elements or grains will become important. Will $100 M_{\odot}$ zero metallicity stars near the end of their lives resemble Eta Carina? It is also uncertain just how fast this first generation of stars rotated and how rotationally induced mixing may have affected not only mass loss and nucleosynthesis, but also the presupernova structure (e.g., Meynet et al. 2006).

Here we consider a fiducial set of models whose physics is comparatively simple. The initial composition is

pristine Big Bang nucleosynthesis and mass loss is neglected at all stages of the evolution. Similarly, rotation is ignored and, along with it, any consequences of rotationally-induced mixing and strong asymmetry in the explosion. The mass range studied is $10 M_{\odot}$ to $100 M_{\odot}$. Except between $90 M_{\odot}$ and $100 M_{\odot}$, this selection avoids the complications of the pair instability on the upper end and asymptotic giant branch mass loss on the lower end. Each of these approximations is a potentially serious omission, and we hope to return with these embellishments in future works.

Other recent surveys of zero metallicity massive stars are Woosley & Weaver (1995), Marigo et al. (2001), Heger & Woosley (2002), Chieffi & Limongi (2004), Umeda & Nomoto (2005), Hirschi & et al. (2006), and Tominaga et al. (2007). This one differs in following the evolution of a large number of stars in great physical detail, from the zero age main sequence through explosion as a supernovae. A variety of supernova properties (energies, mixing, mass cut) are considered for each mass. Nucleosynthesis, supernova light curves and remnant masses are calculated. Even this “simple” study took us five years to complete. As we shall see, our simple models agree reasonably well with all the available data and make some interesting predictions. The yields of all isotopes in all stars and supernova models calculated (extended versions of Tables 7 - 14) are available in the electronic version of the paper and more detailed data including all the presupernova models and the yield data base and search tool is available online.

2. INITIAL MODELS AND PROCEDURE

2.1. Masses Studied

This study is specifically of non-rotating stars that experience iron core collapse in the end and avoid the pair instability. Because the ignition of multiple shells of nuclear burning can often lead to dramatic variation in the final stellar structure for stars that differ only slightly in initial mass (Barkat & Marom 1990), the grid of masses employed is very fine - 120 different masses in the range $10 M_{\odot}$ to $100 M_{\odot}$. Frequently, model stars differing by only $0.1 M_{\odot}$ had substantially different presupernova properties, especially towards the lighter end of the range studied. The masses of the stars studied are given in Table 1.

2.2. The Kepler Code and Adopted Physics

All calculations of evolution, nucleosynthesis, and light curves were done with the KEPLER ode. KEPLER is a one-dimensional implicit hydrodynamics package adapted to the study of stellar evolution and explosive astrophysical phenomena (Weaver et al. 1978; Woosley et al. 2002). The convective criterion is Ledoux, but with a substantial semi-convective diffusion coefficient, about 10% of the radiative diffusion coefficient in regions that are stable by the Ledoux criterion and unstable by Schwarzschild (Woosley & Weaver 1988). A small amount of convective overshooting is included by forcing convective boundary zones to be semiconvective. Opacities from the OPAL and Los Alamos tables are used wherever the helium mass fraction exceeds 10^{-5} and the temperature is less than 10^9 K. Energy generation is followed using the small 19 isotope nuclear reaction network prior to oxygen depletion, and

a 128 isotope quasi-equilibrium network thereafter as described in Weaver et al. (1978). The critical nuclear reaction rates and other stellar physics are those described in Woosley et al. (2002) and Woosley & Heger (2007). Compositional information on the neutron excess, which can affect the structure during late stages of evolution, was taken at each time step in the calculation from the larger nucleosynthesis co-processing network (§ 2.3). Since this quantity evolves slowly, this procedure proved a stable and cost effective way of implementing some of the results of a large network in a large survey. No rotation was included in the present study and mass loss was taken to be zero. Calculations by Kudritzki (2002); Meynet & Maeder (2002), for example, suggest that the mass loss for non-rotating stars lighter than $100 M_{\odot}$ and metallicity $\lesssim 10^{-5} Z_{\odot}$ can be neglected, though see Meynet et al. (2006).

2.3. Nucleosynthesis Network and Initial Composition

Nucleosynthesis was followed with an adaptive reaction network that included from ~ 250 isotopes on the main sequence to ~ 900 isotopes during the explosion (Rauscher et al. 2002). Isotopes were added and removed as necessary to follow the nuclear reaction flow, with decisions based upon a conservative set of assumptions regarding abundances and flows in the neighborhood.

The initial composition of Pop III stars is, by assumption, pristine Big Bang material. We adopt a Big Bang composition from Cybert et al. (2001, 2002). The assumed initial mass fractions of ^1H , ^2H , ^3He , and ^4He are 0.7513, 4.3×10^{-5} , 2.1×10^{-5} and 0.2487, respectively. A mass fraction of 1.9×10^{-9} was taken for ^7Li .

3. PRESUPERNOVA EVOLUTION

3.1. Ionizing Photon Yield on the Main Sequence

The great majority of the energy released in the evolution of a massive star does not come out as the kinetic energy of stellar winds or of the supernova it produces in the end, but as the light it emits as a stable star. Most of this light is emitted during the long-lived main sequence evolution (central hydrogen burning, about 90% of the star’s lifetime). It is thought that this emission, primarily in the ultraviolet band may have played a key role in ionizing the universe after the recombination epoch (e.g., Loeb & Barkana 2001). At the end of central hydrogen burning the stars expand, making softer radiation, but many stars here remained very blue compared to their more metal-rich counterparts. A few of our more massive stars became red supergiants during their late evolution (Table 3) due to the production of primary nitrogen.

Table 1 gives, for all models, the total energy, E , number of photons, N_{γ} , and the average wavelength, $\bar{\lambda}$, of all photons emitted during the presupernova evolution that are capable of causing hydrogen ionization ($\text{H} + \gamma \mapsto \text{H}^+ + e^-$, marked as “HII”), first helium ionization ($\text{He} + \gamma \mapsto \text{He}^+ + e^-$, marked as “HeII”), second helium ionization ($\text{He}^+ + \gamma \mapsto \text{He}^{2+} + e^-$, marked as “HeIII”), or in the Lyman-Werner (LW) Band ($\text{H}_2 + \gamma \mapsto 2\text{H}$, marked as “LW”). The values given for the LW Band only include photon energies between 11.2 eV and 13.6 eV, i.e., they exclude the hydrogen ionizing photons. The data are obtained by integrating

an time-dependent assumed black body flux and spectrum based on luminosity and effective stellar temperature over the entire stellar evolution. Fig. 1 shows the number of photons for these energies normalized to the stellar mass (photons per baryon).

For convenience, we also give, in Table 2, the photon numbers in bins relevant to primordial radiation chemistry so that they can be added up according to the desired cutoffs. The corresponding energies are given in the Table. We use the following bin boundaries:

H	+ γ	→	H ⁺ + e ⁻	for hν > 13.5984 eV (911.76 Å)
He	+ γ	→	He ⁺ + e ⁻	for hν > 24.5874 eV (504.26 Å)
He ⁺	+ γ	→	He ²⁺ + e ⁻	for hν > 54.4161 eV (227.8 Å)
H ₂	+ γ	→	2 H	for hν > 11.18 eV (1109 Å)
H ₂	+ γ	→	H ₂ ⁺ + e ⁻	for hν > 15.42 eV (804 Å)
H ⁻	+ γ	→	H + e ⁻	for hν > 0.755 eV (16421 Å)
H ₂ ⁺	+ γ	→	H + H ⁺	for hν > 2.65 eV (4678 Å)
H ₂ ⁺	+ γ	→	2 H ⁺ + e ⁻	for hν > 30 eV (413.3 Å)

3.2. Energy Generation and Convective History

The convective and energy generation histories for four representative stars (15 M_⊙, 25 M_⊙, 40 M_⊙, and 80 M_⊙) are given in Figs. 2 and 3.

As has been known for a long time, stars with zero metallicity are different from all other stars (Ezer & Cameron 1971), even those with just a trace of heavy elements. In order to burn hydrogen they must first contract and burn a trace of helium to produce the catalyst for the CNO cycle hydrogen burning (the pp-cycles are never important in such massive stars). This need for high temperature and density to obtain nuclear energy leads to denser, higher entropy cores from the beginning, a characteristic that affects the evolution throughout all subsequent stages. Also, without heavy elements in their outer envelope, these stars are stable against opacity driven pulsations that would tear down their modern counterparts as well as nuclear driven pulsations (Baraffe et al. 2001). They also have weaker hydrogen burning shells and that adds to their tendency to be compact blue stars throughout their entire evolution.

During core hydrogen burning, the central mass fraction of ¹⁴N gradually rises but is typically about 10⁻⁹. Only during the very end of hydrogen burning are much higher values reached, approaching 10⁻⁷. In contrast, during most of hydrogen shell burning, (i.e., during core He burning and thereafter) values of 10⁻⁷ are typical at the base of the shell. In the more massive stars, even those that do not make primary nitrogen (see below), the hydrogen burning shell can nevertheless become very vigorous (e.g., the 40 M_⊙ star shown in Fig. 3) and move outwards in mass at a high rate.

Of the stars whose convective histories are plotted in Figs. 2 and 3, the 15 M_⊙, 25 M_⊙ and 40 M_⊙ stars all die with envelopes that, at least in their outer extremities, are radiative. As Table 3 shows, these three stars are blue supergiants at death. The 15 M_⊙ and 40 M_⊙ stars die without having ever made primary nitrogen in excess of 10⁻⁶ by mass fraction their hydrogen layers. The 25 M_⊙ star did make primary nitrogen of about 10⁻³ in the convective part of its envelope and, given sufficient time, would have expanded to red giant proportions. But it died in transit while still a very blue star (Table 3). This

also happened for the 20.5 M_⊙, 21.5 M_⊙, 27 M_⊙, 28 M_⊙, and 30 M_⊙ models, but above 30 M_⊙, primary nitrogen production always led to a red supergiant progenitor. An example of the latter behavior is the 80 M_⊙ star in Fig. 3.

Carbon burning is convective in the center of the 15 M_⊙ star, but radiative in the heavier ones - consistent with what has been seen in solar metallicity stars and showing that the evolution overall is most sensitive to the helium core mass, not much to the metallicity.

For the 80 M_⊙ star in Fig. 3, a mild nuclear instability is encountered during the ignition of the second oxygen burning shell, notable as a series of growing spikes of energy generation (dark blue) just above a mass coordinate of 7 M_⊙, starting at 10⁻⁴ yr prior to core collapse. These shell flashes reflect the onset of the “pulsational pair instability” (Heger & Woosley 2002). As the mass of the star becomes larger, these flashes become more violent and happen earlier, eventually moving to the center of the star. They can briefly expand the core and reduce the neutrino losses, as seen in the reduction in purple coloration following each flash. During the peak of the last pulse (note logarithmic time scale that make later pulses take more space on the x-axis) burning has proceeded far enough for the stellar core to collapse at this point.

3.3. Primary nitrogen production

As noted in the previous section, some of the models produced primary nitrogen at the base of the hydrogen envelope, a phenomenon that not only affected their nucleosynthesis, but greatly altered their structure.

In the 25 M_⊙ model nitrogen production commenced late in the evolution (Fig. 2), just following central carbon depletion, as the convective helium burning *shell* encroached on the base of the hydrogen envelope. The phenomenon is inhibited in lower mass stars (like the 15 M_⊙ model) presumably because the exoergic nature of carbon burning (including neutrino losses) causes core expansion and a weaker helium shell. Because of the weak hydrogen burning activity, the entropy contrast between the helium convective shell and the base of the hydrogen envelope was not great at the time they touched, $S/N_A k = 12.8$ as compared to 13.4. As the carbon and hydrogen were mixed together as a consequence of convective overshoot mixing, the nitrogen mass fraction at the base of the hydrogen shell rose rapidly. This led to increased energy generation, a rise in entropy, and the onset of hydrogen shell convection. The (“undershoot” and) overshoot mixing of both shells continued to hold them in contact and the nitrogen abundance rose. Carbon was dredged up into the hydrogen shell immediately became nitrogen. This mixing continued until shortly before the star’s death. By that time the entropy at the hydrogen shell had risen to 27.6.

We regard this synthesis of nitrogen as unavoidable, but with an uncertainty in the yield of at least an order of magnitude, especially if the effects of rotation were to be included. We repeated the calculation of the 25 M_⊙ model with convective overshoot turned off, expecting the primary nitrogen to be reduced. Instead a different phenomenon was observed. A trace of hydrogen mixed into the helium shell by the first contact caused a burst of energy generation that raised the entropy. Consequently the outer part of the helium shell, that part into which

hydrogen had been mixed became convective and merged with the hydrogen shell. The substantial amount of carbon in this boundary layer then all became nitrogen in the envelope. Almost the same amount of nitrogen was made as before, but this was a coincidence and the yield was found to depend upon the zoning and time step at the moment the two layers touched.

Even above $25 M_{\odot}$ some stars did *not* make significant primary nitrogen. The $40 M_{\odot}$ model is an example (Fig. 3). The helium shell at the end of carbon burning in this star contained little mass, only $1.3 M_{\odot}$ and burned only a few percent of its helium to carbon before the star died. Consequently, the helium convective burning shell was weak and never made it to the base of the hydrogen shell. The primary nitrogen that was made survived in the hydrogen shell *from hydrogen burning* from its earlier, pre-helium burning evolution. Its mass fraction, between 10^{-7} and 10^{-6} , was adequate to catalyze hydrogen burning and produce a convective region that extended almost to the surface of the star.

In still higher mass stars, of which we may take $80 M_{\odot}$ as representative, copious primary nitrogen production occurred at an earlier stage in the evolution and was more robust. Here the nitrogen was made during helium core burning, again by the encroachment of the helium convective zone on the hydrogen shell. As the hydrogen convective core receded near the end of central hydrogen burning, a gradient of hydrogen concentration was left behind that resulted in several solar masses with hydrogen mass fraction below 10%. The helium convection zone first collided with an appreciable hydrogen abundance when the central helium mass fraction was 0.50. The initial entropy contrast was, as in the case of the $25 M_{\odot}$ star, quite small, and the hydrogen envelope was entirely radiative.

In the collision, a trace of hydrogen was initially convected downwards and combined with carbon to make nitrogen in the outer part of the helium convective core. The energy released raised the entropy and temporarily shut off the convection, truncating nitrogen production after about $10^{-4} M_{\odot}$ had been made. When the helium convective core grew again, most of this nitrogen was convected downwards in the helium core and became ^{22}Ne (with interesting implications for the *s*-process. Later, when the central helium abundance was 0.38, however, the convective core re-expanded into the hydrogen layer again, making more nitrogen, this time about $10^{-3} M_{\odot}$. Enough of this was mixed into the hydrogen envelope to ignite hydrogen burning and produce a convection zone that extended out to a mass coordinate of about $55 M_{\odot}$ (Fig. 3). It also shut off convection in the outer part of the helium convection zone (see the vertical line at $10^{5.35}$ s in Fig. 3). Over time the hydrogen burning replenished a thin shell of helium ash at its base. When helium burning was almost over (central mass fraction 0.02), convective dredge up destroyed this thin buffer shell and carbon began to be dredged up directly into the envelope. The nitrogen abundance rose rapidly at this point ($10^{4.2}$ s in Fig. 3), eventually reaching $0.25 M_{\odot}$, and the star became a fully developed red supergiant.

Rotation, which was neglected here, is likely to have a large effect, on primary nitrogen production, especially on the more massive stars (Hirschi et al. 2008). Shear

mixing between the highly differentially rotating helium core and hydrogen envelope will amplify the effects of convective overshoot that we have included here and lead to greater nitrogen production and more frequent red supergiant progenitors. This could have a dramatic effect on the mixing during the explosion and we intend to include these effects in a subsequent publication.

3.4. Presupernova Models - Structure and Composition

Fig. 4 and Table 3 show the composition and density structure of our presupernova stars. By and large, these structures are the same as seen in solar metallicity stars with the same final helium core mass. Thus whatever central engine blows up solar metallicity stars below $40 M_{\odot}$ should blow up these just as well, though the degree of rotation and the amount of fallback after the initial explosion will differ.

The density of the hydrogen envelope in the $15 M_{\odot}$ stars is much larger and its radius smaller for reasons we have discussed - chiefly the weak hydrogen burning shell in stars with low metallicity. The $25 M_{\odot}$ star, as previously noted, is somewhat anomalous in having produced primary nitrogen shortly before its death, but not yet expanded to red giant proportions. The primary nitrogen and extent of the convection zone are apparent in the bottom frame of Fig. 4. But in general, the helium core structures and especially the iron cores of the zero metallicity stars resemble their solar counterparts. There are greater variations from mass to mass than systematic differences in the two metallicities.

Presupernova properties of the zero metallicity stars are given in Table 3. For comparison, the central density, temperature, entropy, and electron mole number of a $15 M_{\odot}$ solar metallicity star (Woosley & Heger 2007) at the same stage in the collapse would be $7.25 \times 10^9 \text{ g cm}^{-3}$, $7.64 \times 10^9 \text{ K}$, 0.698, and 0.436. For $25 M_{\odot}$ the equivalent numbers would be $3.34 \times 10^9 \text{ g cm}^{-3}$, $7.89 \times 10^9 \text{ K}$, 0.892, and 0.443.

The figures also make clear two possible choices for locating the piston in the explosion - the edge of the iron core, where the electron mole number, Y_e has a sudden decrease, moving inwards, from $Y_e \approx 0.50$ to $Y_e \lesssim 0.48$, and the location of entropy per baryon, $S/N_A k_B = 4.0$. The latter, typically at the base of the oxygen burning shell (Fig. 4), is where the density begins to decline rapidly (moving outwards). The physical motivation for these choices is discussed in the next section.

4. EXPLOSION AND MIXING

Lacking a robust, first principles model for how core-collapse supernovae explode, one must parameterize the explosion. Even if such a fundamental understanding existed, the number of stellar masses to be explored is so large that a parameterized approach would be necessary, but this admittedly adds an element of uncertainty and ambiguity in all studies of nucleosynthesis in supernovae. Assuming that the central engine in these stars initially operates the same as in their modern counterparts (though fallback may differ), then present day constraints on nucleosynthesis, supernova light curves, and remnant masses (Weaver et al. 1978; Woosley & Heger 2007) limit our choices of explosion energy and mass cut. It is possible, however, that early stars of a given mass

differed in ways other than metallicity. More rapid rotation, for example, may have led to a change in the central engine and hence different explosion energies, symmetries, and mixing. Thus we explore here a wide range of explosion energies and make mixing essentially a free parameter.

4.1. *The Piston Model*

One can simulate an explosion either by moving a piston (essentially time-dependent momentum deposition) or depositing energy (usually done instantly, but could, in principle, depend on time and space). We choose the former approach because it is easy to implement in a Lagrangian code and preserves, approximately, the entropy in the material close to the piston. Depositing energy is a reasonable alternative, but brings in additional parameters (e.g., in what mass to deposit the energy) and may artificially increase the entropy of the material in which the energy is deposited.

Besides choosing the location of the piston one must also choose how to move it. A rapid large amplitude motion gives a powerful explosion; a short or slow motion gives a weak one. Here we explore a range of kinetic energies at infinity of 0.3×10^{51} erg to 10^{52} erg with 8 intermediate values. These are named Models “zmX” where “z” stand for the zero metallicity models of this paper, “m” is the mass of the star in solar masses, X is a letter denoting the explosion energy and is one of: A (0.3 Bethe), B (0.6 B), C (0.9 B), D (1.2 B), E (1.5 B), F (1.8 B), G (2.4 B), H, (3.0 B), I (5.0 B), and J(10.0 B) respectively, and the piston mass is situated at $S/N_A k_B = 4.0$. We also followed two additional explosion series with the piston located deeper in the star at the edge of the iron core. These were Models P (explosion energy 1.2 B) and V (explosion energy 10 B)

An important point here is that the energy of the models given is their *kinetic energy at infinity*. This is not the same as the energy often calculated by those who study core collapse, because our energy automatically includes the gravitational binding energy of all the mass that was ejected. That is the energy that must be provided by the central engine is always larger than the energy with which our models are labeled, especially for more massive stars. This difference is also metallicity dependent.

For example, in our Model z25D, the piston is located at $S/N_A k_B = 4.0$ which is at $2.17 M_{\odot}$. In the explosion (plus fallback), all the material external to a final remnant mass of $4.16 M_{\odot}$ is ejected with a kinetic energy of 1.2 B. The binding energy of that ejected material in the presupernova star is 0.775 B, so the central engine, plus any energy generation associated with fallback actually had to provide 1.98 B. For a corresponding solar metallicity star, S25A (Woosley & Heger 2007), the remnant mass was $2.09 M_{\odot}$ and the binding energy in the presupernova star at that point was 0.865 B, so the central engine had to provide 2.07 B. In general, the low metallicity stars are more tightly bound and that makes them harder to explode. But the amount of mass that falls back is also larger and that means less total energy is required to provide the assigned kinetic energy to the material that does escape.

This perhaps cumbersome definition of explosion energy has been used in the nucleosynthesis community for decades and will probably persist until the central engine

responsible for the explosion is better understood.

4.2. *Fallback and Remnant Masses*

The idea of “fallback” in supernovae, the incomplete ejection of matter outside the neutron star, was originally introduced by Colgate & White (1966); Colgate (1971). Chevalier (1989) gave analytic estimates for the time history of fallback and pointed out that fallback would be enhanced in compact stars (e.g., blue supergiants as opposed to red ones). This is because the expanding helium core encounters significant mass at an earlier time in more compact stars, thus decelerating the deep interior at a time when its density is higher. The early arrival of the “reverse shock” at the neutron star thus increases its mass, perhaps turning it into a black hole.

Determining this number accurately poses a computational problem for Lagrangian hydrodynamics codes like KEPLER. If the inner boundary (here “the piston”) is reflecting and is held fixed at a constant radius (here 10^9 cm), then the matter that falls back can pile up on it, ultimately distorting the accretion flow. Later the deposition of energy by radioactive decay can even cause matter that has fallen in to move out again. This problem can be circumvented, in part, by fine zoning near the piston and by moving the piston into a smaller radius, beyond the point where the infall becomes supersonic. In practice, however, attempts to do this resulted in code instability and small steps.

A different approach was therefore adopted. Explosions calculated in KEPLER were linked at 100 s, a time after nucleosynthesis has ceased but fallback has not commenced, to an explicit Eulerian hydrodynamics code. A transmitting inner boundary condition (see also MacFadyen et al. 2001) was assumed and the fallback calculated for the approximately 1200 supernova studied here. The results, for the full range of masses, explosion energies and choices for piston mass, have been determined by Zhang et al. (2007) and were employed for all nucleosynthetic yields reported here. Fig. 6 shows these masses for the explosions of various energies using the $S/N_A k_B = 4$ piston location. As the figure shows, fallback is a very important effect in zero metallicity stars leading, for a standard explosion energy of 1.2 B, to delayed black hole formation in stars over about $25 M_{\odot}$. This can have a dramatic effect on the light curves, nucleosynthesis, and remnant properties of such massive stars.

4.3. *Mixing*

Multi-dimensional effects such as mixing cannot be followed in our one-dimensional code and this adds another source of uncertainty to our calculations. This mixing can be quite important, both for the light curve and the nucleosynthesis. In the more massive stars, nuclei that might not have been ejected without mixing can escape when mixing precedes fallback. Mixing was studied in SN 1987A by many groups and should be similar for the compact stars calculated here (Table 3). For stars with radii $\lesssim 2 \times 10^{12}$ cm, it may be less because the perturbations has less time to grow before freezing out (Herant & Woosley 1994).

Here we adopt a consistent, but artificial prescription for mixing across all masses and explosion energies, the

same essentially as used by Pinto & Woosley (1988) in their study of mixing in SN 1987A. A running boxcar average of width ΔM is moved through the star a total of n times until the desired mixing is obtained. The default values ΔM and n are 10% of the mass of the helium core and 4, respectively. This gives, for example, the mixed composition for a $25 M_{\odot}$ star in Fig. 7. Since this parametric mixing is applied after the explosion is all over, other choices of parameters ranging from no mixing to nearly complete mixing may be explored provided that the distribution of yields with Lagrangian mass in the unmixed model is known (§ 7).

5. LIGHT CURVES

5.1. *UV-Transients from Shock Break Out*

The optical display begins as the supernova shock erupts from the surface giving rise to a brief, hard ultraviolet flash. For the progenitors with radius $R \sim 10^{12}$ cm and explosion energies of 1.2 B, the flash should resemble that estimated for SN 1987A, (e.g., Ensmann & Burrows 1992), i.e., $L \sim 5 \times 10^{44}$ ergs $^{-1}$ for about two minutes with a color temperature, $T_{\text{col}} \sim 10^6$ K. The displays of the more compact stars will be fainter, last a shorter time and have a somewhat harder spectrum. Obviously for supernova that may be happening at high redshift, say $z \sim 5 - 10$, these properties would need to be scaled to the local frame and corrected for ultraviolet absorption between here and the source, which may be significant.

5.2. *Typical Light Curves*

For those compact presupernova with radiative envelopes - essentially those with radii smaller than about $50 R_{\odot}$ in Table 3 - the light curves resemble that of SN 1987A, a brief faint plateau followed by a broad peak powered by radioactive decay (Figs. 9). Depending on details of the mixing, the dip just before the radioactive peak could be greater (less mixing) or absent (with a lot of mixing, as in 87A). For supernovae that experience a lot of fallback, i.e., the lower energy explosions for a given mass, the light curve is much fainter because most of the ^{56}Ni falls into the collapsed remnant.

6. NUCLEOSYNTHESIS

For a given mass star, piston location, mixing prescription, and energy, the nucleosynthesis is completely determined. Mixing is applied across all the nucleosynthesis, including the part that falls back. Otherwise the two operations, mixing and fallback, would not be commutative. Mixing ejecta after some has already been removed from the grid gives a different result than mixing before. Woosley & Weaver (1995) did not include mixing and, as a result, their ejected compositions were more sensitive to fallback.

6.1. *Nucleosynthesis in Representative Models*

Tables 7 through 11 give a subset of the nucleosynthesis determined for the supernovae studied here. They provide the total ejected masses of each stable isotope from hydrogen through germanium for six different mass stars ($12 M_{\odot}$, $15 M_{\odot}$, $20 M_{\odot}$, $25 M_{\odot}$, $35 M_{\odot}$, $50 M_{\odot}$, $75 M_{\odot}$ and $100 M_{\odot}$) and five choices of explosion energy (0.6 B, 1.2 B, 2.4 B, 5 B, and 10 B). Standard piston locations

(the point where $SN\text{Ak}B = 4.0$) and mixing prescriptions (§ 4.3) were employed. It is not necessary to tabulate yields above germanium because they were negligibly small in all cases. We do not include here, however, the nucleosynthesis from the neutrino winds of all those stars that made neutron stars or from any disks in those stars that made black holes. To first order, the r -process and perhaps part of the p -process would be made in the neutrino winds of these first generation stars in the same amounts that they are today. That is, if the solar r -process abundance pattern owes its origin to proto-neutron star winds, it would not be surprising to see the same pattern in second generation stars. More extensive tables, available in the electronic version on the paper, give the ejected masses of each isotope for all 1,440 explosion models with four choices of mixing (120 masses times 10 explosion energies with $SN\text{Ak}B = 4.0$ plus two explosion energies with pistons located at the edge of the iron core). The principal mass fractions in the ejecta of the mixed and unmixed Model z15D are given in Fig. 7 which makes clear the sensitivity of the results to fallback.

6.2. *Lithium and Deuterium Production by the Neutrino Process*

Deuterium, ^3He and ^7Li are known to be important products of Big Bang nucleosynthesis, but interesting quantities can also be made in stars. Fig. 8 shows the distribution of these species and the radioactive progenitor of ^7Li , ^7Be , in the ejecta of the 1.2 B explosion of a $15 M_{\odot}$ star (Model z15D).

These species (as well as ^{11}B and ^{19}F) are made during the explosion by neutrinos interacting with the supernova ejecta (Woosley 1977; Domogatsky et al. 1978; Woosley et al. 1990). The deuterium production occurs in the envelope due to the charged current reaction, $\nu_e(p, e^+)n$, with neutrons immediately reacting with protons to make ^2H . A substantial portion of this ^2H is turned into ^3He , and in any case the abundance is not large enough compared with the Big Bang value, $\sim 4 \times 10^{-5}$, to be interesting. In fact these stars are a net *sinks* for ^2H . The same is true for ^3He .

The most interesting of the three is ^7Li , which is produced in much greater quantities than is destroyed. The reactions of interest are the neutral current process $^4\text{He}(\nu_{\mu, \tau}, n)^3\text{He}(\alpha, \gamma)^7\text{Be}$ in the helium and heavy element core, and the charged current sequence $\bar{\nu}_e(p, e^+)n(p, \gamma)^2\text{H}(p, \gamma)^3\text{He}(\alpha, \gamma)^7\text{Be}$ at the base of the hydrogen envelope (just outside $3.7 M_{\odot}$ in the figure). As we shall see later, the net yield averaged over an initial mass function is an appreciable fraction of solar.

6.3. *Elemental yields as a function of mass*

Figs. 10 show the production factors for all elements as a function of stellar mass and explosion energy. All calculations assumed the standard prescription for mixing. For all but the highest energies, there is significant fallback above $30 M_{\odot}$ that substantially decreases the production of heavy elements.

Taking Case D (1.2 B explosions) as representative case, one sees very limited production of elements above zinc and a strong odd-even effect for elements lighter than silicon. The lighter colored bands for Be and N

are indicative of substantial underproduction. The trend continues to a lesser extent for F, Na, and Al. Beryllium probably does not owe its origin to massive stars and nitrogen may be underproduced because of the neglect of rotation. Fluorine is made in interesting quantities by the neutrino process, but not quite in a solar ratio compared with other major productions. Sodium and aluminum are sensitive to the initial metallicity because the neutron excess in carbon and neon burning is smaller when the metallicity is low.

Some interesting odd Z elements are made though. The reddish band for lithium shows that a lot is being made in stars of many different masses. Boron is also produced in copious quantities by the neutrino process.

Stars lighter than about 12 M_⊙ produce large amounts of silicon through zinc *compared with magnesium*, though the total yield of all heavy elements is low in such light stars. Overall though, one is stuck with the preponderance of blue and black in the figure, i.e., most elements above neon in most stars are made in nearly solar proportions.

6.4. Integrated Elemental Yields

6.4.1. Standard model and variations in IMF and mixing

While the yields of individual stars can vary discontinuously due to the location of various burning shells, the average over large numbers of stars shows less fluctuation. Fig. 11 shows the integrated yields of elements from hydrogen to selenium for various assumptions regarding the initial mass function, explosion energy and mixing.

Panel A of this figure shows what may be regarded as the “standard solution”. All explosion energies are taken to be 1.2B regardless of mass and the standard mixing prescription is employed. The solid line is the result when all masses are included. One sees that the general trends discussed in the previous section are reflected in the integral. Odd-even effects tend to wash out above silicon and nitrogen is underproduced compared with, e.g., oxygen in the sun by almost a factor of 10. For these Population III stars, the initial mass function is particularly uncertain, and might have been “top heavy” compared with modern stars Tan & McKee (2004), so the dashed lines in Panel A explore the consequences of omitting supernovae below a certain mass from the sample. For the standard choices of mixing and explosion energy, deleting stars on the light end of the IMF tends to suppress the production of heavier elements. These heavy elements are made, but a large fraction falls back into the collapsed remnant. Primary nitrogen is augmented by as much as a factor of three because it tends to be made chiefly in the more massive stars and does not fallback.

Panel B shows that the effect of fallback on heavy element production can be even more dramatic if mixing is small or absent and this is certainly one solution to the existence of ultra-iron poor stars (see § 8.2). Mixing is probably suppressed for explosions in presupernova stars that are very compact compared with stars red supergiants derived from the same main sequence mass (Herant & Woosley 1994; Church et al. 2008). Depending on the amount and timing of primary nitrogen production, such compact progenitors may be common in Population III stars (Table 3).

6.4.2. Effect of a mass-dependent explosion energy

While we do not know the details of the explosion mechanism, it is reasonable to expect that it will function differently in stars of varying iron core mass and central density structure. In particular, the density gradients will be shallower in the silicon shells and inner oxygen shells outside the iron cores of higher mass stars. Because of the increased ram pressure from accretion of this material, it will be harder to develop an explosion in stars of higher mass. If no outward shock is generated, the star just becomes a black hole and, in the absence of rotation, simply disappears. This is equivalent to imposing an upper mass limit on the IMF. Such stars would contribute to re ionization, but nothing else. On the other hand, if such stars do explode, one expects their energy to be comparable to their binding energy which increases with mass Woosley et al. (2002). The higher accretion rate may also cause the buildup of a greater overpressure before the shock moves out. These considerations motivate exploring the effect of an explosion energy, E_{kin} , that increases with mass as some power

$$E_{\text{kin}} = F \left(\frac{M}{20 M_{\odot}} \right)^n \quad (1)$$

where F is the kinetic energy at infinity for 20 M_⊙ supernova and n is some positive power. Since we have calculated a large number of stars and explosion energies, interpolation in energy is meaningful and a continuous function can be employed.

Panel C of Fig. 11 explores the consequences of $F = 1.2B$ and $n = 1$ and Panel D shows what happens if F is varied while $n = 0$. In both cases raising the explosion energy for the heavier stars decreases the amount of fallback, increases the iron-group yield, and makes the results overall more robust to variations in the IMF and fallback. The sensitivity of the integrated yields is much more sensitive to mixing, fallback and explosion energy than they are to the placement of the piston (Panels E and F of Fig. 11).

7. AN AUTOMATED FITTING PROCEDURE TO ABUNDANCE PATTERNS

Of course the solar abundance set was not exclusively produced by the first generation of massive stars and it makes more sense to compare the yields with observations of metal-poor stars. Before doing so however, we briefly discuss an algorithm that will facilitate the objective comparison with both average data sets for metal poor stars and individual objects. The parameter space has indeed become rather large - IMF, mixing, fallback, explosion energy, and piston location, so an automated engine to search for the most appropriate models is necessary. The parameters such an algorithm finds as optimal may have interesting implications for the first stars as well as proving that a good fit is in principle possible.

From the complete isotopic yields from our nucleosynthesis calculations we first follow all the decay chains including (ground state) branchings to obtain yields of stable isotopes. To compare with observed abundance patterns we compute elemental yields by adding the number fractions for each isotope.

To find the best fits to observed abundance patterns we compute a data base of ten explosion energies (Ta-

ble 4) and 13 different mixtures (0 and -0.6 , -0.8 , -1.0 [default], ... dex as fraction of the He core size) for each of the 120 stellar models. For the best star fits we search this data base. For the IMF fits we integrate yields for different Salpeter-like power-law IMFs ($\Gamma = -0.65$, 0.35 , 1.35 [standard], 2.35 , 3.35) and for different lower and upper bounds of the IMF. A second set assumes a Gaussian IMF (in $\log M$) centered at different masses and with widths of $(1 \dots 20) \times 0.025$ dex. For both IMFs we assume a mass-dependent explosion energy such that

$$E = E_0 \times \left(\frac{M}{20 M_\odot} \right)^{E^{\text{exp}}} \quad (2)$$

where E_0 can be any of our explosion energies and E^{exp} is one of -1 , -0.5 , 0 [default], 0.5 , 1 .

For the N elements present in each data set (HE0107, HE1327, Cayrel et al. 2004) with $\log \epsilon$ values D_i and uncertainties σ_i we then determine the quality of the fit from the standard formula

$$\chi^2 = \left(\sum_{i=1}^N W_i \right)^{-1} \times \sum_{i=1}^N \frac{(F_i + O - D_i)^2}{\sigma_i^2} W_i. \quad (3)$$

Extra weights W_i can be employed; in this paper we always use $W_i \equiv 1$. The fit value for the elements, F_i , are shifted up or down by a constant offset O . Note that the entire fits is done in logarithmic abundance space. The optimal value for O is found by differentiating Eq. (3) with respect to O and setting it to zero and solving for O to find the minimum (there is no maximum).

Upper limits are only included in the determination of χ when the observational data points lie below the theoretical abundance pattern, otherwise they are ignored. Algorithmically this is implemented by first finding the offset O when all upper limits are ignored. Then we successively add the data points of the lower limits most below the theoretical data (this always will bring the fit down) until only upper limits above the fit remain. For the normalization the upper limits always have to be considered. If there are N normal limits ($i = 1 \dots N$) and U upper limits ($i = N + 1 \dots N + U$) we hence compute χ from

$$\chi^2 = \left(\sum_{i=1}^{N+U} W_i \right)^{-1} \times \left(\sum_{i=1}^N \frac{(F_i + O - D_i)^2}{\sigma_i^2} W_i + \sum_{i=N+1}^{N+U} \frac{(F_i + O - D_i)^2}{\sigma_i^2} W_i \Theta(F_i + O - D_i) \right), \quad (4)$$

where $\Theta(x)$ is the Heaviside function. Lower limits for theoretical data are mathematically equivalent and are treated in an identical way.

For combining elements, e.g., carbon and nitrogen, “C+N”, we add the number fraction of the isotopes. For production factors, we compare the number fraction of isotopes with the total solar number fraction for these elements. The error bars, while given in dex, we combine in linear space by multiplying them by the abundance, i.e., by the product of production factor and solar abundance. For a combined species X which is the combination of N species x_i , $X = x_1 + x_2 + \dots + x_N$ with production factors P_i , solar abundances S_i , and error σ_i in dex we compute

the combined solar number fraction S_X , the combined production factor P_X , and the combined abundance error σ_X (in dex) from

$$S_X = \sum_{i=1}^N S_i, \quad (5)$$

$$P_X = S_X^{-1} \times \sum_{i=1}^N P_i S_i, \quad (6)$$

$$(10^{\sigma_X} - 1)^2 = P_X^{-1} S_X^{-1} \times \sum_{i=1}^N (10^{\sigma_i} - 1)^2 P_i S_i. \quad (7)$$

Hence the absolute error of combination of N species of equal error σ_i is \sqrt{N} times bigger than that of each species, while the relative error becomes smaller by a factor $1/\sqrt{N}$. When combining species for very different number fractions the smaller one does not contribute much to the combined production factor P_X or the combined relative error σ_X (in dex). Note that a species with a high production factor can still have a small number abundance due to a small solar number fraction of this species. For example, when nitrogen has a production factor similar to that of oxygen, nitrogen would contribute little to “N+O” and its error bar since its solar number fraction is about $10 \times$ less than that of oxygen.

8. COMPARISON WITH OBSERVATIONS

8.1. The Cayrel et al. Data Set

Cayrel et al. (2004) have summarized the abundances obtained from observations of 35 giants, 30 of which have $[\text{Fe}/\text{H}]$ in the range -4.1 to -2.7 . In Fig. 12 we show the best matches between our model database and these observations for various choices of physics. Table 17 gives further information on these and other similar fits. Note that we printed in bold font the parameters or limits of each fit that were held fixed. When carrying out these fits, we chose to ignore the element chromium. We simply could not fit the Cayrel et al. Cr abundance using any subset of our models and did not want to contaminate the statistics for the other elements by trying. It seems likely to us that there are greater uncertainties in the Cayrel et al. abundance of Cr than indicated by the published error bar (see also Cayrel et al. 2004; Sobeck et al. 2007; Lai et al. 2008). We also treated our calculated abundances of scandium and copper as lower bounds. The zero metal stars studied here are singular in the absence of any appreciable heavy element production by the s -process. In a separate work in preparation, we have found that this is not the case for stars with even a trace of initial metallicity (e.g., 10^{-4} solar). Since the Cayrel et al. set is for metallicity around 10^{-3} solar, it is reasonable that some contamination by second generation stars may already have occurred. Also, as previously noted, we ignore nucleosynthesis in the neutrino-powered wind (Pruet et al. 2005), GRB accretion disks (Surman et al. 2006) here, and any other r -process site.

Panel E of Fig. 12, by no means the best possible fit, shows the “standard model” - 1.2 B explosions for all masses, standard mixing, and a Salpeter IMF with all stellar masses included. Even this “first guess” gives good overall agreement with the observations. Indeed,

given all the uncertainties in both models and observations, it may be that nothing beyond this set of assumptions is really justified. The elements Cr and Na are greatly overproduced in the model. We have discussed the uncertainty in Cr and Na might have large non-LTE corrections or a contribution from $Z > 0$ stars. Or it may be that the odd-even effect has been underestimated in our models. As we shall see though, it is difficult to simultaneously fit Na, Al, and Mg for any selection of our model space.

Cobalt and zinc on the other hand are underproduced, though not by two sigma. Zinc has an uncertain contribution from the s -process and the neutrino wind (Hoffman et al. 1996). Cobalt is chiefly a product of the alpha-rich freeze out from nuclear statistical equilibrium and its production is therefore particularly sensitive to how the inner zones are treated in the explosion (i.e., using a piston or thermal energy deposition to drive the expansion) and to fallback. Note that simply increasing the explosion energy is not a good solution for the cobalt underproduction (Kobayashi et al. 2006). Panel E shows the results when a higher explosion energy is imposed on a standard IMF, 1.8B at 20 M_⊙ and proportional to M thereafter. The production of Co is not improved and the quality of the overall fit is reduced. Since Ni and Co are both made by the alpha-rich freeze out here, it is hard to raise Co without overproducing Ni.

Other possibilities are explored in Panels A - D. The best overall power law fit, not surprisingly, is achieved in Panel B when the code is allowed to vary simultaneously all degrees of freedom - mixing, explosion energy, slope of the IMF, and upper and lower mass limits. Essentially everything is fit except Na and Cr. The parameters the code finds for this good fit are interesting. It prefers to have stars in the limited mass range 11 M_⊙ to 15 M_⊙, a flatter IMF than Salpeter, very little mixing in the explosion, and a *low* explosion energy that decreases with increasing mass. The low energy and reduced mixing suppress the contribution of the heavier stars because their synthesis mostly falls back into the remnant. Panel A shows again this preference for low mass stars and low explosion energy when the IMF is allowed to be a Gaussian rather than a power law.

It should be noted, however, that the goodness of the fit, both by eye and formally, in the χ , for Panels A - D and even Panel E, does not differ greatly and no particular significance should be attached to any one set of parameters. Panel F on the other hand, where a higher explosion energy is artificially imposed, is a decidedly inferior fit. Overall the Cayrel et al. data set is consistent with a normal IMF and explosion energy, but with a preference for stars lighter than 15 M_⊙ and reduced mixing in the explosion. The reduced mixing may be a natural consequence of the compact nature of the supernova progenitor stars in this mass range.

8.2. Comparison with the Ultra-Iron-Poor Stars

The stars HE0107-5240 (Christlieb et al. 2004; Bessell et al. 2004; Frebel et al. 2005; Collet et al. 2006; Christlieb et al. 2007) and HE1327-2326 (Frebel et al. 2005; Aoki et al. 2006; Frebel et al. 2006; Collet et al. 2006; Frebel et al. 2008) may be representative of a larger class of stars that show both very low iron abundance and extremely high oxygen to iron ratios.

A popular explanation is that such stars represent the ejecta of a primitive stellar population in which mixing was minimal and fallback was large. The small iron abundance thus reflects the fact that, in some supernova or set of supernovae, iron was made, but failed to be mixed sufficiently far out to be ejected (Umeda & Nomoto 2003; Limongi et al. 2003). A very similar scenario was put forward in Depagne et al. (2002) based upon one of our unpublished models for a 35 M_⊙ zero-metallicity supernova, in order to explain another low metal star, CS 22949-037, with a large oxygen to iron ratio. In fact, large oxygen to iron ratios due to fallback in low metallicity supernovae were also published (Models Z35B and Z40B) by Woosley & Weaver (1995).

If the abundances in such stars do reflect the operation of an early generation of supernovae, then the pattern might provide information about those events. Were they high mass stars or low, more energetic or less, mixed or unmixed, and are the results consistent with a range of supernova masses and metallicities or just a single event.

8.3. Comparison with HE0107

Fig. 13 shows several model fits compared with data from Christlieb et al. (2007). The fitting program (§ 7) was again instructed to find the best fit subject to various constraints. As discussed in § 8.1, the element Cr was ignored in the fit, but the observational upper limit and was always above the model value. In general, the best fits were for supernovae in the mass range 12 M_⊙ to 30 M_⊙ with the best single star fit occurring for 20.5 M_⊙ with an explosion energy of 0.6B and very little mixing (Panel A). If the carbon and nitrogen abundances are combined to reflect possible CN processing in the star, the fit is modestly improved (Panel B) and the favored stellar mass shifts to lower values. Gaussian IMFs allow a spread in masses around a preferred value and favor a relatively narrow range of masses around 15 M_⊙, again showing that low explosion energy and less mixing are favored. Panels E and F allow the code to seek a power law fit that is either Salpeter in character (Panel F) or where the exponent is allowed to float (Panel E). In all cases, the best fit is for low explosion energies, small fallback and stars in the 10 M_⊙ to 30 M_⊙ range.

The low energy and preference for lighter supernova progenitors is similar to what was inferred for the Cayrel et al. data set, but more extreme. The Cayrel et al. set definitely required more mixing and was at least consistent with all masses from 10 M_⊙ to 100 M_⊙ participating. The small amount of mixing may relate to the compact nature of the progenitor stars (Church et al. 2008), but could also reflect envelope stripping in a binary system or simply low explosion energy. Unless the central engine produces a grossly asymmetric explosion, one expects the least amount of mixing in Type Ib and Ic supernovae derived from massive stars that have lost their envelopes and this have no reverse shock in the explosion.

8.3.1. Comparison with HE1327-2326

Fits to observations of HE1327-2326 (Fig. 14) select similar models. Here data are taken from Aoki et al. (2006); Frebel et al. (2006) with new upper limits for Cr,

Co, and Ni from Frebel et al. (2008). Again, intermediate masses, low explosion energy, and a very limited amount of fallback are preferred. Markedly inferior fits results for both HE0107 and HE1327 result if one insists on sampling heavier mass stars up to $100 M_{\odot}$ using a Salpeter IMF (Fig. 15). Carbon or carbon plus nitrogen are grossly underproduced. Magnesium is also chronically overproduced. A particularly bad fit ($\chi = 30.3$) is obtained for the “standard model” (Panel F). Clearly these stars have a very different nucleosynthetic history from the Cayrel et al. set. Supernova solutions to the problem are feasible and require low energy, a relatively narrow range of masses, and little mixing. But just why these stars would sample such a limited set possibilities is unclear. Low energy, spherically symmetric explosions in stars that have been stripped of their envelopes in binaries or in compact blue stars like many of the models computed here would be favored. The numbers of such stars in a given generation will be sensitive to the history of primary nitrogen production since this affects whether the star dies as a compact star or a red supergiant. The frequency could thus be a function of both metallicity and rotation rate. It is by no means clear that the ultra-iron poor stars are necessarily more primitive than the stars in the Cayrel et al. set.

9. CONCLUSIONS

We have systematically studied the complete evolution and parameterized explosions of 120 stars of initially zero metallicity. These stars have been exploded with a range of energies - ten choices for kinetic energy at infinity between 0.3 B and 10 B. For two energies, 1.2 B and 10 B, the location of the piston has been varied. Nucleosynthesis has been accurately determined for all isotopes with significant abundance in all these models, as have the remnant masses that result after all fallback is over.

To first order, the nucleosynthesis of major elements has a solar pattern. That is to say, the helium core mass dominates in determining the synthesis of abundant elements with even nuclear charge and the helium core mass is not so different for the lighter, most abundant stars when the metallicity is reduced. There are four important exceptions to this trend though. First, as has long been realized, reducing the metallicity reduces the synthesis of odd- Z elements and neutron-rich isotopes because the neutron excess after helium burning depends on the initial abundance of CNO. This is particularly true for elements lighter than silicon. Second, since the mass loss is less, stars with larger helium cores can survive to the presupernova stage and contribute to the nucleosynthesis (if their explosion energy is large enough to unbind them). Since such large stars have shallow density gradients around their iron cores, explosive nucleosynthesis contributes more to the yield. This can moderately increase the yield of iron group elements and especially the α -rich freeze out. Third, because there is no primordial iron in these stars, there is very little s -process synthesis heavier than germanium. Those few neutrons that are produced during helium burning are absorbed on carbon and oxygen and go to enhancing the production of intermediate mass isotopes. Finally, a significant number of stars, especially those over $40 M_{\odot}$ (and presumably lower with rotation) produce primary nitrogen. This does not happen in non-rotating stars of solar metallicity because

the entropy at the base of the hydrogen shell is much higher and the helium convective core does not extend as far. Even here, in zero metal, non-rotating stars, the interpenetration of shells is sensitive to zoning and an uncertain parameterization of overshoot (and undershoot) mixing.

We do not include here any contribution from the neutrino wind or the “hot convective bubble” in those models that make neutron stars, and most do. Presumably the properties of those neutron stars and their winds would be most sensitive to their mass and not to the star’s initial metallicity. Therefore we expect the same nucleosynthesis in the wind as in modern supernovae. This probably means the production of the r -process (Woosley et al. 1994), some light p -process nuclei by the rp -process (Pruet et al. 2006; Fröhlich et al. 2006), and the production of significant quantities of rare nuclei lighter than molybdenum (Hoffman et al. 1996; Pruet et al. 2005). Most important in the last category may be the elements scandium and zinc. These elements can also be made, to some extent, by the s -process and α -rich freeze out, but one should therefore treat deficient production of these elements in our models with caution.

It should also be noted that *zero* metallicity is a singular condition only realized for the very first generation of stars. Stars of even 10^{-5} solar metallicity will have a different sort of evolution, because they will not have to produce their own catalyst for the CNO cycle and will have *some* iron for the s -process. Our next survey, nearly completed, is for 10^{-4} solar metallicity. Results will be reported elsewhere.

In addition to the above limitations and the omission of rotation, the most fundamental limitations of the models is that they do not incorporate a complete physical model for the explosion - because none is known, and that they are one-dimensional. Consequently, the highly important parameter of “mix”, how much the composition is stirred by the explosion, pulsar remnant, and hydrodynamical instabilities, remains artificial. To compensate for this arbitrariness, we have made a library of all our explosion models and developed an algorithm that allows the user to specify any range of mixing and explosion energy desired, or, conversely, to present a data set and find the best fit. The initial mass function (and whether it is Gaussian, Salpeter, or single star), the power-law dependence of explosion energy on mass, and the mixing can all be varied. Upper and lower mass limits (between $10 M_{\odot}$ and $100 M_{\odot}$) can be specified. This powerful tool is discussed in § 7.

To provide examples, as well as insight, we have applied these models and this “robotic” search for best fits to three sets of data - the “Cayrel” set and two ultra-iron poor stars, HE0107 and HE1327. For the former we find (Fig. 12) several good fits that are not clearly distinguishable within the observational and theoretical error bars. What might be regarded as the “standard model” is not a bad fit. That is a constant kinetic energy at infinity of 1.2 B for all stars, mixing using a moving box car average with width equal to one-tenth the helium core mass, a Salpeter IMF and including all stars from $10 M_{\odot}$ to $100 M_{\odot}$. This model fit, and all others, greatly overproduce chromium which may be more uncertain than reported thus far by the observers. The model also overproduces sodium and underproduces

cobalt and zinc by about two sigma. The fit is significantly improved by reducing the mixing and the explosion energy, especially in the higher mass stars. An explosion energy of around 0.6 B to 0.9 B seems preferred. That the mixing be less than what seems to work well for making solar abundances in higher metallicity stars (Woosley & Heger 2007) may not be surprising. Many of these zero metallicity stars are compact blue stars when they die and mixing by the Rayleigh-Taylor instability is suppressed compared with red supergiants (Herant & Woosley 1994) where the instability has a longer time to develop. The automated fits find no need for a high energy “hypernova” component (Tominaga et al. 2007) despite the presence in our library of stars with up to 10 B of explosion energy.

For the ultra-iron-poor stars we find, as did Umeda & Nomoto (2003), that the low abundance of iron group elements is a consequence of fallback coupled to small mixing. This effect was also seen in the lower energy calculations of metal free stars by Woosley & Weaver (1995) who had *no* mixing at early times, and a deficiency of iron in very low metallicity stars was attributed to fallback in this models by Norris et al. (2001) and Depagne et al. (2002). Here we have considered a much larger sample of models and confirm that low explosion energy (i.e., less than the canonical 1.2 B) for stars above 20 M_⊙ improves the fit and that the mixing should be smaller than for the Cayrel et al. set.

Taken together these calculations suggest several characteristics for the “first supernovae”. First, no nucleosynthetic evidence is found for either pair instability supernovae or hypernovae (contrary to Umeda & Nomoto 2005). The same mass stars that make the solar abundances today could have made the abundances in the most metal stars seen so far quite well. Mixing was less and fallback more important. Both of these effects are consistent with what is expected for more compact supernova progenitors. Fallback would also be greater from the very massive stars that, here at least, had no mass loss and thus died with much greater binding energy. It will be interesting to see if the abundance trends seen in HE0107 and HE1327 are characteristic of all ultra-iron-poor stars when more are discovered.

The compact nature of some of the presupernova stars (Table 3) also affects their light curves (Fig. 9). Supernovae resembling SN 1987A with its initially faint plateau and slow rise to a peak powered by radioactivity might be much more common in the early universe. But this conclusion is sensitive to whether the stars make primary nitrogen or not. Here only the heaviest stars became red supergiants because of nitrogen production, but the inclusion of rotation may extend the critical mass for primary nitrogen production downwards (Heger et al. 2000; Chiappini et al. 2006; Meynet et al. 2006; Hirschi & et al. 2006). If so, the star in many, and perhaps most cases will die as a red supergiant. This would make the light curves more like ordinary Type IIp’s. We caution again, though, that zero metallicity is

a singularity that only characterized the very first stars. We find, in our survey of 10⁻⁴ solar metallicity stars that even a little metallicity can suppress primary nitrogen production and that most of the supernova progenitors are blue stars, though not so compact as for $Z = 0$.

For the upper end of the mass range studied, above about 90 M_⊙, the pulsational pair instability is encountered. This leads to the ejection of the envelope and part of the helium core in a series of violent nuclear powered flashes (Woosley, Blinnikov, & Heger 2007). Collisions between the shells ejected in pairs of flashes can produce extraordinarily bright supernovae.

Finally, the compact remnants of massive stellar evolution, especially black holes, will be more massive for zero (and low) metallicity. There are two reasons. First, because the mass loss rate is low, larger helium cores are possible at the time the star dies. This both increases the potential mass reservoir for making a black hole by fallback (the hydrogen envelope is almost always ejected) and makes it harder to explode the star. Indeed, unless the explosion mechanism can somehow provide a much greater energy than 1 B, black holes will be the typical result of stellar evolution for main sequence masses above about 30 M_⊙ (Zhang et al. 2007). Black hole formation is also favored in compact presupernova stars because the reverse shock develops earlier and reaches the center when the density is still high (Chevalier 1989; Zhang et al. 2007). The maximum black hole mass, though, will be about 40 M_⊙, even for very low explosion energies. This is the largest helium core that avoids the pulsational pair instability.

We are grateful to Thomas Janka for his physically motivated suggestion to use the density jump at the base of the O shell as most likely location for the initial piston that explodes the star. We thank Rob Hoffman, Tommy Rauscher, Frank Timmes, Jason Pruet, Karlheinz Langanke, and Gabriel Martinez-Pinedo for their contributions to the reaction rate library, weak interaction rates, and neutrino cross sections. We are also grateful to Tim Beers, Mike Bolte, and David Lai for discussions about the interpretation of UMP star abundance and enrichment observation and theory. We particularly thank Anna Frebel and Norbert Christlieb for providing us their most recent abundance data for HE0107 and HE1327. We thank Dan Whalen for helpful discussions about primordial gas chemistry and relevant radiation bands, and we thank Candace Church for providing us results from her work in preparation on multi-dimensional simulations of mixing in Pop III supernovae.

This work was supported by the NSF (AST 02-06111), and the DOE Program for Scientific Discovery through Advanced Computing (SciDAC; grants DOE-FC02-01ER41176 and DOE-FC02-06ER41438). At LANL, Heger performed this work under the auspices of the National Nuclear Security Administration of the U.S. Department of Energy at Los Alamos National Laboratory under Contract No. DE-AC52-06NA25396.

REFERENCES

- Aoki, W. et al. 2006, ApJ, 639, 897
 Baraffe, I., Heger, A., & Woosley, S. E. 2001, ApJ, 550, 890
 Barkat, Z., & Marom, A. 1990, Supernovae, Jerusalem Winter School for Theoretical Physics, 95

- Bessell, M. S., Christlieb, N., & Gustafsson, B. 2004, *ApJ*, 612, L61
- Cayrel, R., et al. 2004, *A&A*, 416, 1117.
- Chevalier, R. A. 1989, *ApJ*, 346, 847
- Chiappini, C., Hirschi, R., Meynet, G., Ekström, S., Maeder, A., & Matteucci, F. 2006, *A&A*, 449, L27
- Chieffi, A., & Limongi, M. 2004, *ApJ*, 608, 405
- Christlieb, N., et al. 2002, *Nature*, 419, 904
- Christlieb, N., Gustafsson, B., Korn, A. J., Barklem, P. S., Beers, T. C., Bessell, M. S., Karlsson, T., & Mizuno-Wiedner, M. 2004, *ApJ*, 603, 708
- Christlieb, N., Bessell, M.S., & Eriksson, K. 2007, *ApJ*, submitted
- Church, C., Woosley, S. E., & Heger, A. 2008, in preparation
- Colgate, S. A., & White, R. H. 1966, *ApJ*, 143, 626
- Colgate, S. A. 1971, *ApJ*, 163, 221
- Collet, R., Asplund, M., & Trampedach, R. 2006, *ApJ*, 644, L121
- Cybert, R. H., Fields, B. D., & Olive, K. A. 2001, *New Astronomy*, 6, 215
- Cybert, R. H., Fields, B. D., & Olive, K. A. 2002, *Astroparticle Physics*, 17, 87
- Depagne, E., et al. 2002, *A&A*, 390, 187
- G. V. Domogatsky, G. V., Eramzhyan, R. A., & Nadyozhin, D. K. 1978, *Ap. Sp. Sci.*, 58, 273
- Ensmann, L., & Burrows, A. 1992, *ApJ*, 393, 742
- Ezer, D., & Cameron, A. G. W. 1971, *Ap&SS*, 14, 399
- Fröhlich, C., Martínez-Pinedo, G., Liebendörfer, M., Thielemann, F.-K., Bravo, E., Hix, W. R., Langanke, K., & Zinner, N. T. 2006, *Physical Review Letters*, 96, 142502
- Frebel, A., et al. 2005, *Nature*, 434, 871
- Frebel, A., Christlieb, N., Norris, J. E., Aoki, W., & Asplund, M. 2006, *ApJ*, 638, L17
- Frebel, A., Collet, R., Eriksson, K., Christlieb, N. & Aoki, W. 2008, *ApJ*, submitted
- Heger, A., Woosley, S. E., & Waters, R. 2000, in *The First Stars: Proceedings of the MPA/ESO Workshop, ESO ASTROPHYSICS SYMPOSIA*. ISBN 3-540-67222-2. Edited by A. Weiss, T.G. Abel, and V. Hill. Springer-Verlag, p. 121
- Heger, A., & Woosley, S. E. 2002, *ApJ*, 567, 532
- Herant, M., & Woosley, S. E. 1994, *ApJ*, 425, 814
- Hirschi, R., & et al. 2006, *Reviews in Modern Astronomy*, 19, 101
- Hirschi, R., Chiappini, C., Meynet, G., Maeder, A., & Ekstrom, S. 2008, in *Massive Stars as Cosmic Engines* (IAU Symp 250), eds. F. Bresolin, P.A. Crowther, J. Puls, p. 101 - 111, *astroph-0802.1675*
- Hoffman, R. D., Woosley, S. E., Fuller, G. M., & Meyer, B. S. 1996, *ApJ*, 460, 478
- Kobayashi, C., Umeda, H., Nomoto, K., Tominaga, N., & Ohkubo, T. 2006, *ApJ*, 653, 1145
- Kogut, A., et al. 2003, *ApJS*, 148, 161
- Kudritzki, R. P. 2002, *ApJ*, 577, 389
- Lai, D. K., Bolte, M., Johnson, J. A., Lucatello, S., Heger, A., & Woosley, S. E. 2008, *ApJ*, submitted
- Limongi, M., Chieffi, A., & Bonifacio, P. 2003, *ApJ*, 594, L123
- Loeb, A., & Barkana, R. 2001, *ARA&A*, 39, 19
- MacFadyen, A. I., Woosley, S. E., & Heger, A. 2001, *ApJ*, 550, 410
- Marigo, P., Girardi, L., Chiosi, C., & Wood, P. R. 2001, *A&A*, 371, 152
- Meynet, G., & Maeder, A. 2002, *A&A*, 390, 561
- Meynet, G., Ekström, S., & Maeder, A. 2006, *A&A*, 447, 623
- Norris, J. E., Ryan, S. G., & Beers, T. C. 2001, *ApJ*, 561, 1034
- O'Shea, B. W., McKee, C. F., Heger, A., and Abel, T. 2008, in *First Stars III Conference Proceedings*, eds. B. W. O'Shea, A. Heger, and T. Abel, in press; arXiv0801.2124
- Pinto, P. A., & Woosley, S. E. 1988, *Nature*, 333, 534
- Pruet, J., Woosley, S. E., Buras, R., Janka, H.-T., & Hoffman, R. D. 2005, *ApJ*, 623, 325
- Pruet, J., Hoffman, R. D., Woosley, S. E., Janka, H.-T., & Buras, R. 2006, *ApJ*, 644, 1028
- Rauscher, T., Heger, A., Hoffman, R. D., & Woosley, S. E. 2002, *ApJ*, 576, 323
- Sobeck, J. S., Lawler, J. E., & Sneden, C. 2007, *ApJ*, 667, 1267
- Tan, J. C., & McKee, C. F. 2004, *ApJ*, 603, 383
- Tominaga, N., Umeda, H., & Nomoto, K. 2007, *ApJ*, 660, 516
- Umeda, H., & Nomoto, K. 2003, *Nature*, 422, 871
- Umeda, H., & Nomoto, K. 2005, *ApJ*, 619, 427
- Spergel, D. N., et al. 2003, *ApJS*, 148, 175
- Surman, R., McLaughlin, G. C., & Hix, W. R. 2006, *ApJ*, 643, 1057
- Woosley, S. E. 1977, *Nature*, 269, 42
- Weaver, T. A., Zimmerman, G. B., & Woosley, S. E. 1978, *ApJ*, 225, 1021
- Woosley, S. E., & Weaver, T. A. 1988, *Phys. Rep.*, 163, 79
- Woosley, S. E., Hartmann, D. H., Hoffman, R. D., & Haxton, W. C. 1990, *ApJ*, 356, 272
- Woosley, S. E., Wilson, J. R., Mathews, G. J., Hoffman, R. D., & Meyer, B. S. 1994, *ApJ*, 433, 229
- Woosley, S. E., & Weaver, T. A. 1995, *ApJS*, 101, 181 (WW95)
- Woosley, S. E., Heger, A., & Weaver, T. A. 2002, *RMP*, 74, 1015
- Woosley, S. E., & Heger, A. 2007, *Phys. Rep.*, 442, 269
- Woosley, S. E., Blinnikov, S. A., & Heger, A. 2007, *Nature*, submitted
- Zhang, W., Woosley, S. E., & Heger, A. 2007, *ApJ*, in press

TABLE 2
 BINNED PHOTON NUMBERS (CONTINUED)

mass M_{\odot}	0.755eV2.650 eV	2.650eV11.18 eV	11.18eV13.60 eV	13.60eV15.42 eV	15.42eV24.59 eV	24.59eV30.00 eV	30.00eV54.42 eV	>54.42 eV
19.2	1.57×10^{62}	1.39×10^{63}	3.49×10^{62}	2.23×10^{62}	6.64×10^{62}	1.56×10^{62}	1.30×10^{62}	2.92×10^{60}
19.4	1.56×10^{62}	1.40×10^{63}	3.51×10^{62}	2.25×10^{62}	6.73×10^{62}	1.59×10^{62}	1.34×10^{62}	3.07×10^{60}
19.6	1.57×10^{62}	1.41×10^{63}	3.55×10^{62}	2.28×10^{62}	6.83×10^{62}	1.62×10^{62}	1.37×10^{62}	3.19×10^{60}
19.8	1.63×10^{62}	1.46×10^{63}	3.67×10^{62}	2.35×10^{62}	7.04×10^{62}	1.67×10^{62}	1.41×10^{62}	3.30×10^{60}
20.0	1.81×10^{62}	1.59×10^{63}	3.92×10^{62}	2.50×10^{62}	7.38×10^{62}	1.72×10^{62}	1.44×10^{62}	3.41×10^{60}
20.5	1.80×10^{62}	1.60×10^{63}	3.99×10^{62}	2.55×10^{62}	7.62×10^{62}	1.81×10^{62}	1.53×10^{62}	3.75×10^{60}
21.0	1.69×10^{62}	1.54×10^{63}	3.93×10^{62}	2.54×10^{62}	7.73×10^{62}	1.89×10^{62}	1.64×10^{62}	4.19×10^{60}
21.5	1.89×10^{62}	1.69×10^{63}	4.25×10^{62}	2.73×10^{62}	8.23×10^{62}	1.99×10^{62}	1.73×10^{62}	4.51×10^{60}
22.0	1.82×10^{62}	1.65×10^{63}	4.24×10^{62}	2.74×10^{62}	8.38×10^{62}	2.06×10^{62}	1.83×10^{62}	4.93×10^{60}
22.5	1.83×10^{62}	1.67×10^{63}	4.33×10^{62}	2.81×10^{62}	8.66×10^{62}	2.16×10^{62}	1.94×10^{62}	5.39×10^{60}
23.0	1.88×10^{62}	1.72×10^{63}	4.46×10^{62}	2.90×10^{62}	8.97×10^{62}	2.25×10^{62}	2.04×10^{62}	5.81×10^{60}
23.5	1.96×10^{62}	1.79×10^{63}	4.64×10^{62}	3.02×10^{62}	9.34×10^{62}	2.35×10^{62}	2.14×10^{62}	6.27×10^{60}
24.0	1.94×10^{62}	1.79×10^{63}	4.68×10^{62}	3.05×10^{62}	9.53×10^{62}	2.43×10^{62}	2.25×10^{62}	6.79×10^{60}
24.5	2.09×10^{62}	1.92×10^{63}	4.97×10^{62}	3.23×10^{62}	1.00×10^{63}	2.55×10^{62}	2.36×10^{62}	7.25×10^{60}
25.0	2.14×10^{62}	1.96×10^{63}	5.11×10^{62}	3.32×10^{62}	1.04×10^{63}	2.66×10^{62}	2.49×10^{62}	7.86×10^{60}
25.5	2.16×10^{62}	2.00×10^{63}	5.23×10^{62}	3.41×10^{62}	1.07×10^{63}	2.76×10^{62}	2.61×10^{62}	8.43×10^{60}
26.0	2.20×10^{62}	2.03×10^{63}	5.34×10^{62}	3.49×10^{62}	1.10×10^{63}	2.85×10^{62}	2.71×10^{62}	8.94×10^{60}
26.5	2.28×10^{62}	2.10×10^{63}	5.50×10^{62}	3.59×10^{62}	1.13×10^{63}	2.94×10^{62}	2.81×10^{62}	9.49×10^{60}
27.0	2.37×10^{62}	2.18×10^{63}	5.69×10^{62}	3.72×10^{62}	1.17×10^{63}	3.05×10^{62}	2.94×10^{62}	1.01×10^{61}
27.5	2.34×10^{62}	2.17×10^{63}	5.74×10^{62}	3.76×10^{62}	1.20×10^{63}	3.16×10^{62}	3.08×10^{62}	1.08×10^{61}
28.0	2.46×10^{62}	2.27×10^{63}	5.96×10^{62}	3.90×10^{62}	1.24×10^{63}	3.26×10^{62}	3.18×10^{62}	1.14×10^{61}
28.5	2.38×10^{62}	2.23×10^{63}	5.94×10^{62}	3.91×10^{62}	1.25×10^{63}	3.35×10^{62}	3.31×10^{62}	1.21×10^{61}
29.0	2.50×10^{62}	2.33×10^{63}	6.18×10^{62}	4.06×10^{62}	1.30×10^{63}	3.47×10^{62}	3.44×10^{62}	1.28×10^{61}
29.5	2.42×10^{62}	2.29×10^{63}	6.14×10^{62}	4.06×10^{62}	1.31×10^{63}	3.55×10^{62}	3.57×10^{62}	1.36×10^{61}
30.0	2.63×10^{62}	2.44×10^{63}	6.47×10^{62}	4.25×10^{62}	1.36×10^{63}	3.66×10^{62}	3.68×10^{62}	1.43×10^{61}
30.5	2.50×10^{62}	2.37×10^{63}	6.39×10^{62}	4.23×10^{62}	1.37×10^{63}	3.75×10^{62}	3.82×10^{62}	1.50×10^{61}
31.0	2.53×10^{62}	2.40×10^{63}	6.49×10^{62}	4.30×10^{62}	1.40×10^{63}	3.85×10^{62}	3.95×10^{62}	1.59×10^{61}
31.5	2.81×10^{62}	2.61×10^{63}	6.94×10^{62}	4.57×10^{62}	1.47×10^{63}	4.00×10^{62}	4.10×10^{62}	1.67×10^{61}
32.0	2.69×10^{62}	2.54×10^{63}	6.85×10^{62}	4.53×10^{62}	1.48×10^{63}	4.07×10^{62}	4.21×10^{62}	1.75×10^{61}
32.5	2.89×10^{62}	2.69×10^{63}	7.18×10^{62}	4.74×10^{62}	1.53×10^{63}	4.20×10^{62}	4.35×10^{62}	1.83×10^{61}
33.0	2.88×10^{62}	2.71×10^{63}	7.25×10^{62}	4.79×10^{62}	1.56×10^{63}	4.30×10^{62}	4.49×10^{62}	1.91×10^{61}
33.5	3.20×10^{62}	2.93×10^{63}	7.68×10^{62}	5.04×10^{62}	1.62×10^{63}	4.42×10^{62}	4.61×10^{62}	1.99×10^{61}
34.0	2.83×10^{62}	2.69×10^{63}	7.33×10^{62}	4.87×10^{62}	1.60×10^{63}	4.50×10^{62}	4.76×10^{62}	2.10×10^{61}
34.5	3.03×10^{62}	2.84×10^{63}	7.65×10^{62}	5.06×10^{62}	1.65×10^{63}	4.61×10^{62}	4.88×10^{62}	2.17×10^{61}
35.0	3.06×10^{62}	2.88×10^{63}	7.76×10^{62}	5.14×10^{62}	1.69×10^{63}	4.72×10^{62}	5.04×10^{62}	2.28×10^{61}
36.0	2.99×10^{62}	2.86×10^{63}	7.83×10^{62}	5.22×10^{62}	1.73×10^{63}	4.91×10^{62}	5.30×10^{62}	2.46×10^{61}
37.0	3.10×10^{62}	2.96×10^{63}	8.11×10^{62}	5.41×10^{62}	1.80×10^{63}	5.13×10^{62}	5.58×10^{62}	2.65×10^{61}
38.0	3.95×10^{62}	3.38×10^{63}	8.59×10^{62}	5.65×10^{62}	1.85×10^{63}	5.29×10^{62}	5.83×10^{62}	2.85×10^{61}
39.0	6.87×10^{62}	3.80×10^{63}	8.58×10^{62}	5.66×10^{62}	1.89×10^{63}	5.49×10^{62}	6.12×10^{62}	3.06×10^{61}
40.0	3.45×10^{62}	3.29×10^{63}	8.99×10^{62}	6.00×10^{62}	2.00×10^{63}	5.79×10^{62}	6.45×10^{62}	3.28×10^{61}
41.0	4.24×10^{62}	3.71×10^{63}	9.53×10^{62}	6.28×10^{62}	2.07×10^{63}	5.95×10^{62}	6.70×10^{62}	3.49×10^{61}
42.0	4.02×10^{62}	3.69×10^{63}	9.79×10^{62}	6.49×10^{62}	2.15×10^{63}	6.20×10^{62}	7.00×10^{62}	3.71×10^{61}
43.0	4.11×10^{62}	3.79×10^{63}	1.01×10^{63}	6.69×10^{62}	2.22×10^{63}	6.42×10^{62}	7.29×10^{62}	3.94×10^{61}
44.0	4.11×10^{62}	3.83×10^{63}	1.03×10^{63}	6.84×10^{62}	2.28×10^{63}	6.65×10^{62}	7.59×10^{62}	4.16×10^{61}
45.0	4.92×10^{62}	4.04×10^{63}	1.03×10^{63}	6.82×10^{62}	2.28×10^{63}	6.74×10^{62}	7.84×10^{62}	4.41×10^{61}
50.0	8.42×10^{62}	5.00×10^{63}	1.18×10^{63}	7.74×10^{62}	2.59×10^{63}	7.79×10^{62}	9.31×10^{62}	5.65×10^{61}
55.0	1.88×10^{63}	6.60×10^{63}	1.21×10^{63}	8.05×10^{62}	2.79×10^{63}	8.69×10^{62}	1.07×10^{63}	6.99×10^{61}
60.0	7.09×10^{62}	5.75×10^{63}	1.43×10^{63}	9.48×10^{62}	3.22×10^{63}	9.89×10^{62}	1.23×10^{63}	8.42×10^{61}
65.0	1.30×10^{63}	7.14×10^{63}	1.52×10^{63}	9.96×10^{62}	3.41×10^{63}	1.07×10^{63}	1.38×10^{63}	9.88×10^{61}
70.0	9.24×10^{62}	7.10×10^{63}	1.71×10^{63}	1.12×10^{63}	3.81×10^{63}	1.19×10^{63}	1.53×10^{63}	1.14×10^{62}
75.0	6.40×10^{63}	8.55×10^{63}	1.60×10^{63}	1.10×10^{63}	3.95×10^{63}	1.29×10^{63}	1.69×10^{63}	1.30×10^{62}
80.0	3.21×10^{63}	9.45×10^{63}	1.80×10^{63}	1.20×10^{63}	4.24×10^{63}	1.38×10^{63}	1.84×10^{63}	1.46×10^{62}
85.0	2.54×10^{63}	1.02×10^{64}	1.95×10^{63}	1.29×10^{63}	4.54×10^{63}	1.49×10^{63}	1.99×10^{63}	1.62×10^{62}
90.0	6.32×10^{63}	9.85×10^{63}	2.05×10^{63}	1.37×10^{63}	4.84×10^{63}	1.59×10^{63}	2.15×10^{63}	1.78×10^{62}
95.0	2.89×10^{63}	1.24×10^{64}	2.41×10^{63}	1.55×10^{63}	5.14×10^{63}	1.59×10^{63}	2.11×10^{63}	1.83×10^{62}
100.0	1.59×10^{63}	1.06×10^{64}	2.50×10^{63}	1.65×10^{63}	5.68×10^{63}	1.83×10^{63}	2.48×10^{63}	2.12×10^{62}

TABLE 3
SUMMARY OF PRESUPERNOVA MODEL DATA

mass (M _⊙)	T _c (GK)	ρ _c (kt/cm ³)	S _c (k _B /u)	Y _{e,c}	He core (M _⊙)	C/O core (M _⊙)	O shell (M _⊙)	Y _e core (M _⊙)	BE _{Y_ecore} (B)	M _{S=4} (M _⊙)	BE _{S=4} (B)	R _{eff} (R _⊙)	T _{eff} (kK)	L _{eff} (kL _⊙)
10.0	6.023	16.52	0.493	0.426	1.90	1.43	1.27	1.27	0.09	1.28	0.09	62	8.02	14
10.2	6.642	18.43	0.515	0.424	1.97	1.45	1.29	1.18	0.27	1.38	0.04	38	10.51	15
10.4	6.731	17.01	0.531	0.422	2.29	1.59	1.32	1.18	0.34	1.32	0.11	34	11.58	18
10.5	6.488	14.79	0.528	0.424	2.15	1.54	1.33	1.20	0.34	1.41	0.07	27	12.77	17
10.6	6.468	18.41	0.505	0.425	2.09	1.52	1.31	1.20	0.30	1.40	0.06	21	14.86	18
10.7	6.499	14.85	0.528	0.425	2.17	1.54	1.32	1.19	0.35	1.41	0.08	20	15.12	18
10.8	6.537	14.74	0.533	0.424	2.20	1.56	1.34	1.17	0.39	1.34	0.13	19	15.96	20
10.9	6.395	14.97	0.524	0.423	2.22	1.57	1.33	1.25	0.27	1.43	0.08	17	16.87	20
11.0	6.072	11.79	0.531	0.429	2.19	1.59	1.33	1.33	0.23	1.42	0.12	15	17.89	21
11.1	6.521	14.65	0.530	0.427	2.42	1.77	1.31	1.27	0.22	1.31	0.14	18	16.71	22
11.2	6.421	14.35	0.532	0.423	2.29	1.62	1.35	1.19	0.37	1.35	0.14	14	18.81	22
11.3	6.509	12.21	0.549	0.425	2.37	1.68	1.34	1.18	0.43	1.47	0.11	14	18.85	23
11.4	6.783	11.83	0.568	0.427	2.58	1.77	1.40	1.22	0.43	1.48	0.16	18	16.95	25
11.5	6.338	14.51	0.525	0.423	2.40	1.68	1.35	1.35	0.15	1.35	0.15	13	20.30	24
11.6	6.303	14.71	0.521	0.423	2.40	1.71	1.34	1.34	0.16	1.34	0.16	12	20.89	25
11.7	7.163	14.11	0.570	0.426	2.53	1.73	1.38	1.23	0.41	1.38	0.17	13	20.62	26
11.8	6.901	13.51	0.560	0.428	2.47	1.76	1.39	1.24	0.40	1.49	0.16	12	21.72	26
11.9	6.870	15.08	0.545	0.428	2.52	1.77	1.36	1.26	0.34	1.54	0.13	11	22.17	27
12.0	6.475	15.19	0.524	0.427	2.48	1.79	1.30	1.26	0.23	1.30	0.15	12	21.86	29
12.2	7.056	11.78	0.585	0.429	2.82	1.92	1.42	1.26	0.44	1.51	0.19	14	20.39	32
12.4	7.245	10.37	0.614	0.432	2.61	1.88	1.46	1.31	0.44	1.46	0.24	10	24.51	32
12.6	7.140	11.86	0.589	0.426	2.65	1.92	1.37	1.23	0.49	1.50	0.20	10	24.98	33
12.8	6.984	10.39	0.597	0.431	2.77	1.97	1.41	1.31	0.38	1.41	0.21	10	25.55	35
13.0	6.543	10.46	0.574	0.433	2.81	2.01	1.40	1.37	0.25	1.40	0.21	19	18.42	37
13.2	7.055	11.40	0.592	0.433	2.91	2.04	1.42	1.31	0.43	1.54	0.23	10	25.30	38
13.4	7.009	9.04	0.620	0.435	2.97	2.10	1.45	1.35	0.43	1.57	0.21	9.1	27.00	39
13.6	6.720	9.67	0.594	0.434	3.02	2.17	1.42	1.41	0.27	1.42	0.27	10	26.12	42
13.8	7.100	8.51	0.633	0.434	3.08	2.22	1.45	1.37	0.44	1.45	0.32	9.0	27.95	44
14.0	7.186	7.63	0.657	0.438	3.19	2.29	1.47	1.37	0.52	1.57	0.29	9.0	28.17	46
14.2	7.331	7.37	0.672	0.437	3.24	2.32	1.50	1.38	0.53	1.58	0.30	9.0	28.42	48
14.4	7.276	6.63	0.685	0.438	3.39	2.44	1.50	1.39	0.56	1.62	0.31	9.2	28.32	49
14.6	7.312	6.65	0.686	0.437	3.46	2.46	1.56	1.40	0.55	1.56	0.36	9.0	29.00	52
14.8	7.341	6.51	0.692	0.438	3.50	2.48	1.57	1.41	0.55	1.56	0.37	9.0	29.29	54
15.0	7.373	10.99	0.614	0.430	3.70	2.65	1.43	1.28	0.53	1.43	0.30	10	28.23	55
15.2	7.075	9.88	0.611	0.433	3.85	2.75	1.45	1.33	0.49	1.45	0.32	10	28.47	56
15.4	7.134	10.72	0.603	0.432	3.71	2.65	1.43	1.31	0.50	1.43	0.31	10	28.37	56
15.6	7.122	8.19	0.640	0.434	3.87	2.81	1.46	1.36	0.52	1.46	0.38	8.9	30.21	60
15.8	7.372	7.27	0.678	0.438	3.90	2.76	1.55	1.36	0.62	1.55	0.40	8.7	30.66	60
16.0	7.390	6.43	0.698	0.438	3.98	2.86	1.58	1.41	0.62	1.58	0.42	8.9	30.92	65
16.2	7.487	6.00	0.718	0.438	4.01	2.85	1.61	1.42	0.66	1.61	0.44	8.9	31.09	66
16.4	7.495	5.70	0.728	0.439	4.14	2.97	1.64	1.45	0.67	1.63	0.46	8.8	31.16	66
16.6	7.508	5.84	0.725	0.439	4.31	3.16	1.63	1.44	0.68	1.63	0.47	9.1	31.05	69
16.8	7.417	5.75	0.718	0.437	4.23	2.99	1.67	1.32	0.84	1.74	0.48	10	31.05	78
17.0	7.564	5.62	0.735	0.437	4.37	3.16	1.76	1.35	0.87	1.76	0.52	9.0	31.98	76
17.1	7.651	5.54	0.747	0.438	4.39	3.19	1.77	1.37	0.86	1.77	0.53	8.9	32.32	78
17.2	7.480	5.59	0.728	0.437	4.41	3.18	1.74	1.34	0.87	1.74	0.52	9.1	32.14	80
17.3	7.775	6.16	0.740	0.439	4.46	3.22	1.67	1.39	0.84	1.82	0.53	9.0	32.85	84
17.4	7.292	8.11	0.654	0.436	4.50	3.24	1.49	1.37	0.63	1.50	0.45	10	31.84	84
17.5	7.734	5.87	0.745	0.439	4.54	3.29	1.59	1.40	0.85	1.82	0.54	9.1	33.28	90
17.6	7.777	5.49	0.763	0.440	4.75	3.57	1.69	1.46	0.85	1.87	0.59	10	31.63	89
17.7	7.279	5.65	0.709	0.437	4.66	3.41	1.73	1.58	0.64	1.73	0.52	9.1	32.43	82
17.8	7.786	5.47	0.763	0.439	4.70	3.47	1.65	1.40	0.91	1.83	0.59	9.1	33.10	89
17.9	7.762	5.51	0.760	0.439	4.67	3.41	1.61	1.41	0.87	1.84	0.58	9.3	32.99	93
18.0	7.007	7.84	0.640	0.436	4.71	3.45	1.49	1.38	0.55	1.49	0.40	26	19.48	87
18.1	7.355	7.32	0.674	0.436	4.74	3.44	1.47	1.39	0.65	1.53	0.46	11	30.15	96
18.2	7.756	6.52	0.728	0.439	4.80	3.53	1.65	1.41	0.84	1.54	0.70	9.4	32.58	89
18.3	7.868	6.02	0.754	0.440	4.87	3.61	1.68	1.43	0.88	1.70	0.69	9.5	33.65	103
18.4	6.790	7.46	0.634	0.437	4.90	3.61	1.42	1.40	0.48	1.51	0.33	51	14.33	99
18.5	7.397	6.76	0.690	0.437	4.92	3.62	1.55	1.41	0.68	1.55	0.50	11	30.89	101

(continued on next page)

TABLE 3
SUMMARY OF PRESUPERNOVA MODEL DATA (CONTINUED)

mass (M_{\odot})	T_c (GK)	ρ_c (kt/cm^3)	S_c (k_B/u)	$Y_{e,c}$	He core (M_{\odot})	C/O core (M_{\odot})	O shell (M_{\odot})	Y_e core (M_{\odot})	$BE_{Y_{e,\text{core}}}$ (B)	$M_{S=4}$ (M_{\odot})	$BE_{S=4}$ (B)	R_{eff} (R_{\odot})	T_{eff} (kK)	L_{eff} (kL_{\odot})
18.6	7.099	7.32	0.657	0.437	4.92	3.63	1.51	1.41	0.57	1.51	0.42	22	21.56	95
18.7	7.316	6.86	0.681	0.436	4.99	3.69	1.55	1.41	0.66	1.55	0.48	10	32.31	98
18.8	7.400	6.42	0.699	0.438	5.00	3.68	1.57	1.42	0.69	1.57	0.50	11	31.38	105
18.9	7.498	5.33	0.740	0.439	5.26	4.02	1.63	1.47	0.76	1.63	0.56	11	31.76	101
19.0	7.575	5.68	0.736	0.439	5.30	4.05	1.63	1.44	0.80	1.63	0.57	11	31.28	105
19.2	7.427	5.94	0.714	0.438	5.19	3.88	1.59	1.44	0.72	1.59	0.53	10	32.29	106
19.4	7.408	6.50	0.698	0.438	5.24	3.88	1.56	1.44	0.70	1.56	0.54	10	32.61	108
19.6	7.554	5.49	0.740	0.439	5.33	4.01	1.63	1.45	0.79	1.63	0.57	11	32.55	112
19.8	7.546	6.04	0.722	0.438	5.55	4.24	1.61	1.43	0.79	1.61	0.58	10	33.13	115
20.0	7.199	7.51	0.660	0.437	5.58	4.12	1.46	1.46	0.62	1.46	0.61	13	29.97	126
20.5	7.560	5.21	0.750	0.440	5.65	4.33	1.65	1.46	0.79	1.64	0.56	13	30.89	130
21.0	7.235	7.18	0.669	0.437	6.12	4.72	1.50	1.49	0.71	1.50	0.70	10	34.68	131
21.5	7.541	5.78	0.730	0.439	6.04	4.74	1.61	1.45	0.80	1.61	0.59	14	29.99	138
22.0	7.522	7.85	0.676	0.436	6.54	5.11	1.52	1.36	0.92	1.52	0.72	11	34.00	142
22.5	7.110	7.57	0.651	0.436	6.76	5.31	1.49	1.43	0.68	1.49	0.58	11	34.09	152
23.0	7.551	5.34	0.745	0.439	6.95	5.53	1.64	1.46	0.90	1.63	0.68	11	34.78	163
23.5	7.881	3.09	0.911	0.444	7.16	5.75	1.93	1.58	1.19	1.92	0.87	12	32.84	159
24.0	7.933	2.55	0.978	0.446	7.36	5.80	2.08	1.64	1.34	2.07	0.98	12	35.19	192
24.5	8.029	2.35	1.026	0.446	7.50	5.98	2.21	1.67	1.47	2.20	1.07	13	34.04	201
25.0	8.037	2.65	0.985	0.445	7.62	6.32	2.17	1.59	1.43	2.17	1.02	19	26.21	159
25.5	7.660	3.54	0.844	0.443	8.28	6.73	1.70	1.62	1.08	1.87	0.82	14	33.94	220
26.0	7.612	4.26	0.796	0.441	8.47	6.88	1.74	1.53	1.15	1.74	0.90	15	31.55	208
26.5	7.735	3.89	0.832	0.443	8.45	6.80	1.80	1.54	1.19	1.80	0.90	16	31.13	229
27.0	7.649	4.48	0.790	0.441	8.56	7.09	1.73	1.52	1.12	1.73	0.89	18	29.29	211
27.5	7.529	6.01	0.721	0.438	9.23	7.57	1.54	1.46	1.14	1.59	0.96	16	32.80	252
28.0	7.509	5.81	0.726	0.438	9.04	7.51	1.53	1.46	1.06	1.60	0.88	21	26.55	205
28.5	7.679	5.84	0.740	0.439	9.44	7.68	1.63	1.43	1.22	1.62	0.98	19	30.36	264
29.0	7.702	4.46	0.797	0.441	10.02	8.27	1.73	1.49	1.26	1.72	1.01	15	34.19	281
29.5	7.767	4.88	0.785	0.441	10.04	8.27	1.71	1.45	1.29	1.70	1.00	15	33.51	272
30.0	7.774	4.26	0.816	0.442	9.95	8.24	1.76	1.50	1.24	1.75	0.97	20	29.48	284
30.5	7.772	4.08	0.825	0.442	10.50	8.70	1.77	1.51	1.36	1.77	1.09	14	35.80	289
31.0	7.872	3.58	0.871	0.443	10.56	8.72	1.85	1.54	1.46	1.84	1.15	15	35.36	303
31.5	7.893	3.07	0.915	0.444	11.21	9.40	1.94	1.58	1.56	1.93	1.24	18	33.28	347
32.0	7.934	3.12	0.917	0.444	11.26	9.41	1.95	1.57	1.60	1.94	1.27	15	36.76	381
32.5	7.938	2.93	0.936	0.445	11.62	9.75	1.99	1.59	1.65	1.98	1.30	18	33.99	375
33.0	7.978	2.65	0.975	0.445	11.95	9.93	2.08	1.63	1.77	2.08	1.41	16	35.34	380
33.5	7.989	2.52	0.993	0.446	12.06	10.09	2.13	1.64	1.79	2.12	1.42	24	29.32	398
34.0	8.013	2.56	0.993	0.446	12.14	10.41	2.13	1.64	1.85	2.12	1.48	16	36.51	391
34.5	8.007	2.46	1.002	0.445	12.53	10.72	2.20	1.65	1.91	2.19	1.52	19	33.36	396
35.0	8.026	2.39	1.016	0.445	12.62	10.75	2.25	1.66	1.95	2.24	1.56	21	31.99	415
36.0	7.999	2.22	1.039	0.447	13.11	10.88	2.34	1.80	2.06	2.33	1.73	17	35.34	426
37.0	8.069	2.12	1.076	0.447	13.54	11.32	2.46	1.82	2.20	2.25	1.96	18	35.45	457
38.0	8.041	2.45	1.012	0.445	13.58	10.58	2.24	1.66	1.87	2.23	1.49	59	20.61	571
39.0	7.965	2.31	1.018	0.446	13.66	10.48	2.25	1.78	1.76	2.24	1.44	739	5.66	509
40.0	8.242	2.00	1.151	0.448	15.29	12.92	2.81	1.88	2.60	2.16	2.50	23	32.64	535
41.0	8.152	2.04	1.114	0.448	15.41	12.34	2.59	1.85	2.31	2.27	2.10	50	23.31	667
42.0	8.146	2.00	1.122	0.448	16.21	13.58	2.66	1.93	2.49	2.24	2.35	30	29.22	606
43.0	8.414	2.36	1.131	0.447	16.93	14.49	2.62	1.75	2.82	1.97	2.79	26	32.30	646
44.0	8.415	2.57	1.095	0.446	17.71	15.22	2.45	1.64	2.86	1.64	2.86	23	34.41	664
45.0	8.177	2.03	1.126	0.448	16.14	13.28	2.71	1.91	2.30	2.20	2.18	896	5.14	506
50.0	8.089	2.10	1.084	0.447	17.78	11.34	2.46	1.82	2.08	2.34	1.80	2,020	3.59	615
55.0	8.475	2.30	1.161	0.447	19.85	17.66	2.77	1.91	2.82	1.91	2.82	2,048	3.73	733
60.0	8.415	2.53	1.100	0.447	23.90	20.90	2.82	1.91	3.21	1.91	3.21	150	15.34	1119
65.0	8.348	2.34	1.116	0.448	25.23	21.89	2.82	1.95	3.16	1.97	3.15	1,830	4.28	1019
70.0	8.301	1.86	1.211	0.450	28.78	25.40	2.20	1.96	3.87	2.18	3.72	184	14.61	1390
75.0	8.370	1.79	1.268	0.452	29.49	25.66	3.36	2.04	3.71	2.15	3.63	2,305	4.01	1237
80.0	8.274	1.56	1.311	0.453	31.39	27.08	3.61	2.14	3.88	2.26	3.81	2,334	4.09	1378
85.0	8.504	1.29	1.574	0.458	34.33	31.25	6.79	2.03	4.17	2.42	4.05	2,526	4.05	1548
90.0	8.641	1.23	1.719	0.460	36.23	32.18	6.97	1.54	4.11	2.40	3.92	2,648	4.00	1630
95.0	8.282	1.22	1.499	0.458	33.31	33.23	7.47	2.04	4.26	2.53	4.11	1,214	7.22	3617
100.0	7.952	2.98	0.933	0.444	42.44	42.44	1.82	1.44	3.34	2.02	2.92	1.3	191.5	2144

TABLE 4
SUMMARY OF EXPLOSION MODELS

explosion model	energy (B)	piston location (initial mass cut)
A	0.3	$S = 4$ (base of O shell)
B	0.6	$S = 4$ (base of O shell)
C	0.9	$S = 4$ (base of O shell)
D	1.2	$S = 4$ (base of O shell)
E	1.5	$S = 4$ (base of O shell)
F	1.8	$S = 4$ (base of O shell)
G	2.4	$S = 4$ (base of O shell)
H	3.0	$S = 4$ (base of O shell)
I	5.0	$S = 4$ (base of O shell)
J	10.0	$S = 4$ (base of O shell)
P	1.2	iron core (drop in Y_e)
V	10.0	iron core (drop in Y_e)

TABLE 5
ADOPTED SOLAR ABUNDANCES

ion	mass frac.	ion	mass frac.	ion	mass frac.	ion	mass frac.	ion	mass frac.	ion	mass frac.
¹ H	7.11×10^{-1}	¹⁷ O	2.62×10^{-6}	³¹ P	7.59×10^{-6}	⁴² Ca	5.00×10^{-7}	⁵² Cr	1.64×10^{-5}	⁶³ Cu	6.72×10^{-7}
² H	2.76×10^{-5}	¹⁸ O	1.49×10^{-5}	³² S	3.96×10^{-4}	⁴³ Ca	1.07×10^{-7}	⁵³ Cr	1.89×10^{-6}	⁶⁵ Cu	3.09×10^{-7}
³ He	3.41×10^{-5}	¹⁹ F	4.67×10^{-7}	³³ S	3.22×10^{-6}	⁴⁴ Ca	1.69×10^{-6}	⁵⁴ Cr	4.80×10^{-7}	⁶⁴ Zn	1.12×10^{-6}
⁴ He	2.74×10^{-1}	²⁰ Ne	1.17×10^{-3}	³⁴ S	1.86×10^{-5}	⁴⁶ Ca	3.36×10^{-9}	⁵⁵ Mn	1.47×10^{-5}	⁶⁶ Zn	6.60×10^{-7}
⁶ Li	7.39×10^{-10}	²¹ Ne	2.94×10^{-6}	³⁶ S	8.00×10^{-8}	⁴⁸ Ca	1.66×10^{-7}	⁵⁴ Fe	7.73×10^{-5}	⁶⁷ Zn	9.86×10^{-8}
⁷ Li	1.05×10^{-8}	²² Ne	9.44×10^{-5}	³⁵ Cl	4.06×10^{-6}	⁴⁵ Sc	4.50×10^{-8}	⁵⁶ Fe	1.26×10^{-3}	⁶⁸ Zn	4.57×10^{-7}
⁹ Be	1.94×10^{-10}	²³ Na	3.87×10^{-5}	³⁷ Cl	1.37×10^{-6}	⁴⁶ Ti	2.69×10^{-7}	⁵⁷ Fe	2.96×10^{-5}	⁷⁰ Zn	1.56×10^{-8}
¹⁰ B	1.00×10^{-9}	²⁴ Mg	5.65×10^{-4}	³⁶ Ar	9.13×10^{-5}	⁴⁷ Ti	2.47×10^{-7}	⁵⁸ Fe	4.00×10^{-6}	⁶⁹ Ga	4.36×10^{-8}
¹¹ B	4.47×10^{-9}	²⁵ Mg	7.46×10^{-5}	³⁸ Ar	1.75×10^{-5}	⁴⁸ Ti	2.51×10^{-6}	⁵⁹ Co	4.01×10^{-6}	⁷¹ Ga	2.98×10^{-8}
¹² C	2.46×10^{-3}	²⁶ Mg	8.54×10^{-5}	⁴⁰ Ar	2.81×10^{-8}	⁴⁹ Ti	1.88×10^{-7}	⁵⁸ Ni	5.52×10^{-5}	⁷⁰ Ge	5.24×10^{-8}
¹³ C	2.98×10^{-5}	²⁷ Al	6.64×10^{-5}	³⁹ K	3.93×10^{-6}	⁵⁰ Ti	1.84×10^{-7}	⁶⁰ Ni	2.20×10^{-5}	⁷² Ge	7.03×10^{-8}
¹⁴ N	7.96×10^{-4}	²⁸ Si	7.55×10^{-4}	⁴⁰ K	6.28×10^{-9}	⁵⁰ V	1.05×10^{-9}	⁶¹ Ni	9.72×10^{-7}	⁷³ Ge	1.99×10^{-8}
¹⁵ N	3.13×10^{-6}	²⁹ Si	3.97×10^{-5}	⁴¹ K	2.98×10^{-7}	⁵¹ V	4.29×10^{-7}	⁶² Ni	3.15×10^{-6}	⁷⁴ Ge	9.37×10^{-8}
¹⁶ O	6.60×10^{-3}	³⁰ Si	2.71×10^{-5}	⁴⁰ Ca	7.13×10^{-5}	⁵⁰ Cr	8.17×10^{-7}	⁶⁴ Ni	8.27×10^{-7}	⁷⁶ Ge	2.00×10^{-8}

TABLE 6
 ^{14}N YIELDS, 1.2 B, STANDARD MIXING

mass (M_{\odot})	^{14}N (M_{\odot})	mass (M_{\odot})	^{14}N (M_{\odot})	mass (M_{\odot})	^{14}N (M_{\odot})	mass (M_{\odot})	^{14}N (M_{\odot})	mass (M_{\odot})	^{14}N (M_{\odot})	mass (M_{\odot})	^{14}N (M_{\odot})	mass (M_{\odot})	^{14}N (M_{\odot})
10.0	9.39×10^{-7}	12.0	1.66×10^{-6}	15.6	4.46×10^{-6}	18.1	2.18×10^{-6}	22.0	3.19×10^{-5}	31.0	8.89×10^{-7}	45.0	3.09×10^{-2}
10.2	4.06×10^{-7}	12.2	2.94×10^{-6}	15.8	2.21×10^{-6}	18.2	2.53×10^{-6}	22.5	1.46×10^{-5}	31.5	1.42×10^{-6}	50.0	1.05×10^{-1}
10.4	2.07×10^{-6}	12.4	3.39×10^{-6}	16.0	2.04×10^{-6}	18.3	2.35×10^{-6}	23.0	1.34×10^{-4}	32.0	1.06×10^{-6}	55.0	1.21×10^{-1}
10.5	1.17×10^{-6}	12.6	2.79×10^{-6}	16.2	2.01×10^{-6}	18.4	2.54×10^{-6}	23.5	1.09×10^{-5}	32.5	1.23×10^{-6}	60.0	3.74×10^{-5}
10.6	1.29×10^{-6}	12.8	2.57×10^{-6}	16.4	1.97×10^{-6}	18.5	2.21×10^{-6}	24.0	8.00×10^{-6}	33.0	1.05×10^{-6}	65.0	9.27×10^{-2}
10.7	1.39×10^{-6}	13.0	2.58×10^{-6}	16.6	2.30×10^{-6}	18.6	2.16×10^{-6}	24.5	8.02×10^{-6}	33.5	1.66×10^{-6}	70.0	4.38×10^{-5}
10.8	1.61×10^{-6}	13.2	2.44×10^{-6}	16.8	1.63×10^{-6}	18.7	1.83×10^{-6}	25.0	1.05×10^{-2}	34.0	9.32×10^{-7}	75.0	2.05×10^{-1}
10.9	1.19×10^{-6}	13.4	2.83×10^{-6}	17.0	1.72×10^{-6}	18.8	2.34×10^{-6}	25.5	1.73×10^{-5}	34.5	8.70×10^{-7}	80.0	2.25×10^{-1}
11.0	1.43×10^{-6}	13.6	2.94×10^{-6}	17.1	1.68×10^{-6}	18.9	2.43×10^{-6}	26.0	3.74×10^{-5}	35.0	9.18×10^{-7}	85.0	2.12×10^{-1}
11.1	1.65×10^{-6}	13.8	1.78×10^{-6}	17.2	1.76×10^{-6}	19.0	2.21×10^{-6}	26.5	7.72×10^{-6}	36.0	7.31×10^{-7}	90.0	3.35×10^{-1}
11.2	2.14×10^{-6}	14.0	2.18×10^{-6}	17.3	1.78×10^{-6}	19.2	2.06×10^{-6}	27.0	9.37×10^{-3}	37.0	7.00×10^{-7}	95.0	9.70×10^{-1}
11.3	1.46×10^{-6}	14.2	2.08×10^{-6}	17.4	1.79×10^{-6}	19.4	1.46×10^{-6}	27.5	2.94×10^{-5}	38.0	1.20×10^{-4}	100.0	2.71×10^{-6}
11.4	2.92×10^{-6}	14.4	2.23×10^{-6}	17.5	1.80×10^{-6}	19.6	1.85×10^{-6}	28.0	7.99×10^{-3}	39.0	2.42×10^{-2}		
11.5	1.42×10^{-6}	14.6	1.71×10^{-6}	17.6	2.51×10^{-6}	19.8	1.94×10^{-6}	28.5	3.43×10^{-5}	40.0	4.45×10^{-7}		
11.6	1.75×10^{-6}	14.8	1.59×10^{-6}	17.7	1.51×10^{-6}	20.0	2.30×10^{-5}	29.0	4.16×10^{-6}	41.0	6.79×10^{-6}		
11.7	1.80×10^{-6}	15.0	4.48×10^{-6}	17.8	1.97×10^{-6}	20.5	8.52×10^{-4}	29.5	2.21×10^{-6}	42.0	1.71×10^{-6}		
11.8	2.88×10^{-6}	15.2	6.52×10^{-6}	17.9	1.93×10^{-6}	21.0	1.39×10^{-5}	30.0	5.07×10^{-3}	43.0	4.31×10^{-7}		
11.9	3.21×10^{-6}	15.4	4.28×10^{-6}	18.0	2.57×10^{-6}	21.5	3.96×10^{-3}	30.5	1.27×10^{-6}	44.0	3.29×10^{-7}		

TABLE 7
 POSTSUPERNOVA YIELDS IN SOLAR MASSES, 0.6 B, STANDARD MIXING, $S = 4$ PISTON (CONTINUED)

isotope	10 M_{\odot}	12 M_{\odot}	15 M_{\odot}	20 M_{\odot}	25 M_{\odot}	35 M_{\odot}	50 M_{\odot}	75 M_{\odot}	100 M_{\odot}
⁵⁹ Co	1.17×10^{-4}	4.94×10^{-5}	1.17×10^{-5}	4.82×10^{-6}	1.80×10^{-6}	3.54×10^{-8}	8.01×10^{-6}	2.16×10^{-6}	2.82×10^{-6}
⁵⁸ Ni	7.97×10^{-4}	2.51×10^{-4}	5.52×10^{-5}	5.69×10^{-5}	1.09×10^{-5}	1.16×10^{-7}	1.08×10^{-4}	1.15×10^{-4}	6.65×10^{-5}
⁶⁰ Ni	1.08×10^{-3}	4.68×10^{-4}	1.36×10^{-4}	4.21×10^{-5}	3.99×10^{-5}	9.68×10^{-7}	1.42×10^{-4}	8.23×10^{-5}	2.24×10^{-5}
⁶¹ Ni	5.37×10^{-5}	2.18×10^{-5}	6.41×10^{-6}	2.42×10^{-6}	1.87×10^{-6}	3.81×10^{-8}	7.41×10^{-6}	5.95×10^{-6}	1.50×10^{-6}
⁶² Ni	2.58×10^{-4}	9.42×10^{-5}	2.28×10^{-5}	1.23×10^{-5}	4.90×10^{-6}	8.59×10^{-8}	2.69×10^{-5}	2.63×10^{-5}	1.08×10^{-5}
⁶⁴ Ni	1.20×10^{-12}	1.67×10^{-12}	5.90×10^{-13}	2.19×10^{-13}	7.55×10^{-14}	2.50×10^{-15}	1.98×10^{-11}	1.78×10^{-12}	8.20×10^{-14}
⁶³ Cu	6.50×10^{-6}	4.36×10^{-6}	9.78×10^{-7}	1.45×10^{-7}	1.03×10^{-7}	3.59×10^{-9}	2.50×10^{-7}	5.83×10^{-8}	8.01×10^{-8}
⁶⁵ Cu	7.43×10^{-7}	3.34×10^{-7}	8.83×10^{-8}	3.17×10^{-8}	2.45×10^{-8}	5.72×10^{-10}	9.64×10^{-8}	6.97×10^{-8}	2.34×10^{-8}
⁶⁴ Zn	1.14×10^{-5}	7.69×10^{-6}	2.79×10^{-6}	2.91×10^{-7}	5.87×10^{-7}	2.54×10^{-8}	1.34×10^{-6}	3.65×10^{-7}	1.83×10^{-7}
⁶⁶ Zn	5.62×10^{-6}	2.15×10^{-6}	5.83×10^{-7}	2.73×10^{-7}	1.28×10^{-7}	2.44×10^{-9}	5.86×10^{-7}	6.69×10^{-7}	2.36×10^{-7}
⁶⁷ Zn	2.70×10^{-8}	1.92×10^{-8}	5.12×10^{-9}	1.54×10^{-9}	6.48×10^{-10}	1.14×10^{-11}	3.62×10^{-9}	2.75×10^{-9}	1.46×10^{-9}
⁶⁸ Zn	1.54×10^{-8}	1.22×10^{-8}	5.83×10^{-9}	3.66×10^{-10}	1.53×10^{-9}	1.51×10^{-10}	1.43×10^{-9}	3.79×10^{-10}	2.93×10^{-10}
⁷⁰ Zn	6.47×10^{-19}	7.41×10^{-19}	3.72×10^{-18}	2.18×10^{-19}	1.28×10^{-17}	1.26×10^{-22}	4.81×10^{-14}	7.07×10^{-15}	3.43×10^{-18}
⁶⁹ Ga	1.16×10^{-8}	7.35×10^{-9}	1.66×10^{-9}	2.81×10^{-10}	3.23×10^{-10}	1.23×10^{-11}	7.39×10^{-10}	2.38×10^{-10}	2.22×10^{-10}
⁷¹ Ga	1.50×10^{-9}	7.95×10^{-10}	2.17×10^{-10}	8.16×10^{-11}	3.95×10^{-11}	6.40×10^{-13}	1.70×10^{-10}	1.91×10^{-10}	6.89×10^{-11}
⁷⁰ Ge	1.46×10^{-7}	5.61×10^{-8}	1.77×10^{-8}	8.22×10^{-9}	4.18×10^{-9}	7.69×10^{-11}	1.69×10^{-8}	1.90×10^{-8}	6.00×10^{-9}
⁷² Ge	2.45×10^{-10}	1.23×10^{-10}	6.04×10^{-11}	1.98×10^{-11}	1.62×10^{-11}	1.97×10^{-12}	3.79×10^{-11}	5.14×10^{-11}	2.53×10^{-11}
⁷³ Ge	2.20×10^{-10}	1.65×10^{-10}	4.34×10^{-11}	4.64×10^{-12}	7.81×10^{-12}	3.67×10^{-13}	1.42×10^{-11}	3.82×10^{-12}	3.74×10^{-12}
⁷⁴ Ge	1.32×10^{-18}	1.18×10^{-18}	1.09×10^{-18}	3.72×10^{-19}	7.76×10^{-17}	5.32×10^{-22}	3.00×10^{-12}	2.19×10^{-13}	2.24×10^{-16}
⁷⁶ Ge	0.00	0.00	9.64×10^{-20}	0.00	8.23×10^{-18}	0.00	2.40×10^{-14}	3.85×10^{-15}	5.97×10^{-20}

TABLE 8
 POSTSUPERNOVA YIELDS IN SOLAR MASSES, 1.2 B, STANDARD MIXING, $S = 4$ PISTON (CONTINUED)

isotope	10 M_{\odot}	12 M_{\odot}	15 M_{\odot}	20 M_{\odot}	25 M_{\odot}	35 M_{\odot}	50 M_{\odot}	75 M_{\odot}	100 M_{\odot}
⁵⁹ Co	2.15×10^{-4}	1.65×10^{-4}	1.66×10^{-4}	1.74×10^{-4}	6.27×10^{-5}	1.01×10^{-6}	1.58×10^{-5}	4.40×10^{-6}	6.12×10^{-6}
⁵⁸ Ni	7.58×10^{-4}	4.87×10^{-4}	3.87×10^{-4}	1.95×10^{-3}	2.10×10^{-4}	1.93×10^{-6}	1.29×10^{-4}	1.65×10^{-4}	1.28×10^{-4}
⁶⁰ Ni	1.52×10^{-3}	1.32×10^{-3}	1.64×10^{-3}	1.83×10^{-3}	1.48×10^{-3}	2.61×10^{-5}	4.20×10^{-4}	1.87×10^{-4}	4.21×10^{-5}
⁶¹ Ni	6.07×10^{-5}	5.21×10^{-5}	6.30×10^{-5}	9.64×10^{-5}	5.98×10^{-5}	8.48×10^{-7}	1.88×10^{-5}	1.27×10^{-5}	2.52×10^{-6}
⁶² Ni	3.17×10^{-4}	2.43×10^{-4}	2.38×10^{-4}	4.57×10^{-4}	1.41×10^{-4}	1.63×10^{-6}	5.35×10^{-5}	3.87×10^{-5}	1.91×10^{-5}
⁶⁴ Ni	5.97×10^{-13}	2.40×10^{-12}	4.18×10^{-12}	5.60×10^{-12}	3.34×10^{-12}	7.80×10^{-14}	2.75×10^{-11}	2.56×10^{-12}	1.75×10^{-13}
⁶³ Cu	2.05×10^{-5}	1.47×10^{-5}	1.52×10^{-5}	6.21×10^{-6}	5.65×10^{-6}	1.67×10^{-7}	1.23×10^{-6}	9.95×10^{-8}	2.14×10^{-7}
⁶⁵ Cu	8.89×10^{-7}	8.11×10^{-7}	8.50×10^{-7}	1.19×10^{-6}	8.65×10^{-7}	1.56×10^{-8}	2.59×10^{-7}	1.73×10^{-7}	4.40×10^{-8}
⁶⁴ Zn	3.16×10^{-5}	3.08×10^{-5}	4.62×10^{-5}	1.79×10^{-5}	4.00×10^{-5}	1.13×10^{-6}	7.27×10^{-6}	8.99×10^{-7}	1.34×10^{-6}
⁶⁶ Zn	7.11×10^{-6}	5.60×10^{-6}	6.04×10^{-6}	1.01×10^{-5}	4.20×10^{-6}	6.05×10^{-8}	1.30×10^{-6}	9.83×10^{-7}	4.37×10^{-7}
⁶⁷ Zn	1.08×10^{-7}	9.82×10^{-8}	1.21×10^{-7}	5.09×10^{-8}	2.17×10^{-8}	4.16×10^{-10}	5.72×10^{-9}	5.42×10^{-9}	3.34×10^{-9}
⁶⁸ Zn	5.72×10^{-8}	6.29×10^{-8}	1.64×10^{-7}	3.20×10^{-8}	2.16×10^{-7}	7.12×10^{-9}	9.27×10^{-9}	8.34×10^{-10}	6.21×10^{-9}
⁷⁰ Zn	1.52×10^{-19}	2.96×10^{-19}	7.01×10^{-18}	3.16×10^{-18}	1.75×10^{-16}	1.24×10^{-21}	6.74×10^{-14}	1.39×10^{-14}	4.80×10^{-18}
⁶⁹ Ga	2.03×10^{-8}	2.14×10^{-8}	2.04×10^{-8}	1.11×10^{-8}	1.73×10^{-8}	4.18×10^{-10}	2.81×10^{-9}	8.28×10^{-10}	5.17×10^{-10}
⁷¹ Ga	3.01×10^{-9}	2.64×10^{-9}	3.45×10^{-9}	2.38×10^{-9}	1.08×10^{-9}	1.33×10^{-11}	3.17×10^{-10}	2.61×10^{-10}	1.30×10^{-10}
⁷⁰ Ge	1.78×10^{-7}	1.40×10^{-7}	1.79×10^{-7}	2.72×10^{-7}	1.35×10^{-7}	1.77×10^{-9}	4.06×10^{-8}	2.29×10^{-8}	1.10×10^{-8}
⁷² Ge	5.48×10^{-10}	4.99×10^{-10}	1.59×10^{-9}	6.91×10^{-10}	2.96×10^{-9}	1.09×10^{-10}	8.11×10^{-11}	3.86×10^{-11}	1.07×10^{-10}
⁷³ Ge	4.69×10^{-10}	4.76×10^{-10}	6.13×10^{-10}	2.09×10^{-10}	5.54×10^{-10}	1.51×10^{-11}	7.70×10^{-11}	9.42×10^{-12}	1.38×10^{-11}
⁷⁴ Ge	2.94×10^{-19}	7.88×10^{-19}	2.74×10^{-18}	5.94×10^{-18}	3.44×10^{-16}	6.15×10^{-21}	4.19×10^{-12}	3.18×10^{-13}	3.17×10^{-16}
⁷⁶ Ge	0.00	0.00	2.22×10^{-19}	0.00	9.75×10^{-17}	0.00	3.44×10^{-14}	8.36×10^{-15}	8.78×10^{-20}

TABLE 9
 POSTSUPERNOVA YIELDS IN SOLAR MASSES, 2.4 B, STANDARD MIXING, $S = 4$ PISTON (CONTINUED)

isotope	10 M_{\odot}	12 M_{\odot}	15 M_{\odot}	20 M_{\odot}	25 M_{\odot}	35 M_{\odot}	50 M_{\odot}	75 M_{\odot}	100 M_{\odot}
^{59}Co	3.83×10^{-4}	2.73×10^{-4}	3.55×10^{-4}	5.19×10^{-4}	3.34×10^{-4}	3.82×10^{-4}	1.35×10^{-4}	2.49×10^{-5}	5.07×10^{-5}
^{58}Ni	7.57×10^{-4}	5.08×10^{-4}	4.58×10^{-4}	4.46×10^{-3}	5.96×10^{-4}	7.89×10^{-4}	4.68×10^{-4}	7.02×10^{-4}	8.44×10^{-4}
^{60}Ni	1.99×10^{-3}	1.90×10^{-3}	3.10×10^{-3}	5.89×10^{-3}	7.05×10^{-3}	7.68×10^{-3}	4.14×10^{-3}	9.50×10^{-4}	3.02×10^{-4}
^{61}Ni	5.51×10^{-5}	6.05×10^{-5}	1.08×10^{-4}	2.88×10^{-4}	2.37×10^{-4}	2.06×10^{-4}	1.44×10^{-4}	5.86×10^{-5}	1.71×10^{-5}
^{62}Ni	3.42×10^{-4}	3.17×10^{-4}	3.86×10^{-4}	1.28×10^{-3}	5.04×10^{-4}	3.12×10^{-4}	3.01×10^{-4}	1.58×10^{-4}	1.32×10^{-4}
^{64}Ni	2.78×10^{-13}	1.57×10^{-12}	4.42×10^{-12}	1.10×10^{-11}	1.28×10^{-11}	2.11×10^{-11}	4.41×10^{-11}	5.53×10^{-12}	7.53×10^{-13}
^{63}Cu	4.70×10^{-5}	2.82×10^{-5}	4.78×10^{-5}	2.65×10^{-5}	5.66×10^{-5}	8.93×10^{-5}	2.95×10^{-5}	4.31×10^{-7}	1.12×10^{-6}
^{65}Cu	9.21×10^{-7}	9.77×10^{-7}	1.48×10^{-6}	3.48×10^{-6}	3.99×10^{-6}	5.02×10^{-6}	2.73×10^{-6}	8.24×10^{-7}	2.98×10^{-7}
^{64}Zn	5.26×10^{-5}	5.01×10^{-5}	1.14×10^{-4}	9.40×10^{-5}	2.96×10^{-4}	5.11×10^{-4}	1.93×10^{-4}	6.16×10^{-6}	8.04×10^{-6}
^{66}Zn	7.24×10^{-6}	6.90×10^{-6}	1.03×10^{-5}	2.96×10^{-5}	1.84×10^{-5}	1.85×10^{-5}	1.14×10^{-5}	3.67×10^{-6}	2.84×10^{-6}
^{67}Zn	2.22×10^{-7}	1.66×10^{-7}	3.37×10^{-7}	2.14×10^{-7}	2.48×10^{-7}	4.53×10^{-7}	5.44×10^{-8}	2.08×10^{-8}	3.02×10^{-8}
^{68}Zn	9.25×10^{-8}	9.07×10^{-8}	4.03×10^{-7}	2.94×10^{-7}	2.00×10^{-6}	3.31×10^{-6}	7.55×10^{-7}	5.34×10^{-8}	7.20×10^{-8}
^{70}Zn	3.37×10^{-20}	9.88×10^{-20}	3.49×10^{-18}	2.70×10^{-18}	3.90×10^{-16}	1.25×10^{-19}	9.19×10^{-14}	3.51×10^{-14}	9.73×10^{-18}
^{69}Ga	2.87×10^{-8}	2.95×10^{-8}	3.94×10^{-8}	4.12×10^{-8}	1.10×10^{-7}	1.83×10^{-7}	5.20×10^{-8}	1.28×10^{-8}	4.04×10^{-9}
^{71}Ga	4.53×10^{-9}	3.45×10^{-9}	7.71×10^{-9}	8.02×10^{-9}	5.89×10^{-9}	6.24×10^{-9}	2.02×10^{-9}	1.03×10^{-9}	1.01×10^{-9}
^{70}Ge	1.53×10^{-7}	1.54×10^{-7}	2.60×10^{-7}	8.25×10^{-7}	5.62×10^{-7}	4.59×10^{-7}	3.20×10^{-7}	9.47×10^{-8}	6.96×10^{-8}
^{72}Ge	7.28×10^{-10}	6.06×10^{-10}	3.57×10^{-9}	3.76×10^{-9}	3.00×10^{-8}	4.46×10^{-8}	9.78×10^{-9}	2.83×10^{-10}	1.09×10^{-9}
^{73}Ge	6.77×10^{-10}	5.96×10^{-10}	1.20×10^{-9}	9.92×10^{-10}	3.98×10^{-9}	5.44×10^{-9}	1.88×10^{-9}	9.48×10^{-11}	9.35×10^{-11}
^{74}Ge	5.57×10^{-20}	2.35×10^{-19}	1.21×10^{-18}	5.50×10^{-18}	3.25×10^{-16}	9.54×10^{-19}	5.62×10^{-12}	6.96×10^{-13}	6.37×10^{-16}
^{76}Ge	0.00	0.00	1.42×10^{-19}	0.00	1.77×10^{-16}	0.00	4.78×10^{-14}	2.09×10^{-14}	2.81×10^{-19}

TABLE 10
POSTSUPERNOVA YIELDS IN SOLAR MASSES, 5.0 B, STANDARD MIXING, $S = 4$ PISTON

isotope	35 M _⊙	50 M _⊙	75 M _⊙	100 M _⊙	isotope	35 M _⊙	50 M _⊙	75 M _⊙	100 M _⊙
¹ H	1.34×10 ¹	1.63×10 ¹	2.15×10 ¹	2.74×10 ¹	⁴² Ca	3.03×10 ⁻⁶	2.41×10 ⁻⁶	7.67×10 ⁻⁶	1.42×10 ⁻⁴
² H	7.62×10 ⁻⁷	1.72×10 ⁻⁸	3.39×10 ⁻⁸	4.91×10 ⁻⁹	⁴³ Ca	2.85×10 ⁻⁶	3.82×10 ⁻⁷	1.14×10 ⁻⁶	5.24×10 ⁻⁶
³ He	8.65×10 ⁻⁵	9.16×10 ⁻⁵	1.18×10 ⁻⁴	1.53×10 ⁻⁴	⁴⁴ Ca	1.24×10 ⁻⁴	1.53×10 ⁻⁴	1.85×10 ⁻⁴	2.09×10 ⁻⁴
⁴ He	1.04×10 ¹	1.55×10 ¹	2.46×10 ¹	2.82×10 ¹	⁴⁶ Ca	5.62×10 ⁻¹³	5.33×10 ⁻¹¹	1.80×10 ⁻¹¹	1.87×10 ⁻¹¹
⁶ Li	1.88×10 ⁻¹²	4.46×10 ⁻¹²	6.26×10 ⁻¹³	1.28×10 ⁻¹¹	⁴⁸ Ca	3.53×10 ⁻¹⁵	6.57×10 ⁻¹²	1.22×10 ⁻¹³	4.68×10 ⁻¹³
⁷ Li	1.18×10 ⁻⁵	5.06×10 ⁻⁸	5.99×10 ⁻⁸	1.41×10 ⁻⁸	⁴⁵ Sc	1.21×10 ⁻⁶	5.29×10 ⁻⁷	3.33×10 ⁻⁷	1.19×10 ⁻⁵
⁹ Be	7.52×10 ⁻¹²	3.62×10 ⁻¹¹	4.90×10 ⁻¹²	3.46×10 ⁻¹¹	⁴⁶ Ti	1.62×10 ⁻⁶	1.63×10 ⁻⁶	3.98×10 ⁻⁶	9.58×10 ⁻⁵
¹⁰ B	7.39×10 ⁻¹⁰	2.00×10 ⁻⁹	1.53×10 ⁻⁹	7.66×10 ⁻¹⁰	⁴⁷ Ti	4.34×10 ⁻⁶	4.48×10 ⁻⁶	2.51×10 ⁻⁶	1.92×10 ⁻⁵
¹¹ B	7.73×10 ⁻⁷	2.14×10 ⁻⁶	1.17×10 ⁻⁶	9.21×10 ⁻⁷	⁴⁸ Ti	5.63×10 ⁻⁴	6.89×10 ⁻⁴	6.38×10 ⁻⁴	6.58×10 ⁻⁴
¹² C	3.35×10 ⁻¹	1.86	1.70	1.00	⁴⁹ Ti	1.39×10 ⁻⁵	1.64×10 ⁻⁵	1.86×10 ⁻⁵	4.59×10 ⁻⁵
¹³ C	5.02×10 ⁻⁶	3.08×10 ⁻²	3.03×10 ⁻²	8.28×10 ⁻⁶	⁵⁰ Ti	2.97×10 ⁻¹¹	3.23×10 ⁻¹⁰	6.28×10 ⁻¹⁰	7.82×10 ⁻⁹
¹⁴ N	1.38×10 ⁻⁵	1.06×10 ⁻¹	2.07×10 ⁻¹	1.74×10 ⁻⁵	⁵⁰ V	2.00×10 ⁻⁹	2.45×10 ⁻⁹	1.06×10 ⁻⁸	9.63×10 ⁻⁷
¹⁵ N	1.00×10 ⁻⁴	1.18×10 ⁻⁴	2.02×10 ⁻⁴	1.20×10 ⁻⁴	⁵¹ V	4.93×10 ⁻⁵	5.42×10 ⁻⁵	4.42×10 ⁻⁵	9.40×10 ⁻⁵
¹⁶ O	6.39	1.11×10 ¹	1.37×10 ¹	3.18×10 ¹	⁵⁰ Cr	1.47×10 ⁻⁵	1.70×10 ⁻⁵	6.74×10 ⁻⁵	6.56×10 ⁻⁴
¹⁷ O	3.00×10 ⁻⁵	6.11×10 ⁻⁴	1.86×10 ⁻⁴	2.93×10 ⁻⁵	⁵² Cr	5.05×10 ⁻³	6.12×10 ⁻³	6.86×10 ⁻³	3.89×10 ⁻³
¹⁸ O	4.90×10 ⁻⁷	1.97×10 ⁻⁶	3.94×10 ⁻⁶	1.50×10 ⁻⁶	⁵³ Cr	2.48×10 ⁻⁴	3.01×10 ⁻⁴	4.17×10 ⁻⁴	5.14×10 ⁻⁴
¹⁹ F	3.82×10 ⁻⁵	3.68×10 ⁻⁵	4.27×10 ⁻⁵	6.27×10 ⁻⁶	⁵⁴ Cr	2.56×10 ⁻⁷	3.44×10 ⁻⁷	1.61×10 ⁻⁶	8.96×10 ⁻⁶
²⁰ Ne	1.12	1.22	1.95	1.56	⁵⁵ Mn	7.11×10 ⁻⁴	8.71×10 ⁻⁴	1.59×10 ⁻³	2.44×10 ⁻³
²¹ Ne	2.84×10 ⁻⁴	5.30×10 ⁻³	3.73×10 ⁻⁴	1.11×10 ⁻⁴	⁵⁴ Fe	1.05×10 ⁻³	1.41×10 ⁻³	6.38×10 ⁻³	3.34×10 ⁻²
²² Ne	7.96×10 ⁻⁵	1.28×10 ⁻²	9.30×10 ⁻⁵	6.79×10 ⁻⁵	⁵⁶ Fe	3.83×10 ⁻¹	4.86×10 ⁻¹	4.44×10 ⁻¹	2.99×10 ⁻¹
²³ Na	3.28×10 ⁻³	2.37×10 ⁻³	2.96×10 ⁻³	1.23×10 ⁻³	⁵⁷ Fe	8.58×10 ⁻³	1.09×10 ⁻²	9.68×10 ⁻³	1.28×10 ⁻²
²⁴ Mg	3.14×10 ⁻¹	3.00×10 ⁻¹	8.73×10 ⁻¹	9.74×10 ⁻¹	⁵⁸ Fe	1.61×10 ⁻⁷	1.80×10 ⁻⁷	3.73×10 ⁻⁷	1.17×10 ⁻⁵
²⁵ Mg	1.86×10 ⁻³	1.56×10 ⁻²	5.04×10 ⁻³	1.56×10 ⁻³	⁵⁹ Co	8.08×10 ⁻⁴	9.42×10 ⁻⁴	2.28×10 ⁻⁴	1.24×10 ⁻³
²⁶ Mg	2.10×10 ⁻³	1.69×10 ⁻²	5.76×10 ⁻³	1.01×10 ⁻³	⁵⁸ Ni	1.37×10 ⁻³	1.46×10 ⁻³	4.84×10 ⁻³	2.26×10 ⁻²
²⁷ Al	6.63×10 ⁻³	6.32×10 ⁻³	2.25×10 ⁻²	1.24×10 ⁻²	⁶⁰ Ni	1.08×10 ⁻²	1.34×10 ⁻²	8.92×10 ⁻³	8.35×10 ⁻³
²⁸ Si	2.12×10 ⁻¹	2.59×10 ⁻¹	5.41×10 ⁻¹	3.31	⁶¹ Ni	2.29×10 ⁻⁴	2.90×10 ⁻⁴	4.80×10 ⁻⁴	4.37×10 ⁻⁴
²⁹ Si	1.16×10 ⁻³	1.33×10 ⁻³	3.67×10 ⁻³	9.80×10 ⁻³	⁶² Ni	2.75×10 ⁻⁴	3.68×10 ⁻⁴	1.27×10 ⁻³	3.37×10 ⁻³
³⁰ Si	8.07×10 ⁻⁴	8.72×10 ⁻⁴	3.63×10 ⁻³	2.26×10 ⁻³	⁶⁴ Ni	2.71×10 ⁻¹¹	6.26×10 ⁻¹¹	1.05×10 ⁻¹¹	1.41×10 ⁻¹¹
³¹ P	4.25×10 ⁻⁴	4.89×10 ⁻⁴	1.47×10 ⁻³	3.13×10 ⁻³	⁶³ Cu	1.59×10 ⁻⁴	1.54×10 ⁻⁴	4.55×10 ⁻⁶	6.15×10 ⁻⁵
³² S	1.39×10 ⁻¹	1.80×10 ⁻¹	3.30×10 ⁻¹	2.55	⁶⁵ Cu	6.87×10 ⁻⁶	8.61×10 ⁻⁶	6.91×10 ⁻⁶	8.81×10 ⁻⁶
³³ S	1.98×10 ⁻⁴	2.27×10 ⁻⁴	3.39×10 ⁻⁴	4.79×10 ⁻³	⁶⁴ Zn	1.02×10 ⁻³	1.18×10 ⁻³	9.29×10 ⁻⁵	2.90×10 ⁻⁴
³⁴ S	2.47×10 ⁻⁴	2.86×10 ⁻⁴	6.53×10 ⁻⁴	4.66×10 ⁻³	⁶⁶ Zn	2.95×10 ⁻⁵	3.56×10 ⁻⁵	3.00×10 ⁻⁵	7.21×10 ⁻⁵
³⁶ S	2.35×10 ⁻⁸	2.86×10 ⁻⁸	4.41×10 ⁻⁸	3.09×10 ⁻⁷	⁶⁷ Zn	9.97×10 ⁻⁷	6.90×10 ⁻⁷	1.35×10 ⁻⁷	1.18×10 ⁻⁶
³⁵ Cl	9.17×10 ⁻⁵	1.11×10 ⁻⁴	1.74×10 ⁻⁴	1.30×10 ⁻³	⁶⁸ Zn	6.18×10 ⁻⁶	6.94×10 ⁻⁶	6.99×10 ⁻⁷	2.30×10 ⁻⁶
³⁷ Cl	2.70×10 ⁻⁵	2.31×10 ⁻⁵	4.05×10 ⁻⁵	8.30×10 ⁻⁴	⁷⁰ Zn	2.04×10 ⁻¹⁹	1.33×10 ⁻¹³	6.01×10 ⁻¹⁴	1.84×10 ⁻¹⁷
³⁶ Ar	2.51×10 ⁻²	3.10×10 ⁻²	5.08×10 ⁻²	3.39×10 ⁻¹	⁶⁹ Ga	2.71×10 ⁻⁷	2.95×10 ⁻⁷	1.29×10 ⁻⁷	1.39×10 ⁻⁷
³⁸ Ar	9.78×10 ⁻⁵	1.10×10 ⁻⁴	2.92×10 ⁻⁴	6.09×10 ⁻³	⁷¹ Ga	1.45×10 ⁻⁸	8.91×10 ⁻⁹	7.21×10 ⁻⁹	3.55×10 ⁻⁸
⁴⁰ Ar	1.69×10 ⁻¹⁰	4.94×10 ⁻¹⁰	5.81×10 ⁻¹⁰	5.37×10 ⁻⁹	⁷⁰ Ge	7.79×10 ⁻⁷	9.11×10 ⁻⁷	8.26×10 ⁻⁷	1.70×10 ⁻⁶
³⁹ K	4.90×10 ⁻⁵	5.39×10 ⁻⁵	1.47×10 ⁻⁴	1.41×10 ⁻³	⁷² Ge	7.50×10 ⁻⁸	9.49×10 ⁻⁸	4.49×10 ⁻⁹	3.28×10 ⁻⁸
⁴⁰ K	2.31×10 ⁻⁸	2.83×10 ⁻⁸	6.25×10 ⁻⁸	5.40×10 ⁻⁷	⁷³ Ge	8.22×10 ⁻⁹	1.04×10 ⁻⁸	1.59×10 ⁻⁹	3.44×10 ⁻⁹
⁴¹ K	1.29×10 ⁻⁵	6.74×10 ⁻⁶	1.37×10 ⁻⁵	2.99×10 ⁻⁴	⁷⁴ Ge	2.31×10 ⁻¹⁸	5.63×10 ⁻¹²	1.21×10 ⁻¹²	9.24×10 ⁻¹⁶
⁴⁰ Ca	2.29×10 ⁻²	2.68×10 ⁻²	4.01×10 ⁻²	2.45×10 ⁻¹	⁷⁶ Ge	0.00	8.38×10 ⁻¹⁴	3.40×10 ⁻¹⁴	7.60×10 ⁻¹⁹

TABLE 11
 POSTSUPERNOVA YIELDS IN SOLAR MASSES, 10.0 B, STANDARD MIXING, $S = 4$ PISTON

isotope	35 M_{\odot}	50 M_{\odot}	75 M_{\odot}	100 M_{\odot}	isotope	35 M_{\odot}	50 M_{\odot}	75 M_{\odot}	100 M_{\odot}
¹ H	1.34×10 ¹	1.63×10 ¹	2.15×10 ¹	2.74×10 ¹	⁴² Ca	4.91×10 ⁻⁶	4.52×10 ⁻⁶	2.29×10 ⁻⁵	1.43×10 ⁻⁴
² H	7.62×10 ⁻⁷	1.57×10 ⁻⁸	2.88×10 ⁻⁸	4.91×10 ⁻⁹	⁴³ Ca	6.84×10 ⁻⁶	2.96×10 ⁻⁶	4.42×10 ⁻⁶	9.70×10 ⁻⁶
³ He	8.58×10 ⁻⁵	9.16×10 ⁻⁵	1.18×10 ⁻⁴	1.53×10 ⁻⁴	⁴⁴ Ca	1.86×10 ⁻⁴	2.09×10 ⁻⁴	4.68×10 ⁻⁴	2.53×10 ⁻⁴
⁴ He	1.05×10 ¹	1.55×10 ¹	2.47×10 ¹	2.83×10 ¹	⁴⁶ Ca	5.53×10 ⁻¹³	5.33×10 ⁻¹¹	1.89×10 ⁻¹¹	1.46×10 ⁻¹¹
⁶ Li	1.57×10 ⁻¹²	3.55×10 ⁻¹²	5.27×10 ⁻¹³	9.78×10 ⁻¹²	⁴⁸ Ca	7.06×10 ⁻¹⁵	6.57×10 ⁻¹²	1.32×10 ⁻¹³	3.85×10 ⁻¹³
⁷ Li	1.34×10 ⁻⁵	3.64×10 ⁻⁸	6.23×10 ⁻⁸	1.29×10 ⁻⁸	⁴⁵ Sc	3.05×10 ⁻⁶	2.28×10 ⁻⁶	1.30×10 ⁻⁶	1.23×10 ⁻⁵
⁹ Be	7.10×10 ⁻¹²	3.14×10 ⁻¹¹	6.12×10 ⁻¹²	3.48×10 ⁻¹¹	⁴⁶ Ti	2.49×10 ⁻⁶	2.64×10 ⁻⁶	1.10×10 ⁻⁵	9.99×10 ⁻⁵
¹⁰ B	6.93×10 ⁻¹⁰	1.92×10 ⁻⁹	1.61×10 ⁻⁹	7.55×10 ⁻¹⁰	⁴⁷ Ti	7.04×10 ⁻⁶	6.51×10 ⁻⁶	5.94×10 ⁻⁶	2.46×10 ⁻⁵
¹¹ B	1.12×10 ⁻⁶	1.86×10 ⁻⁶	1.22×10 ⁻⁶	8.91×10 ⁻⁷	⁴⁸ Ti	7.40×10 ⁻⁴	8.75×10 ⁻⁴	2.47×10 ⁻³	7.95×10 ⁻⁴
¹² C	3.32×10 ⁻¹	1.85	1.70	1.00	⁴⁹ Ti	1.72×10 ⁻⁵	2.24×10 ⁻⁵	7.09×10 ⁻⁵	4.21×10 ⁻⁵
¹³ C	3.83×10 ⁻⁶	3.08×10 ⁻²	3.04×10 ⁻²	6.72×10 ⁻⁶	⁵⁰ Ti	1.60×10 ⁻¹¹	3.05×10 ⁻¹⁰	6.96×10 ⁻¹⁰	3.71×10 ⁻⁹
¹⁴ N	1.18×10 ⁻⁵	1.06×10 ⁻¹	2.07×10 ⁻¹	1.75×10 ⁻⁵	⁵⁰ V	1.24×10 ⁻⁹	1.61×10 ⁻⁹	2.01×10 ⁻⁸	4.57×10 ⁻⁷
¹⁵ N	7.82×10 ⁻⁵	9.47×10 ⁻⁵	2.25×10 ⁻⁴	1.13×10 ⁻⁴	⁵¹ V	6.35×10 ⁻⁵	7.59×10 ⁻⁵	1.45×10 ⁻⁴	1.03×10 ⁻⁴
¹⁶ O	6.23	1.10×10 ¹	1.65×10 ¹	3.19×10 ¹	⁵⁰ Cr	1.64×10 ⁻⁵	2.01×10 ⁻⁵	1.63×10 ⁻⁴	6.57×10 ⁻⁴
¹⁷ O	2.12×10 ⁻⁵	6.08×10 ⁻⁴	1.75×10 ⁻⁴	2.89×10 ⁻⁵	⁵² Cr	5.94×10 ⁻³	8.24×10 ⁻³	2.92×10 ⁻²	4.48×10 ⁻³
¹⁸ O	6.02×10 ⁻⁷	2.70×10 ⁻⁶	3.59×10 ⁻⁶	1.52×10 ⁻⁶	⁵³ Cr	2.91×10 ⁻⁴	3.82×10 ⁻⁴	1.58×10 ⁻³	5.27×10 ⁻⁴
¹⁹ F	2.75×10 ⁻⁵	2.64×10 ⁻⁵	3.63×10 ⁻⁵	6.09×10 ⁻⁶	⁵⁴ Cr	1.14×10 ⁻⁷	1.88×10 ⁻⁷	3.42×10 ⁻⁶	6.23×10 ⁻⁶
²⁰ Ne	1.03	1.17	1.98	1.56	⁵⁵ Mn	5.72×10 ⁻⁴	8.12×10 ⁻⁴	5.83×10 ⁻³	2.47×10 ⁻³
²¹ Ne	2.52×10 ⁻⁴	5.35×10 ⁻³	3.45×10 ⁻⁴	1.12×10 ⁻⁴	⁵⁴ Fe	7.33×10 ⁻⁴	1.18×10 ⁻³	1.74×10 ⁻²	3.36×10 ⁻²
²² Ne	7.22×10 ⁻⁵	1.23×10 ⁻²	8.23×10 ⁻⁵	6.78×10 ⁻⁵	⁵⁶ Fe	4.61×10 ⁻¹	6.09×10 ⁻¹	1.90	3.55×10 ⁻¹
²³ Na	2.97×10 ⁻³	2.06×10 ⁻³	2.85×10 ⁻³	1.23×10 ⁻³	⁵⁷ Fe	1.04×10 ⁻²	1.18×10 ⁻²	4.04×10 ⁻²	1.54×10 ⁻²
²⁴ Mg	3.06×10 ⁻¹	3.00×10 ⁻¹	1.07	9.75×10 ⁻¹	⁵⁸ Fe	1.42×10 ⁻⁷	1.55×10 ⁻⁷	1.50×10 ⁻⁶	8.82×10 ⁻⁶
²⁵ Mg	1.66×10 ⁻³	1.62×10 ⁻²	5.04×10 ⁻³	1.54×10 ⁻³	⁵⁹ Co	1.36×10 ⁻³	1.58×10 ⁻³	9.45×10 ⁻⁴	1.61×10 ⁻³
²⁶ Mg	1.90×10 ⁻³	1.69×10 ⁻²	5.67×10 ⁻³	1.01×10 ⁻³	⁵⁸ Ni	2.10×10 ⁻³	2.16×10 ⁻³	1.21×10 ⁻²	2.71×10 ⁻²
²⁷ Al	6.46×10 ⁻³	6.23×10 ⁻³	2.70×10 ⁻²	1.23×10 ⁻²	⁶⁰ Ni	1.41×10 ⁻²	1.82×10 ⁻²	3.90×10 ⁻²	1.06×10 ⁻²
²⁸ Si	2.70×10 ⁻¹	3.21×10 ⁻¹	1.45	3.28	⁶¹ Ni	2.57×10 ⁻⁴	3.05×10 ⁻⁴	1.63×10 ⁻³	5.19×10 ⁻⁴
²⁹ Si	1.29×10 ⁻³	1.51×10 ⁻³	6.57×10 ⁻³	9.71×10 ⁻³	⁶² Ni	3.43×10 ⁻⁴	3.59×10 ⁻⁴	4.28×10 ⁻³	4.15×10 ⁻³
³⁰ Si	8.88×10 ⁻⁴	9.80×10 ⁻⁴	5.58×10 ⁻³	2.23×10 ⁻³	⁶⁴ Ni	1.84×10 ⁻¹¹	5.36×10 ⁻¹¹	8.26×10 ⁻¹¹	8.29×10 ⁻¹²
³¹ P	4.71×10 ⁻⁴	5.56×10 ⁻⁴	2.52×10 ⁻³	2.87×10 ⁻³	⁶³ Cu	2.71×10 ⁻⁴	2.39×10 ⁻⁴	2.77×10 ⁻⁵	2.86×10 ⁻⁵
³² S	1.82×10 ⁻¹	2.28×10 ⁻¹	1.11	2.51	⁶⁵ Cu	8.70×10 ⁻⁶	1.14×10 ⁻⁵	2.33×10 ⁻⁵	1.11×10 ⁻⁵
³³ S	2.25×10 ⁻⁴	2.75×10 ⁻⁴	8.90×10 ⁻⁴	4.68×10 ⁻³	⁶⁴ Zn	1.47×10 ⁻³	1.73×10 ⁻³	7.00×10 ⁻⁴	2.88×10 ⁻⁴
³⁴ S	3.40×10 ⁻⁴	4.06×10 ⁻⁴	1.92×10 ⁻³	4.44×10 ⁻³	⁶⁶ Zn	3.96×10 ⁻⁵	4.39×10 ⁻⁵	1.10×10 ⁻⁴	8.09×10 ⁻⁵
³⁶ S	2.11×10 ⁻⁸	2.69×10 ⁻⁸	1.12×10 ⁻⁷	2.66×10 ⁻⁷	⁶⁷ Zn	1.66×10 ⁻⁶	2.18×10 ⁻⁶	6.51×10 ⁻⁷	1.68×10 ⁻⁶
³⁵ Cl	1.27×10 ⁻⁴	1.55×10 ⁻⁴	4.19×10 ⁻⁴	1.23×10 ⁻³	⁶⁸ Zn	8.75×10 ⁻⁶	1.33×10 ⁻⁵	1.12×10 ⁻⁵	3.39×10 ⁻⁶
³⁷ Cl	3.88×10 ⁻⁵	4.65×10 ⁻⁵	1.09×10 ⁻⁴	8.17×10 ⁻⁴	⁷⁰ Zn	9.35×10 ⁻²⁰	4.34×10 ⁻¹³	7.38×10 ⁻¹⁴	1.63×10 ⁻¹⁷
³⁶ Ar	3.32×10 ⁻²	4.15×10 ⁻²	1.82×10 ⁻¹	3.35×10 ⁻¹	⁶⁹ Ga	3.41×10 ⁻⁷	5.28×10 ⁻⁷	1.38×10 ⁻⁶	1.94×10 ⁻⁷
³⁸ Ar	1.24×10 ⁻⁴	1.57×10 ⁻⁴	8.93×10 ⁻⁴	6.02×10 ⁻³	⁷¹ Ga	2.70×10 ⁻⁸	3.20×10 ⁻⁸	4.14×10 ⁻⁸	4.52×10 ⁻⁸
⁴⁰ Ar	1.33×10 ⁻¹⁰	4.58×10 ⁻¹⁰	1.01×10 ⁻⁹	4.47×10 ⁻⁹	⁷⁰ Ge	1.08×10 ⁻⁶	1.15×10 ⁻⁶	2.93×10 ⁻⁶	1.76×10 ⁻⁶
³⁹ K	6.35×10 ⁻⁵	7.71×10 ⁻⁵	4.30×10 ⁻⁴	1.48×10 ⁻³	⁷² Ge	1.03×10 ⁻⁷	1.67×10 ⁻⁷	8.41×10 ⁻⁸	3.99×10 ⁻⁸
⁴⁰ K	1.86×10 ⁻⁸	2.48×10 ⁻⁸	1.40×10 ⁻⁷	4.71×10 ⁻⁷	⁷³ Ge	1.11×10 ⁻⁸	1.54×10 ⁻⁸	1.92×10 ⁻⁸	3.31×10 ⁻⁹
⁴¹ K	2.23×10 ⁻⁵	1.85×10 ⁻⁵	3.91×10 ⁻⁵	2.96×10 ⁻⁴	⁷⁴ Ge	9.38×10 ⁻¹⁹	5.59×10 ⁻¹²	1.23×10 ⁻¹²	9.21×10 ⁻¹⁶
⁴⁰ Ca	3.04×10 ⁻²	3.82×10 ⁻²	1.52×10 ⁻¹	2.43×10 ⁻¹	⁷⁶ Ge	0.00	3.15×10 ⁻¹³	4.29×10 ⁻¹⁴	7.60×10 ⁻¹⁹

TABLE 12
 POSTSUPERNOVA YIELDS IN SOLAR MASSES, 1.2 B, NO MIXING, $S = 4$ PISTON (CONTINUED)

isotope	10 M_{\odot}	12 M_{\odot}	15 M_{\odot}	20 M_{\odot}	25 M_{\odot}	35 M_{\odot}	50 M_{\odot}	75 M_{\odot}	100 M_{\odot}
⁵⁹ Co	2.09×10^{-4}	1.37×10^{-4}	9.92×10^{-16}	1.10×10^{-15}	1.51×10^{-14}	1.84×10^{-35}	1.25×10^{-11}	1.98×10^{-12}	3.93×10^{-14}
⁵⁸ Ni	7.55×10^{-4}	4.71×10^{-4}	4.55×10^{-17}	1.36×10^{-19}	1.10×10^{-18}	1.06×10^{-43}	3.18×10^{-15}	9.79×10^{-15}	2.54×10^{-20}
⁶⁰ Ni	1.50×10^{-3}	1.23×10^{-3}	1.58×10^{-15}	1.28×10^{-15}	1.53×10^{-14}	1.04×10^{-38}	1.62×10^{-11}	2.04×10^{-12}	3.20×10^{-14}
⁶¹ Ni	6.04×10^{-5}	5.10×10^{-5}	5.19×10^{-16}	3.58×10^{-16}	2.78×10^{-15}	1.63×10^{-41}	6.16×10^{-12}	7.03×10^{-13}	9.28×10^{-15}
⁶² Ni	3.17×10^{-4}	2.43×10^{-4}	5.84×10^{-16}	1.63×10^{-16}	4.16×10^{-15}	6.33×10^{-45}	1.25×10^{-11}	1.27×10^{-12}	1.41×10^{-14}
⁶⁴ Ni	5.55×10^{-13}	1.27×10^{-12}	2.30×10^{-16}	2.27×10^{-17}	9.40×10^{-15}	8.19×10^{-54}	3.19×10^{-11}	2.11×10^{-12}	9.93×10^{-15}
⁶³ Cu	1.87×10^{-5}	8.62×10^{-6}	2.56×10^{-16}	4.87×10^{-17}	4.48×10^{-15}	4.42×10^{-50}	1.19×10^{-11}	6.70×10^{-13}	4.38×10^{-15}
⁶⁵ Cu	8.77×10^{-7}	7.52×10^{-7}	5.13×10^{-17}	9.76×10^{-18}	1.79×10^{-15}	1.81×10^{-56}	7.14×10^{-12}	6.54×10^{-13}	3.46×10^{-15}
⁶⁴ Zn	2.84×10^{-5}	1.81×10^{-5}	1.05×10^{-20}	1.07×10^{-17}	2.45×10^{-18}	8.30×10^{-61}	3.32×10^{-13}	1.96×10^{-13}	2.09×10^{-15}
⁶⁶ Zn	7.05×10^{-6}	5.33×10^{-6}	1.10×10^{-16}	4.31×10^{-18}	1.36×10^{-15}	2.11×10^{-61}	8.74×10^{-12}	6.86×10^{-13}	2.85×10^{-15}
⁶⁷ Zn	9.12×10^{-8}	3.38×10^{-8}	1.84×10^{-17}	9.31×10^{-19}	5.04×10^{-16}	3.83×10^{-65}	2.07×10^{-12}	1.75×10^{-13}	5.80×10^{-16}
⁶⁸ Zn	4.98×10^{-8}	2.66×10^{-8}	1.78×10^{-17}	6.02×10^{-19}	1.77×10^{-15}	1.85×10^{-70}	1.52×10^{-11}	9.54×10^{-13}	2.52×10^{-15}
⁷⁰ Zn	1.52×10^{-19}	2.81×10^{-19}	6.67×10^{-18}	1.87×10^{-23}	1.75×10^{-16}	1.97×10^{-79}	8.12×10^{-14}	1.43×10^{-14}	5.26×10^{-18}
⁶⁹ Ga	1.98×10^{-8}	1.87×10^{-8}	1.40×10^{-17}	5.74×10^{-20}	3.23×10^{-16}	5.65×10^{-73}	2.13×10^{-12}	1.38×10^{-13}	3.03×10^{-16}
⁷¹ Ga	2.76×10^{-9}	1.65×10^{-9}	3.25×10^{-18}	2.54×10^{-22}	1.34×10^{-16}	1.68×10^{-82}	1.84×10^{-12}	1.16×10^{-13}	2.58×10^{-16}
⁷⁰ Ge	1.77×10^{-7}	1.36×10^{-7}	1.64×10^{-21}	1.45×10^{-20}	1.39×10^{-16}	6.08×10^{-83}	3.20×10^{-12}	1.65×10^{-13}	4.11×10^{-16}
⁷² Ge	4.87×10^{-10}	2.17×10^{-10}	4.49×10^{-18}	6.35×10^{-24}	2.67×10^{-16}	3.78×10^{-87}	3.62×10^{-12}	2.03×10^{-13}	3.59×10^{-16}
⁷³ Ge	4.43×10^{-10}	3.68×10^{-10}	1.08×10^{-18}	4.64×10^{-26}	1.22×10^{-16}	4.31×10^{-89}	1.17×10^{-12}	7.24×10^{-14}	9.93×10^{-17}
⁷⁴ Ge	2.91×10^{-19}	6.97×10^{-19}	1.50×10^{-18}	1.43×10^{-27}	3.43×10^{-16}	6.03×10^{-96}	4.98×10^{-12}	2.49×10^{-13}	3.56×10^{-16}
⁷⁶ Ge	0.00	0.00	2.22×10^{-19}	0.00	9.75×10^{-17}	0.00	4.29×10^{-14}	1.02×10^{-14}	1.84×10^{-20}

TABLE 13
 POSTSUPERNOVA YIELDS IN SOLAR MASSES, 1.2 B, STANDARD MIXING, Y_e PISTON (CONTINUED)

isotope	10 M_\odot	12 M_\odot	15 M_\odot	20 M_\odot	25 M_\odot	35 M_\odot	50 M_\odot	75 M_\odot	100 M_\odot
⁵⁹ Co	2.14×10^{-4}	1.21×10^{-4}	2.57×10^{-4}	1.64×10^{-4}	5.44×10^{-5}	3.90×10^{-6}	5.09×10^{-5}	2.55×10^{-6}	8.00×10^{-6}
⁵⁸ Ni	7.63×10^{-4}	6.18×10^{-4}	7.60×10^{-3}	1.92×10^{-3}	1.27×10^{-3}	7.88×10^{-5}	8.17×10^{-4}	1.05×10^{-4}	2.50×10^{-4}
⁶⁰ Ni	1.52×10^{-3}	1.26×10^{-3}	1.49×10^{-3}	1.72×10^{-3}	4.19×10^{-4}	2.93×10^{-5}	4.78×10^{-4}	1.04×10^{-4}	5.97×10^{-5}
⁶¹ Ni	6.04×10^{-5}	6.09×10^{-5}	1.31×10^{-4}	9.21×10^{-5}	2.97×10^{-5}	1.88×10^{-6}	2.73×10^{-5}	6.99×10^{-6}	4.06×10^{-6}
⁶² Ni	3.16×10^{-4}	2.79×10^{-4}	1.43×10^{-3}	4.45×10^{-4}	2.52×10^{-4}	1.54×10^{-5}	1.68×10^{-4}	2.38×10^{-5}	3.73×10^{-5}
⁶⁴ Ni	5.88×10^{-13}	1.43×10^{-12}	3.96×10^{-11}	4.78×10^{-12}	5.36×10^{-12}	2.92×10^{-13}	2.84×10^{-11}	1.86×10^{-12}	1.99×10^{-13}
⁶³ Cu	2.04×10^{-5}	7.18×10^{-6}	8.16×10^{-6}	4.33×10^{-6}	1.73×10^{-6}	1.22×10^{-7}	1.38×10^{-6}	6.04×10^{-8}	1.50×10^{-7}
⁶⁵ Cu	8.78×10^{-7}	9.14×10^{-7}	2.18×10^{-6}	1.12×10^{-6}	4.80×10^{-7}	2.61×10^{-8}	3.50×10^{-7}	1.08×10^{-7}	5.11×10^{-8}
⁶⁴ Zn	3.09×10^{-5}	1.68×10^{-5}	1.23×10^{-5}	1.24×10^{-5}	2.59×10^{-6}	1.85×10^{-7}	2.97×10^{-6}	6.57×10^{-7}	3.30×10^{-7}
⁶⁶ Zn	7.04×10^{-6}	6.72×10^{-6}	3.27×10^{-5}	9.71×10^{-6}	5.91×10^{-6}	3.45×10^{-7}	3.78×10^{-6}	6.16×10^{-7}	8.31×10^{-7}
⁶⁷ Zn	1.03×10^{-7}	2.84×10^{-8}	2.23×10^{-7}	4.31×10^{-8}	4.24×10^{-8}	2.01×10^{-9}	2.03×10^{-8}	3.53×10^{-9}	3.05×10^{-9}
⁶⁸ Zn	5.44×10^{-8}	2.50×10^{-8}	5.34×10^{-8}	1.41×10^{-8}	7.04×10^{-9}	4.26×10^{-10}	4.34×10^{-9}	1.45×10^{-9}	6.46×10^{-10}
⁷⁰ Zn	1.51×10^{-19}	1.29×10^{-18}	1.21×10^{-16}	4.05×10^{-18}	1.41×10^{-16}	5.70×10^{-19}	6.57×10^{-14}	9.91×10^{-15}	4.94×10^{-18}
⁶⁹ Ga	1.97×10^{-8}	2.21×10^{-8}	1.90×10^{-8}	9.64×10^{-9}	3.41×10^{-9}	1.91×10^{-10}	2.44×10^{-9}	6.17×10^{-10}	2.97×10^{-10}
⁷¹ Ga	2.90×10^{-9}	2.07×10^{-9}	9.25×10^{-9}	2.23×10^{-9}	1.71×10^{-9}	8.55×10^{-11}	9.18×10^{-10}	1.63×10^{-10}	1.41×10^{-10}
⁷⁰ Ge	1.75×10^{-7}	1.86×10^{-7}	8.05×10^{-7}	2.62×10^{-7}	1.54×10^{-7}	9.10×10^{-9}	1.05×10^{-7}	1.45×10^{-8}	2.17×10^{-8}
⁷² Ge	5.23×10^{-10}	3.79×10^{-10}	7.85×10^{-9}	5.19×10^{-10}	9.73×10^{-10}	5.36×10^{-11}	3.97×10^{-10}	3.04×10^{-11}	1.10×10^{-10}
⁷³ Ge	4.48×10^{-10}	4.60×10^{-10}	2.48×10^{-10}	1.49×10^{-10}	4.27×10^{-11}	2.54×10^{-12}	3.60×10^{-11}	6.76×10^{-12}	3.98×10^{-12}
⁷⁴ Ge	2.88×10^{-19}	1.65×10^{-18}	1.05×10^{-16}	6.72×10^{-18}	2.60×10^{-16}	4.44×10^{-19}	4.09×10^{-12}	2.29×10^{-13}	3.14×10^{-16}
⁷⁶ Ge	0.00	0.00	2.28×10^{-19}	0.00	7.28×10^{-17}	0.00	3.35×10^{-14}	6.00×10^{-15}	8.68×10^{-20}

TABLE 14
 POSTSUPERNOVA YIELDS IN SOLAR MASSES, 1.2 B, NO MIXING, Y_e PISTON (CONTINUED)

isotope	10 M_\odot	12 M_\odot	15 M_\odot	20 M_\odot	25 M_\odot	35 M_\odot	50 M_\odot	75 M_\odot	100 M_\odot
^{59}Co	2.08×10^{-4}	8.22×10^{-5}	9.81×10^{-16}	1.06×10^{-15}	1.52×10^{-14}	9.15×10^{-40}	1.19×10^{-11}	9.57×10^{-13}	3.89×10^{-14}
^{58}Ni	7.59×10^{-4}	4.10×10^{-4}	3.27×10^{-24}	1.27×10^{-19}	2.28×10^{-20}	5.17×10^{-46}	5.08×10^{-17}	3.28×10^{-18}	2.46×10^{-20}
^{60}Ni	1.50×10^{-3}	9.34×10^{-4}	1.58×10^{-15}	1.24×10^{-15}	1.53×10^{-14}	7.53×10^{-44}	1.58×10^{-11}	9.50×10^{-13}	3.16×10^{-14}
^{61}Ni	6.01×10^{-5}	4.47×10^{-5}	5.20×10^{-16}	3.45×10^{-16}	2.79×10^{-15}	3.50×10^{-48}	5.95×10^{-12}	2.67×10^{-13}	9.19×10^{-15}
^{62}Ni	3.16×10^{-4}	1.80×10^{-4}	5.84×10^{-16}	1.57×10^{-16}	4.15×10^{-15}	1.54×10^{-52}	1.21×10^{-11}	5.20×10^{-13}	1.39×10^{-14}
^{64}Ni	5.48×10^{-13}	6.75×10^{-13}	2.31×10^{-16}	2.19×10^{-17}	9.41×10^{-15}	4.60×10^{-61}	3.08×10^{-11}	9.76×10^{-13}	9.83×10^{-15}
^{63}Cu	1.86×10^{-5}	2.66×10^{-6}	2.58×10^{-16}	4.69×10^{-17}	4.48×10^{-15}	7.89×10^{-57}	1.15×10^{-11}	3.70×10^{-13}	4.34×10^{-15}
^{65}Cu	8.67×10^{-7}	5.95×10^{-7}	5.15×10^{-17}	9.43×10^{-18}	1.80×10^{-15}	1.74×10^{-65}	6.91×10^{-12}	2.56×10^{-13}	3.43×10^{-15}
^{64}Zn	2.78×10^{-5}	1.17×10^{-5}	7.50×10^{-26}	1.04×10^{-17}	2.43×10^{-18}	2.76×10^{-67}	3.22×10^{-13}	5.50×10^{-14}	2.07×10^{-15}
^{66}Zn	6.98×10^{-6}	4.29×10^{-6}	1.11×10^{-16}	4.16×10^{-18}	1.36×10^{-15}	1.49×10^{-69}	8.45×10^{-12}	2.70×10^{-13}	2.82×10^{-15}
^{67}Zn	8.72×10^{-8}	1.28×10^{-8}	1.85×10^{-17}	8.98×10^{-19}	5.05×10^{-16}	1.56×10^{-74}	2.00×10^{-12}	7.15×10^{-14}	5.74×10^{-16}
^{68}Zn	4.75×10^{-8}	1.63×10^{-8}	1.79×10^{-17}	5.78×10^{-19}	1.77×10^{-15}	4.08×10^{-79}	1.47×10^{-11}	3.99×10^{-13}	2.49×10^{-15}
^{70}Zn	1.50×10^{-19}	1.99×10^{-19}	6.73×10^{-18}	1.61×10^{-23}	1.78×10^{-16}	2.88×10^{-88}	7.85×10^{-14}	1.16×10^{-14}	5.21×10^{-18}
^{69}Ga	1.92×10^{-8}	1.23×10^{-8}	1.41×10^{-17}	5.51×10^{-20}	3.25×10^{-16}	1.21×10^{-83}	2.06×10^{-12}	5.96×10^{-14}	3.00×10^{-16}
^{71}Ga	2.66×10^{-9}	1.11×10^{-9}	3.27×10^{-18}	2.30×10^{-22}	1.34×10^{-16}	2.58×10^{-93}	1.78×10^{-12}	4.31×10^{-14}	2.55×10^{-16}
^{70}Ge	1.74×10^{-7}	1.20×10^{-7}	1.71×10^{-21}	1.38×10^{-20}	1.38×10^{-16}	3.07×10^{-92}	3.10×10^{-12}	6.12×10^{-14}	4.07×10^{-16}
^{72}Ge	4.66×10^{-10}	1.30×10^{-10}	4.53×10^{-18}	5.36×10^{-24}	2.67×10^{-16}	0.00	3.50×10^{-12}	8.50×10^{-14}	3.56×10^{-16}
^{73}Ge	4.24×10^{-10}	2.55×10^{-10}	1.09×10^{-18}	3.77×10^{-26}	1.22×10^{-16}	0.00	1.14×10^{-12}	3.16×10^{-14}	9.83×10^{-17}
^{74}Ge	2.85×10^{-19}	4.80×10^{-19}	1.51×10^{-18}	1.26×10^{-27}	3.43×10^{-16}	0.00	4.82×10^{-12}	1.08×10^{-13}	3.52×10^{-16}
^{76}Ge	0.00	0.00	2.28×10^{-19}	0.00	9.85×10^{-17}	0.00	4.14×10^{-14}	9.43×10^{-15}	1.83×10^{-20}

TABLE 16
⁵⁶Ni YIELDS (SOLAR MASSES), PISTON AT Y_e CORE

mass (M _⊙)	1.2 B (no mix)	1.2 B (mixed)	mass (M _⊙)	1.2 B (no mix)	1.2 B (mixed)	mass (M _⊙)	1.2 B (no mix)	1.2 B (mixed)	mass (M _⊙)	1.2 B (no mix)	1.2 B (mixed)
10.0	3.70×10 ⁻²	3.73×10 ⁻²	14.4	8.45×10 ⁻²⁷	5.05×10 ⁻²	18.7	9.71×10 ⁻²⁷	1.41×10 ⁻²	31.0	6.14×10 ⁻²⁸	2.04×10 ⁻³
10.2	1.16×10 ⁻¹	1.16×10 ⁻¹	14.6	1.61×10 ⁻²⁷	4.15×10 ⁻²	18.8	1.58×10 ⁻²⁶	2.02×10 ⁻²	31.5	1.14×10 ⁻²⁷	2.23×10 ⁻³
10.4	4.41×10 ⁻²	4.24×10 ⁻²	14.8	1.47×10 ⁻²⁷	4.08×10 ⁻²	18.9	2.30×10 ⁻²⁶	1.81×10 ⁻²	32.0	1.36×10 ⁻³⁹	1.72×10 ⁻³
10.5	2.16×10 ⁻²	2.15×10 ⁻²	15.0	1.51×10 ⁻²⁵	5.71×10 ⁻²	19.0	1.03×10 ⁻²¹	2.64×10 ⁻²	32.5	7.43×10 ⁻³¹	1.79×10 ⁻³
10.6	2.10×10 ⁻³	2.09×10 ⁻³	15.2	6.96×10 ⁻²⁶	6.19×10 ⁻²	19.2	1.11×10 ⁻²⁶	1.54×10 ⁻²	33.0	1.61×10 ⁻⁴⁰	1.56×10 ⁻³
10.7	1.90×10 ⁻²	1.89×10 ⁻²	15.4	3.86×10 ⁻²⁶	5.07×10 ⁻²	19.4	9.22×10 ⁻²⁷	1.39×10 ⁻²	33.5	2.74×10 ⁻²⁸	2.09×10 ⁻³
10.8	5.34×10 ⁻²	5.20×10 ⁻²	15.6	3.29×10 ⁻²⁶	4.72×10 ⁻²	19.6	4.94×10 ⁻²⁷	1.36×10 ⁻²	34.0	1.98×10 ⁻⁴⁰	1.37×10 ⁻³
10.9	1.26×10 ⁻¹	1.32×10 ⁻¹	15.8	2.70×10 ⁻²⁷	3.39×10 ⁻²	19.8	2.01×10 ⁻²⁴	1.76×10 ⁻²	34.5	5.72×10 ⁻⁴¹	1.45×10 ⁻³
11.0	8.38×10 ⁻²	9.72×10 ⁻²	16.0	1.74×10 ⁻²⁴	2.88×10 ⁻²	20.0	1.80×10 ⁻²¹	7.15×10 ⁻²	35.0	5.78×10 ⁻⁴¹	1.29×10 ⁻³
11.1	4.56×10 ⁻²	4.50×10 ⁻²	16.2	4.85×10 ⁻²⁸	2.69×10 ⁻²	20.5	1.28×10 ⁻²²	2.34×10 ⁻²	36.0	9.73×10 ⁻⁴²	9.98×10 ⁻⁴
11.2	4.76×10 ⁻²	4.40×10 ⁻²	16.4	5.19×10 ⁻²⁸	2.45×10 ⁻²	21.0	3.76×10 ⁻²⁵	1.17×10 ⁻²	37.0	7.76×10 ⁻⁴²	1.00×10 ⁻³
11.3	1.18×10 ⁻¹	1.14×10 ⁻¹	16.6	2.07×10 ⁻²⁷	2.43×10 ⁻²	21.5	4.76×10 ⁻²²	3.30×10 ⁻²	38.0	2.81×10 ⁻²⁴	4.76×10 ⁻³
11.4	1.38×10 ⁻¹	1.36×10 ⁻¹	16.8	5.16×10 ⁻²⁸	1.76×10 ⁻²	22.0	4.04×10 ⁻²⁴	1.56×10 ⁻²	39.0	1.38×10 ⁻²⁰	7.16×10 ⁻²
11.5	4.39×10 ⁻²	4.89×10 ⁻²	17.0	5.12×10 ⁻²⁸	1.72×10 ⁻²	22.5	4.35×10 ⁻²⁰	3.27×10 ⁻²	40.0	4.56×10 ⁻⁴¹	5.35×10 ⁻⁴
11.6	4.58×10 ⁻²	5.18×10 ⁻²	17.1	4.70×10 ⁻²⁸	1.87×10 ⁻²	23.0	1.26×10 ⁻²²	1.22×10 ⁻²	41.0	1.00×10 ⁻³¹	1.68×10 ⁻³
11.7	8.12×10 ⁻¹⁹	9.23×10 ⁻²	17.2	5.10×10 ⁻²⁸	1.46×10 ⁻²	23.5	3.41×10 ⁻²⁵	7.16×10 ⁻³	42.0	4.55×10 ⁻³⁴	9.11×10 ⁻⁴
11.8	1.92×10 ⁻⁴	1.15×10 ⁻¹	17.3	5.74×10 ⁻²⁸	2.44×10 ⁻²	24.0	1.06×10 ⁻²⁶	6.74×10 ⁻³	43.0	1.03×10 ⁻⁴⁴	3.36×10 ⁻⁴
11.9	9.62×10 ⁻³	1.14×10 ⁻¹	17.4	5.07×10 ⁻²⁷	1.96×10 ⁻²	24.5	9.77×10 ⁻²⁷	7.16×10 ⁻³	44.0	9.83×10 ⁻⁴⁴	2.13×10 ⁻⁴
12.0	3.31×10 ⁻²	3.76×10 ⁻²	17.5	5.85×10 ⁻²⁸	2.17×10 ⁻²	25.0	9.44×10 ⁻²⁴	1.74×10 ⁻²	45.0	4.45×10 ⁻²¹	5.22×10 ⁻²
12.2	2.16×10 ⁻²²	8.76×10 ⁻²	17.6	9.07×10 ⁻²⁸	2.10×10 ⁻²	25.5	1.62×10 ⁻¹⁰	1.07×10 ⁻¹	50.0	1.18×10 ⁻²⁰	2.16×10 ⁻²
12.4	3.48×10 ⁻²⁰	8.19×10 ⁻²	17.7	1.22×10 ⁻²⁷	1.90×10 ⁻²	26.0	2.58×10 ⁻¹⁰	5.68×10 ⁻²	55.0	1.19×10 ⁻¹⁹	3.63×10 ⁻²
12.6	5.67×10 ⁻²⁶	5.35×10 ⁻²	17.8	5.86×10 ⁻²⁸	1.79×10 ⁻²	26.5	1.02×10 ⁻²⁶	4.43×10 ⁻³	60.0	2.27×10 ⁻³³	5.38×10 ⁻⁴
12.8	6.77×10 ⁻¹¹	7.77×10 ⁻²	17.9	6.46×10 ⁻²⁸	2.01×10 ⁻²	27.0	1.32×10 ⁻⁹	1.71×10 ⁻¹	65.0	3.13×10 ⁻¹⁹	8.37×10 ⁻³
13.0	1.38×10 ⁻²	5.85×10 ⁻²	18.0	1.43×10 ⁻⁹	2.11×10 ⁻²	27.5	1.64×10 ⁻²⁵	6.46×10 ⁻³	70.0	2.14×10 ⁻³³	2.89×10 ⁻⁴
13.2	1.11×10 ⁻²⁶	6.57×10 ⁻²	18.1	2.09×10 ⁻²⁶	2.32×10 ⁻²	28.0	6.91×10 ⁻¹⁶	1.55×10 ⁻¹	75.0	1.26×10 ⁻²¹	4.30×10 ⁻³
13.4	1.16×10 ⁻²⁴	6.63×10 ⁻²	18.2	8.16×10 ⁻²⁸	1.77×10 ⁻²	28.5	6.13×10 ⁻²⁶	5.34×10 ⁻³	80.0	2.44×10 ⁻²¹	5.69×10 ⁻³
13.6	3.69×10 ⁻¹⁹	5.94×10 ⁻²	18.3	7.90×10 ⁻²⁸	1.74×10 ⁻²	29.0	9.01×10 ⁻²⁷	2.79×10 ⁻³	85.0	2.14×10 ⁻¹⁷	1.69×10 ⁻²
13.8	4.82×10 ⁻²³	5.43×10 ⁻²	18.4	1.87×10 ⁻⁹	6.50×10 ⁻²	29.5	4.98×10 ⁻²⁷	3.06×10 ⁻³	90.0	2.17×10 ⁻¹⁸	2.40×10 ⁻²
14.0	1.31×10 ⁻²⁶	5.73×10 ⁻²	18.5	1.85×10 ⁻²⁶	2.05×10 ⁻²	30.0	6.23×10 ⁻²³	6.22×10 ⁻²	95.0	2.19×10 ⁻¹⁸	1.67×10 ⁻²
14.2	6.53×10 ⁻²⁷	5.47×10 ⁻²	18.6	2.03×10 ⁻¹⁰	1.79×10 ⁻²	30.5	9.86×10 ⁻²⁸	1.97×10 ⁻³	100.0	2.73×10 ⁻²⁴	2.95×10 ⁻³

TABLE 17
 SUMMARY OF FITS/FIGURES

star or compilation	mass (M_{\odot})	IMF	E (B)	E^{exp}	mixing	χ	rank (#)	comment	figure
HE0107	20.5	–	0.6	–	0.0631	3.845	1		Fig. 13A
HE0107	27	–	0.6	–	0.1000	4.297	2		
HE0107	10.5	–	0.3	–	0.0063	1.856	1	C+N	Fig. 13B
HE0107	12.8	–	0.6	–	0.0251	2.183	2	C+N	
HE0107	18.1	–	0.3	–	0.0631	2.786	10	C+N	
HE0107	10.5	–	0.3	–	0.0063	1.958	1	C+N+O	
HE0107	17	± 0.1 dex	0.6	1.0	0.0025	1.571	1		Fig. 13C
HE0107	17	± 0.05 dex	0.6	0.5	0.0251	1.692	3		
HE0107	12	± 0.025 dex	0.3	0.0	0.0040	1.359	1	C+N	Fig. 13D
HE0107	12	± 0.025 dex	0.3	0.0	0.0040	1.472	1	C+N+O	
HE0107	10–40	-0.65	0.3	1.0	0.0040	1.752	1		Fig. 13E
HE0107	13.5–40	0.35	0.6	-0.5	0.0158	1.819	4		
HE0107	12–30	1.35	0.6	1.0	0.0251	1.974	11		Fig. 13F
HE0107	13.5–40	-0.65	0.6	-0.5	0.0158	1.820	1	C+N	
HE0107	12–30	1.35	0.6	1.0	0.0251	2.159	15	C+N	
HE0107	13.5–40	-0.65	0.6	-0.5	0.0158	1.750	1	C+N+O	
HE0107	13.5–100	1.35	0.9	-0.5	0.0158	3.870	1		Fig. 15A
HE0107	15–100	1.35	0.9	-0.5	0.0251	4.186	1	C+N	
HE0107	13.5–100	1.35	0.9	-0.5	0.0158	4.193	2	C+N	
HE0107	15–100	1.35	0.9	-0.5	0.0251	3.968	1	C+N+O	
HE0107	17–100	1.35	1.2	-1.0	0.0158	3.972	2	C+N+O	
HE0107	15–100	1.35	1.2	-0.5	0.0100	2.399	1	ignoring C,N	Fig. 15C
HE0107	10–100	1.35	1.2	0.0	0.1000	19.809	–	standard	Fig. 15E
HE1327	21.5	–	0.3	–	0.0631	4.051	1		Fig. 14A
HE1327	27	–	0.6	–	0.0631	5.241	2		
HE1327	21.5	–	0.6	–	0.0631	5.393	3		
HE1327	30	–	0.3	–	0.1000	7.693	9		
HE1327	65	–	0.3	–	0.1000	8.630	13		
HE1327	11.6	–	0.3	–	0.0158	2.941	1	C+N	Fig. 14B
HE1327	18.1	–	0.9	–	0.0398	2.979	2	C+N	
HE1327	18.1	–	0.9	–	0.0398	3.150	1	C+N+O	
HE1327	25	± 0.05 dex	0.3	0.5	0.0631	4.072	1		Fig. 14C
HE1327	30	± 0.05 dex	0.6	-1.0	0.0631	4.668	3		
HE1327	15	± 0.025 dex	0.9	0.5	0.0063	2.833	1	C+N	Fig. 14D
HE1327	15	± 0.025 dex	0.9	0.0	0.0063	2.907	2	C+N	
HE1327	15	± 0.025 dex	0.9	0.5	0.0063	2.983	1	C+N+O	
HE1327	15–40	1.35	0.3	-1.0	0.0398	3.620	1		Fig. 14E
HE1327	15–40	2.35	0.3	-0.5	0.0398	3.658	2		
HE1327	15–35	-0.65	0.3	-1.0	0.0398	3.699	3		
HE1327	13.5–17	3.35	0.9	0.0	0.0040	2.869	1	C+N	
HE1327	13.5–17	1.35	0.9	0.0	0.0040	2.892	3	C+N	Fig. 14F
HE1327	13.5–17	3.35	0.9	0.0	0.0040	3.036	1	C+N+O	
HE1327	20–100	1.35	1.2	-1.0	0.0158	7.189	1		Fig. 15B
HE1327	20–100	1.35	1.2	-1.0	0.0158	6.699	1	C+N	Fig. 15D
HE1327	20–100	1.35	1.2	-1.0	0.0158	6.663	1	C+N+O	
HE1327	10–100	1.35	1.2	0.0	0.1000	30.341	–	standard	Fig. 15F
Cayrel	11	± 0.3 dex	0.6	-1.0	0.0398	0.824	1		Fig. 12A
Cayrel	12	± 0.275 dex	0.6	-1.0	0.0398	0.849	2		
Cayrel	12	± 0.05 dex	1.2	0.0	0.0158	0.858	3		
Cayrel	12	± 0.1 dex	0.9	-1.0	0.0158	0.859	4		
Cayrel	11–15	-0.65	0.9	-1.0	0.0158	0.732	1		Fig. 12B
Cayrel	10–100	1.35	0.9	-1.0	0.0158	0.753	1		Fig. 12C
Cayrel	10–100	1.35	0.6	-1.0	0.0398	0.764	2		
Cayrel	10–100	1.35	0.6	-1.0	0.0251	0.764	3		
Cayrel	10–15	-0.65	1.2	0.0	0.0158	0.740	1		Fig. 12D
Cayrel	10–100	1.35	0.9	-1.0	0.1000	0.948	1		
Cayrel	10–100	1.35	1.2	0.0	0.1000	1.695	–	standard	Fig. 12E
Cayrel	10–100	1.35	1.8	1.0	0.1000	2.287	1	high energy	Fig. 12F
Cayrel	10–12	-0.65	0.6	1.0	0.0158	2.249	1	+Cr	
Cayrel	10–100	1.35	0.3	-1.0	0.0251	2.573	1	+Cr	
Cayrel	10–100	1.35	1.2	0.0	0.1000	3.828	–	+Cr, standard	

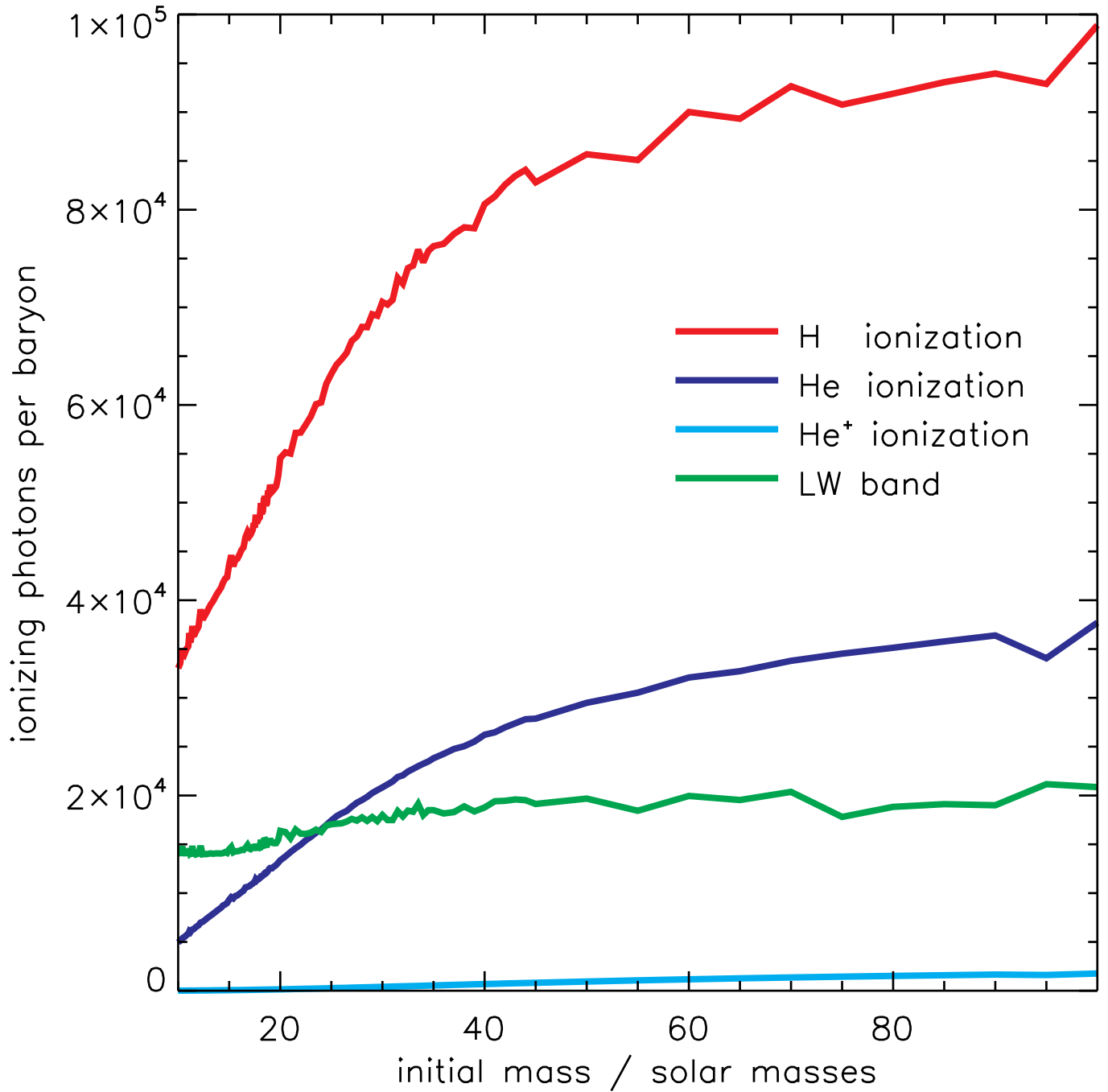


FIG. 1.— Ionizing radiation as a function of mass. Shown is the number of ionizing photons per baryon as a function on initial mass, for atomic hydrogen (red) and helium ionization (HeI to HeII, blue; HeII to HeIII, cyan), and for H_2 dissociation (Lyman-Werner band, green).

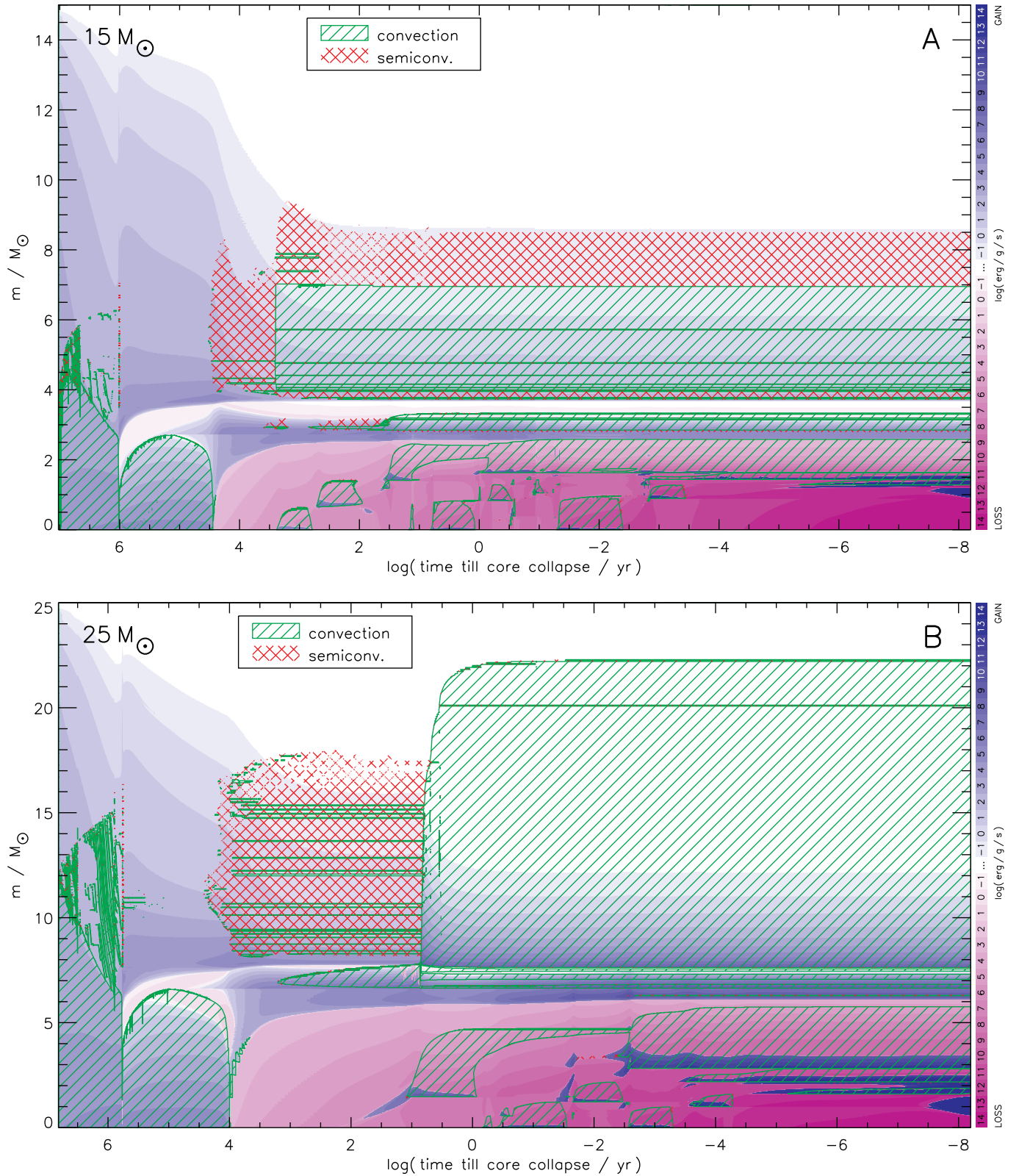


FIG. 2.— Kippenhahn diagram of $15 M_{\odot}$ and $25 M_{\odot}$ stars. As a function of time till core collapse (X-Axis, logarithmic scale) and mass coordinate of the star (Y-Axis) we show net specific energy generation (blue shades), net energy loss (purple shades), convective regions (green hatching) and semiconvective regions (red cross hatching). Energy generations and loss increase by one order of magnitude for each level of darker shading (scale on right hand side), ranging from $10^{-1} \text{ erg g}^{-1} \text{ s}^{-1}$ (lightest colors) to $10^{14} \text{ erg g}^{-1} \text{ s}^{-1}$ (darkest colors).

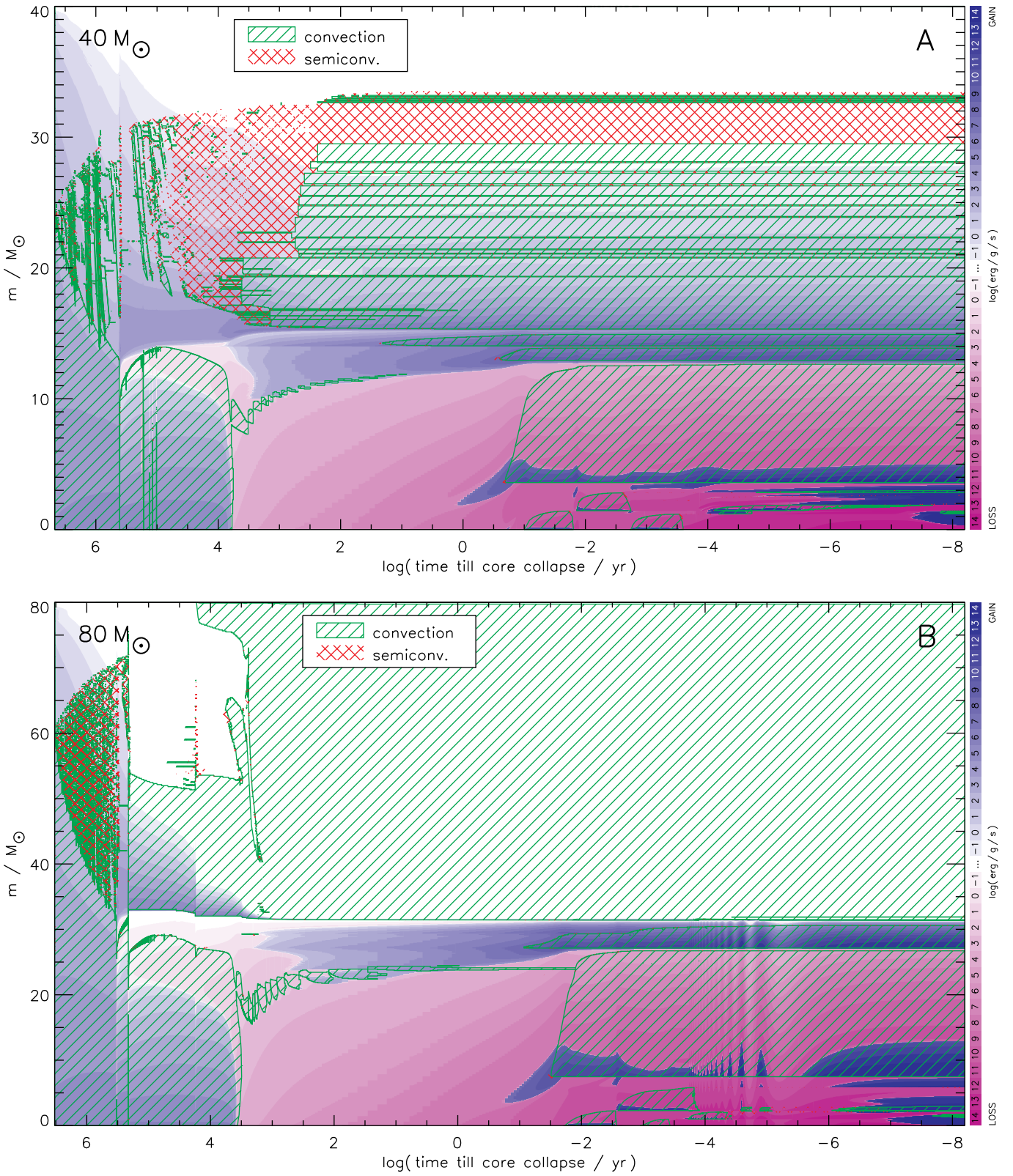


FIG. 3.— Kippenhahn diagram of $40 M_{\odot}$ and $80 M_{\odot}$ stars. See Fig. 2 for a detailed explanation.

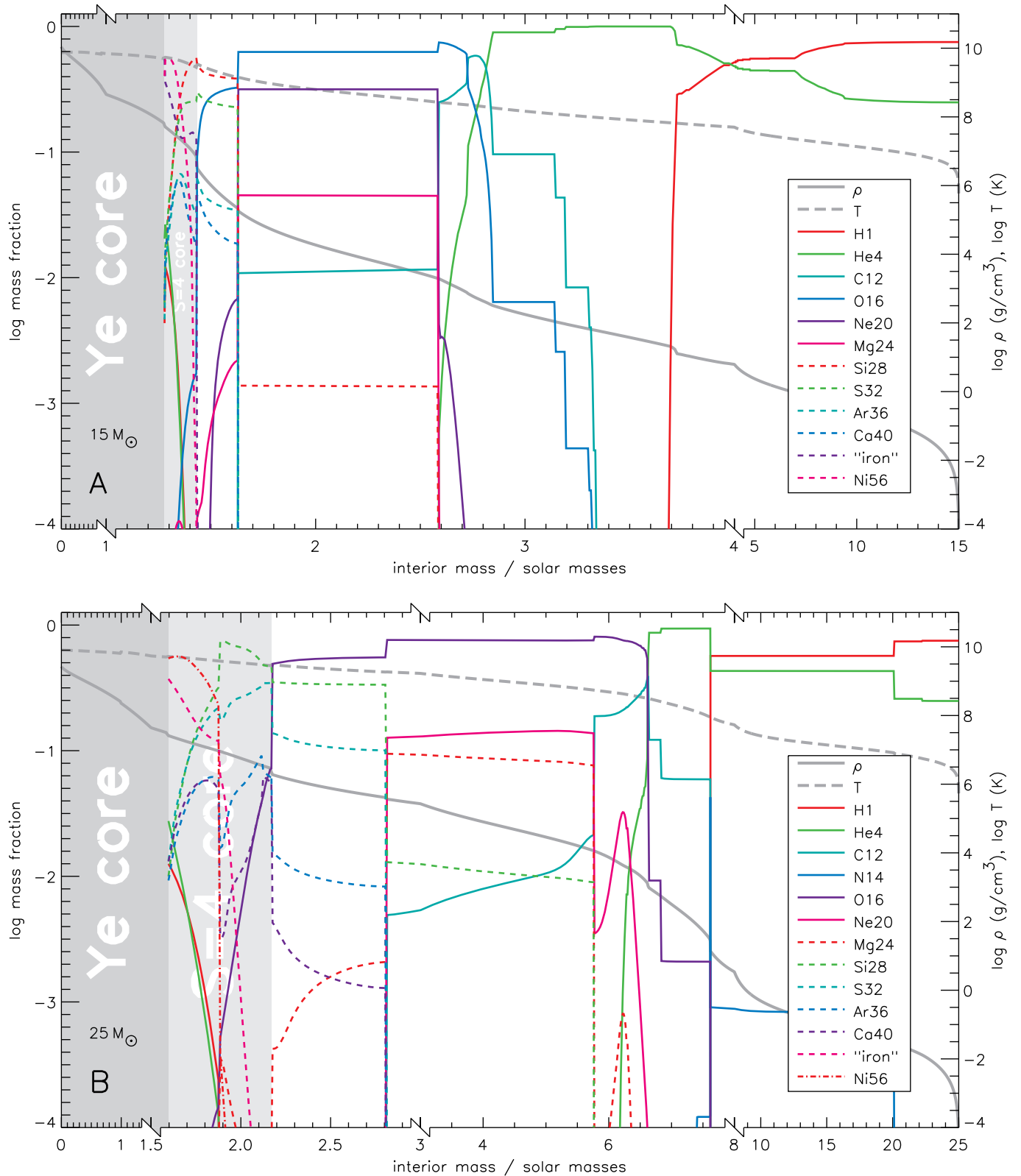


FIG. 4.— Composition and structure of the $15 M_{\odot}$ (Panel A) and $25 M_{\odot}$ (Panel B) presupernova stars. The left darker background shading indicates the “ Y_e ” core, the lighter shading right of it the $S = 4$ core.

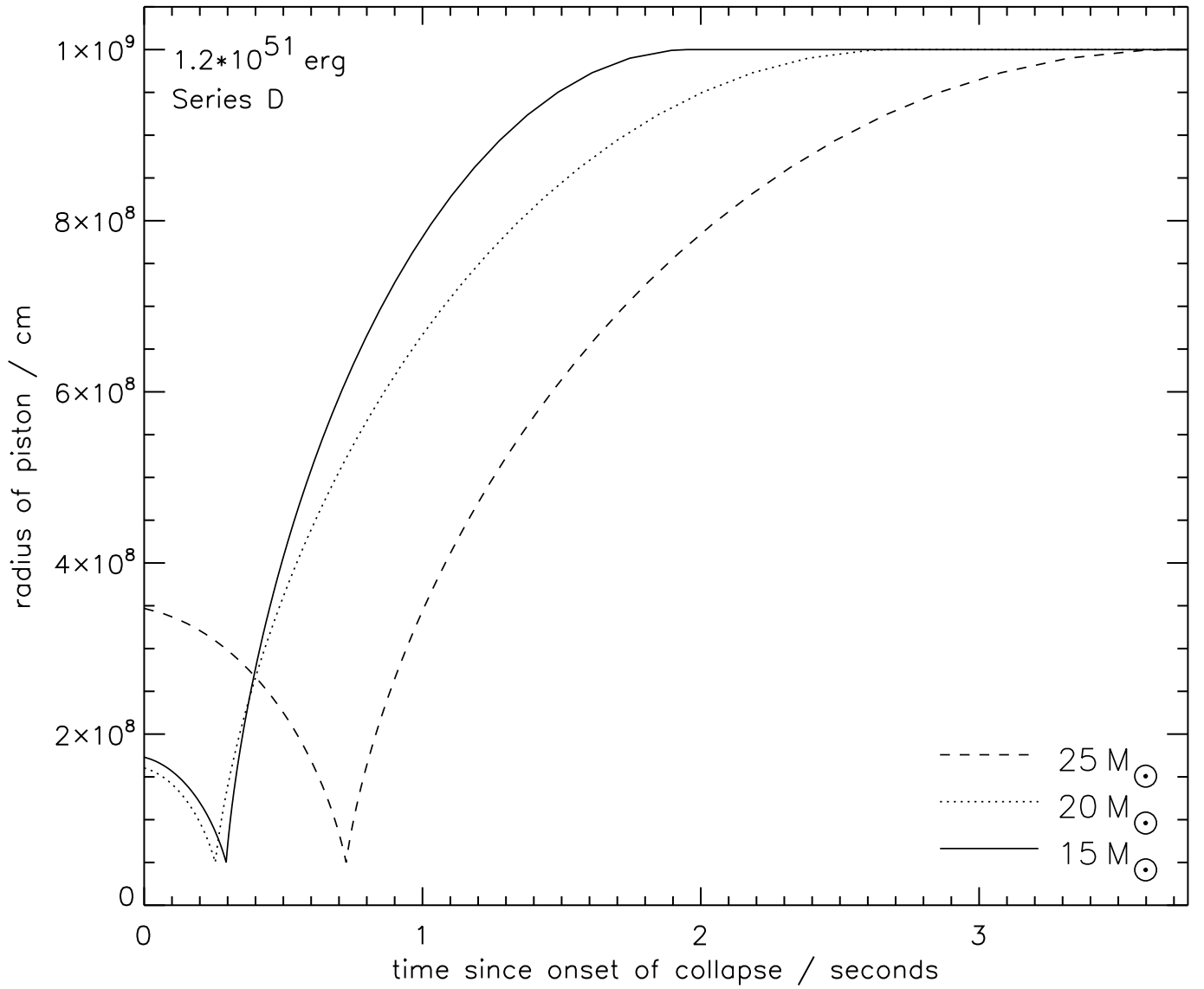


FIG. 5.— Piston location as a function of time for the 15, 20, and 25 M_{\odot} stars. When a piston location of 10^9 cm is reached the piston is stopped. “Onset of collapse” is defined as the time when a peak infall velocity of 900 km s^{-1} is reached.

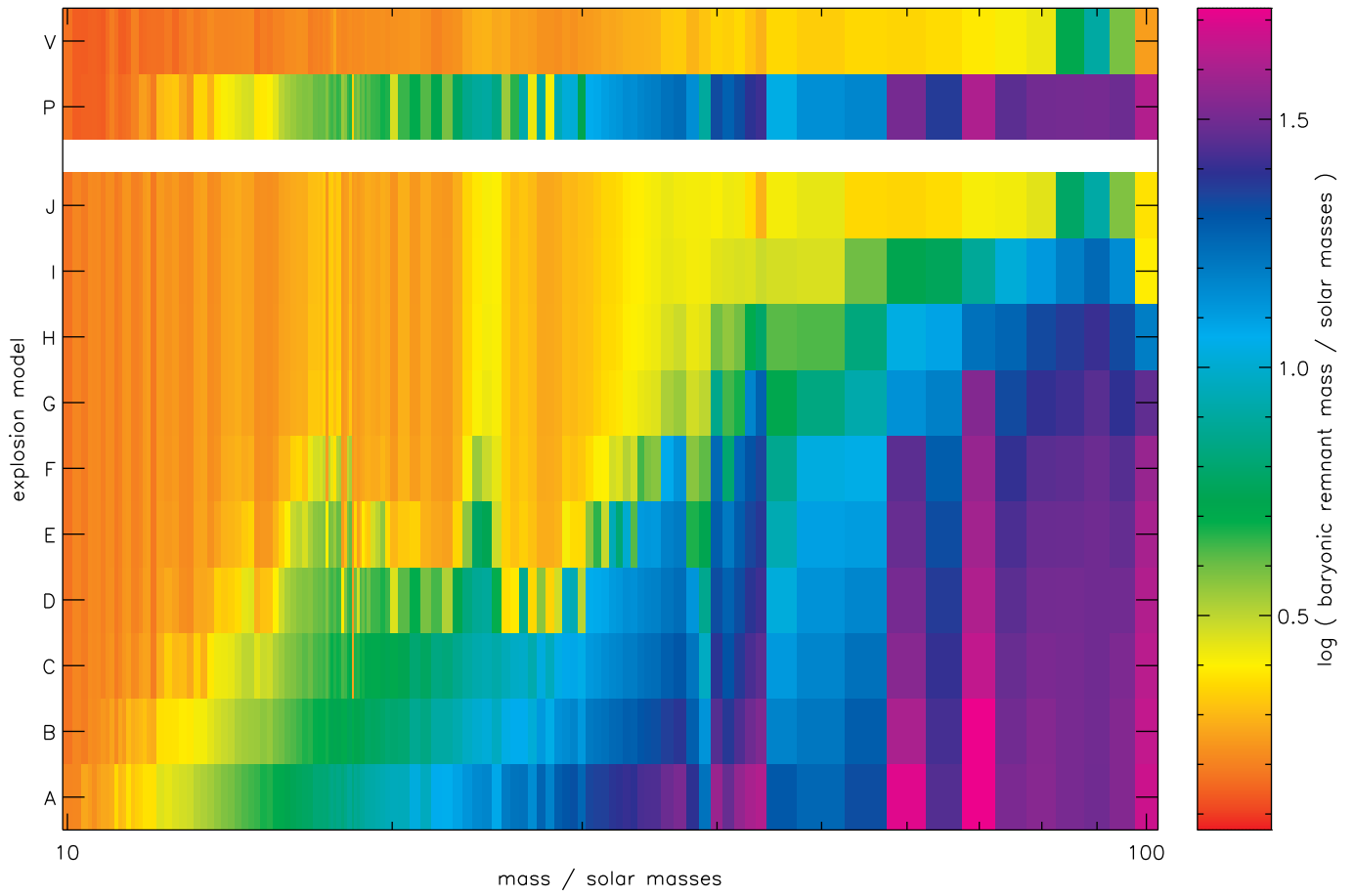


FIG. 6.— Remnant mass as a function of stellar mass (x -axis) and explosion model (y -axis). Remnant masses are color-coded. As a result of essentially negligible fallback, at low mass and high explosion energy the color remains constant for a given stellar mass, however, there are still star-to-star variations.

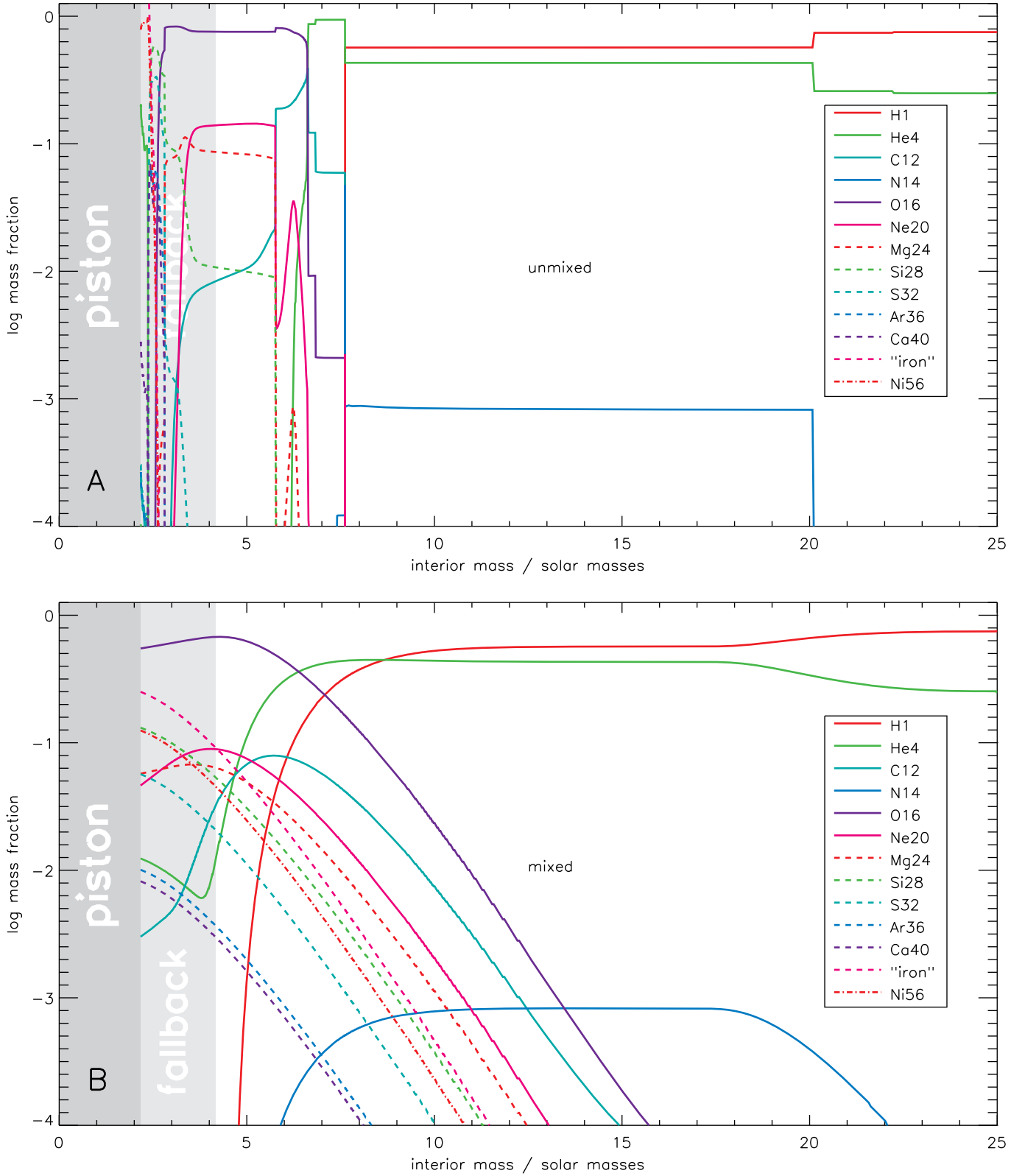


FIG. 7.— Composition of Model z25D ($25 M_{\odot}$, 1.2 B, piston at $S/N_A k_B = 4$) before (**Panel A**) and after (**Panel B**) the standard mixing operation. All explosions were routinely mixed in this fashion unless otherwise specified in the text. The mixing operation is carried out 100 s into the explosion before any significant fallback occurs. The leftmost dark shading indicates the mass of the piston (remnant before fallback); the lighter gray region to its right indicates the mass that falls back. None of the ^{56}Ni comes out without the mixing. The “iron” composition comprises everything heavier than calcium except for ^{56}Ni .

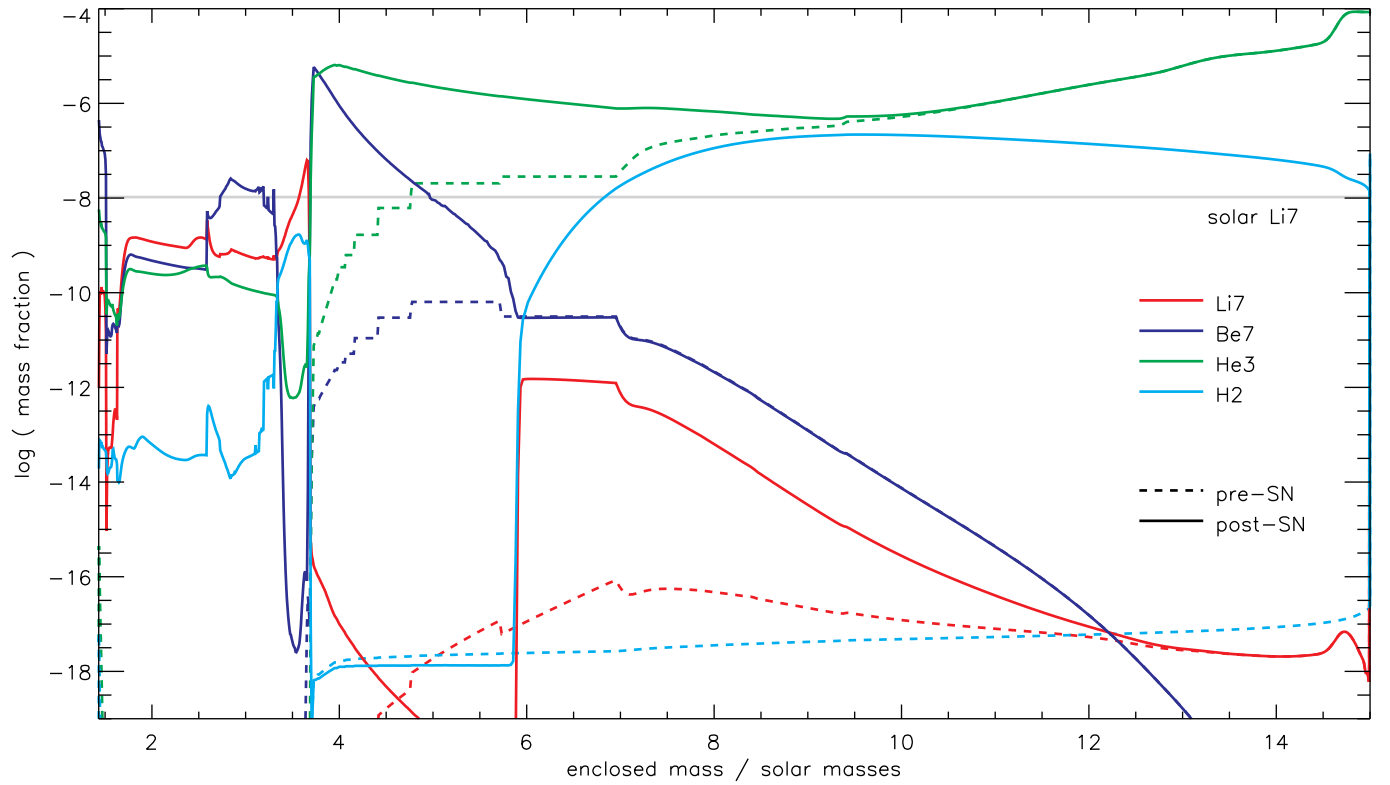


FIG. 8.— Supernova ${}^7\text{Li}$ production in the $15 M_{\odot}$ star for an explosion energy of 1.2 B. The *dashed* curves shows the mass fractions of ${}^2\text{H}$, (*magenta line*), ${}^3\text{He}$ (*green*), ${}^7\text{Li}$ (*red*) and ${}^7\text{Be}$ (*blue*) as a function of the enclosed mass at onset of core collapse (before the supernova). The *solid* lines show these mass fractions 100 s after core collapse and without mixing. At this time the supernova shock has propagated to a mass coordinate of about $5.9 M_{\odot}$; the edge of the helium core is located at about $3.7 M_{\odot}$. The post-SN ${}^7\text{Be}$, which later decays to ${}^7\text{Li}$, is well above the solar value for ${}^7\text{Li}$ (*gray line*) at the inner edge of the hydrogen envelope and causes a significant overproduction of ${}^7\text{Li}$ (observe logarithmic scale for ${}^7\text{Li}$ (*gray line*)). The ${}^7\text{Be}$ is made by the reaction ${}^1\text{H}(\bar{\nu}_e, e^+)n(p, \gamma){}^2\text{H}(p, \gamma){}^3\text{He}(\alpha, \gamma){}^7\text{Be}$ initiated by supernova neutrinos. This reaction is only efficient here due to the compactness of the hydrogen envelope of the primordial stars. The neutrons made from neutrino interactions quickly from ${}^2\text{H}$. Below $\sim 8 M_{\odot}$ most of the ${}^2\text{H}$ has quickly reacted to make ${}^3\text{He}$. Much of the ${}^7\text{Be}$ is then synthesized in the supernova shock.

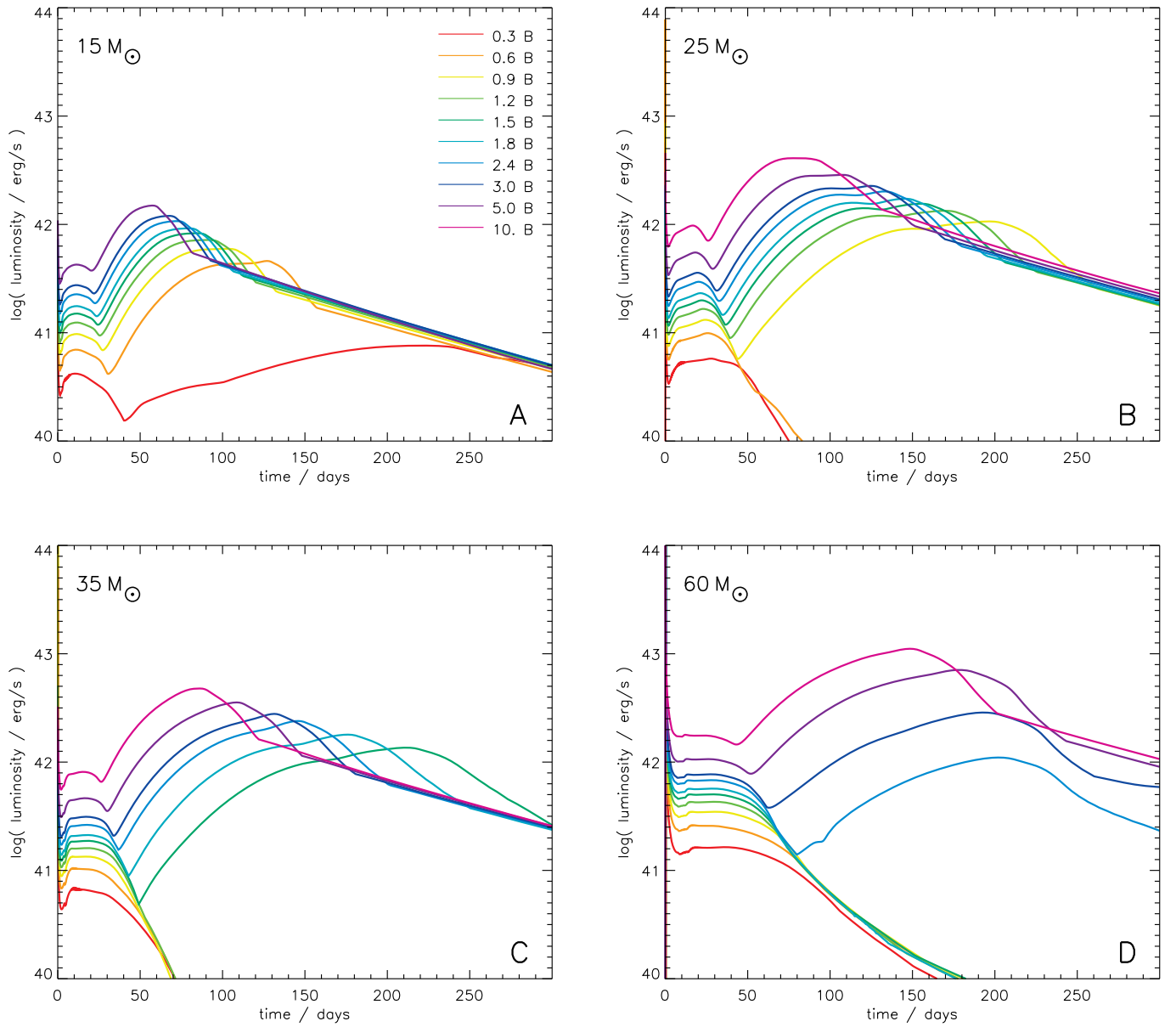


FIG. 9.— Bolometric light curves for the 15 M_{\odot} (Panel A), 25 M_{\odot} (Panel B), 35 M_{\odot} (Panel C), and 60 M_{\odot} (Panel D) stars calculated for a variety of explosion energies.

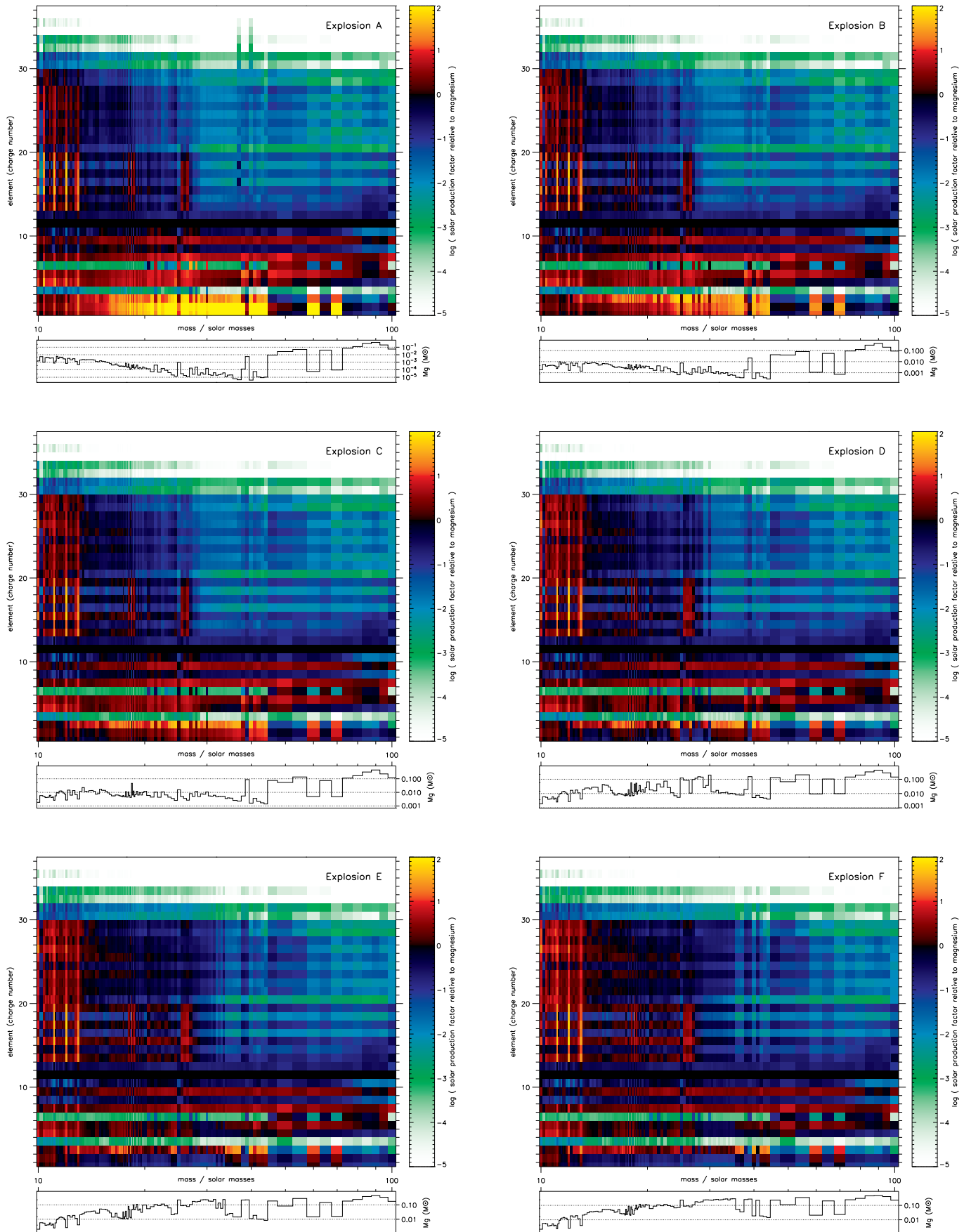


FIG. 10.— Elemental production factors relative to solar as a function of mass for the 0.3–1.8 B explosions (Explosion Models A–F). The production factors are normalized to a solar yield of magnesium and color coded according to the scale on the right hand side. The absolute yield of magnesium as a function of mass is given below each map. Darker colors correspond to about solar co-production with magnesium; red through yellow, to overproduction, and blue through green and white, to underproduction. (CONTINUED ON NEXT PAGE.)

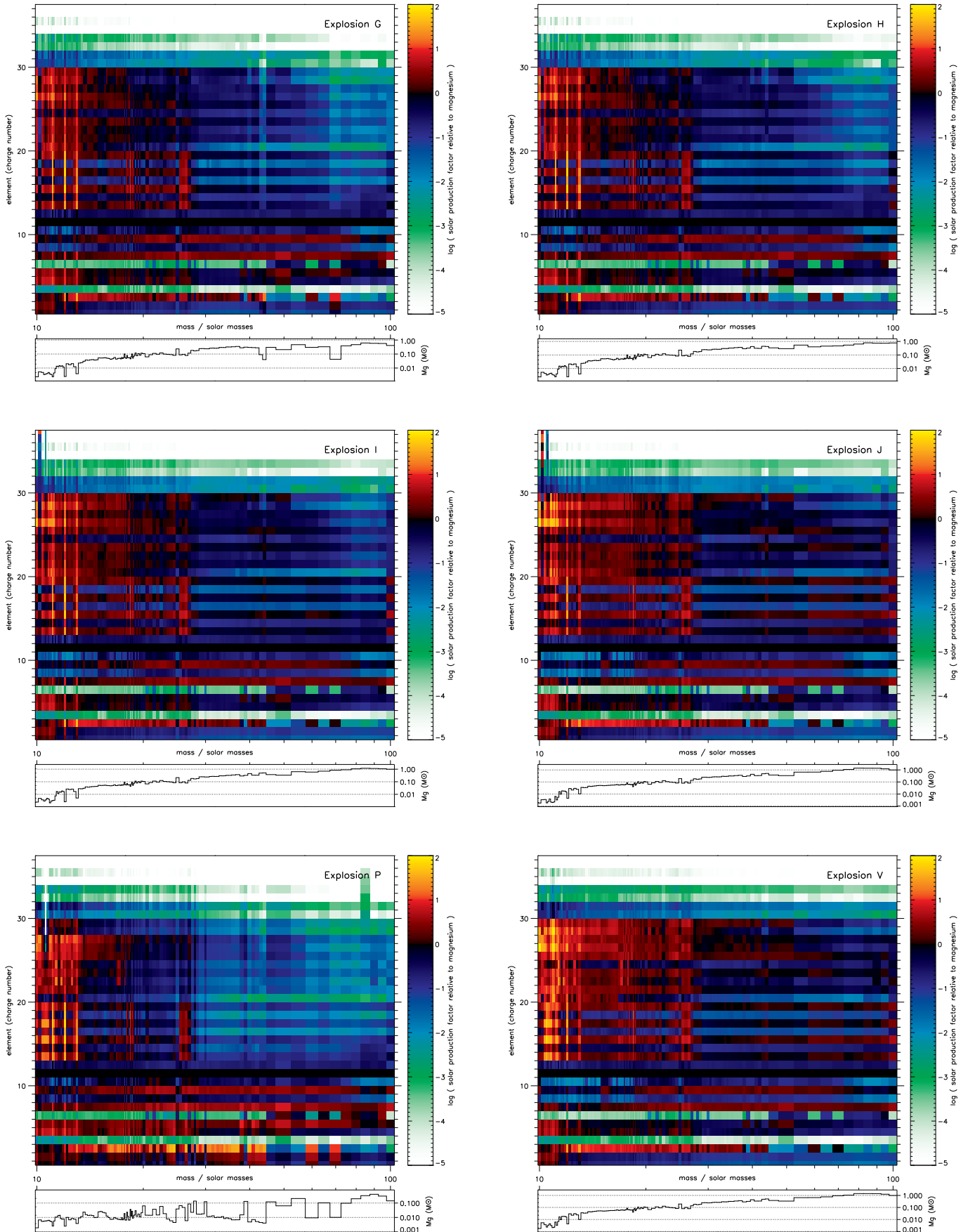


FIG. 10.— (CONTINUED) Production factors as a function of mass for the 2.4–10 B explosions (Explosion Models G–J), and the 1.2 B and 10 B explosions with pistons located at the edge of the deleptonized core (Explosion Models P and V).

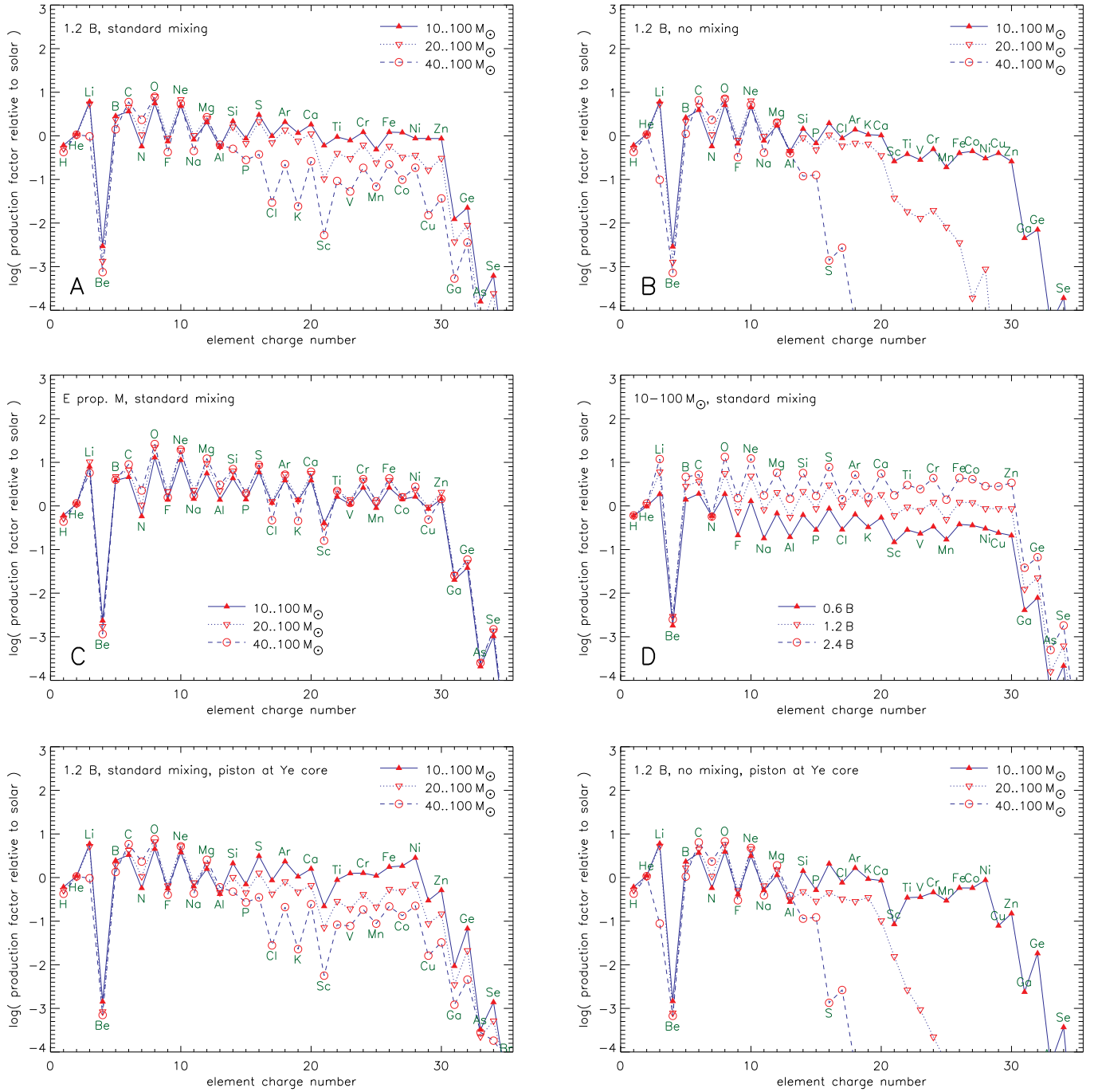


FIG. 11.— IMF integral production factors using the Salpeter IMF with slope with $\Gamma = 1.35$. **Panel A:** Standard mixing of 0.1, 1.2 B explosions, low-mass cut-offs for IMF at 10, 20, and 40 M_{\odot} , $S = 4k_B/\text{baryon}$. **Panel B:** No mixing, 1.2 B explosions, low-mass cut-offs for IMF at 10, 20, and 40 M_{\odot} , $S = 4k_B/\text{baryon}$. Explosion energy is $1.2B \times M/20M_{\odot}$. **Panel C:** Standard mixing of 0.1, 1.2 B explosions, low-mass cut-offs for IMF at 10, 20, and 40 M_{\odot} , $S = 4k_B/\text{baryon}$. **Panel D:** Standard mixing of 0.1, low-mass cut-offs for IMF at 10–100 M_{\odot} , $S = 4k_B/\text{baryon}$. Constant explosion energies of 0.6, 1.2, and 2.4 B. **Panel E:** Standard mixing of 0.1, 1.2 B explosions, low-mass cut-offs for IMF at 10, 20, and 40 M_{\odot} , Y_e core piston. **Panel F:** No mixing, 1.2 B explosions, low-mass cut-offs for IMF at 10, 20, and 40 M_{\odot} , Y_e core piston.

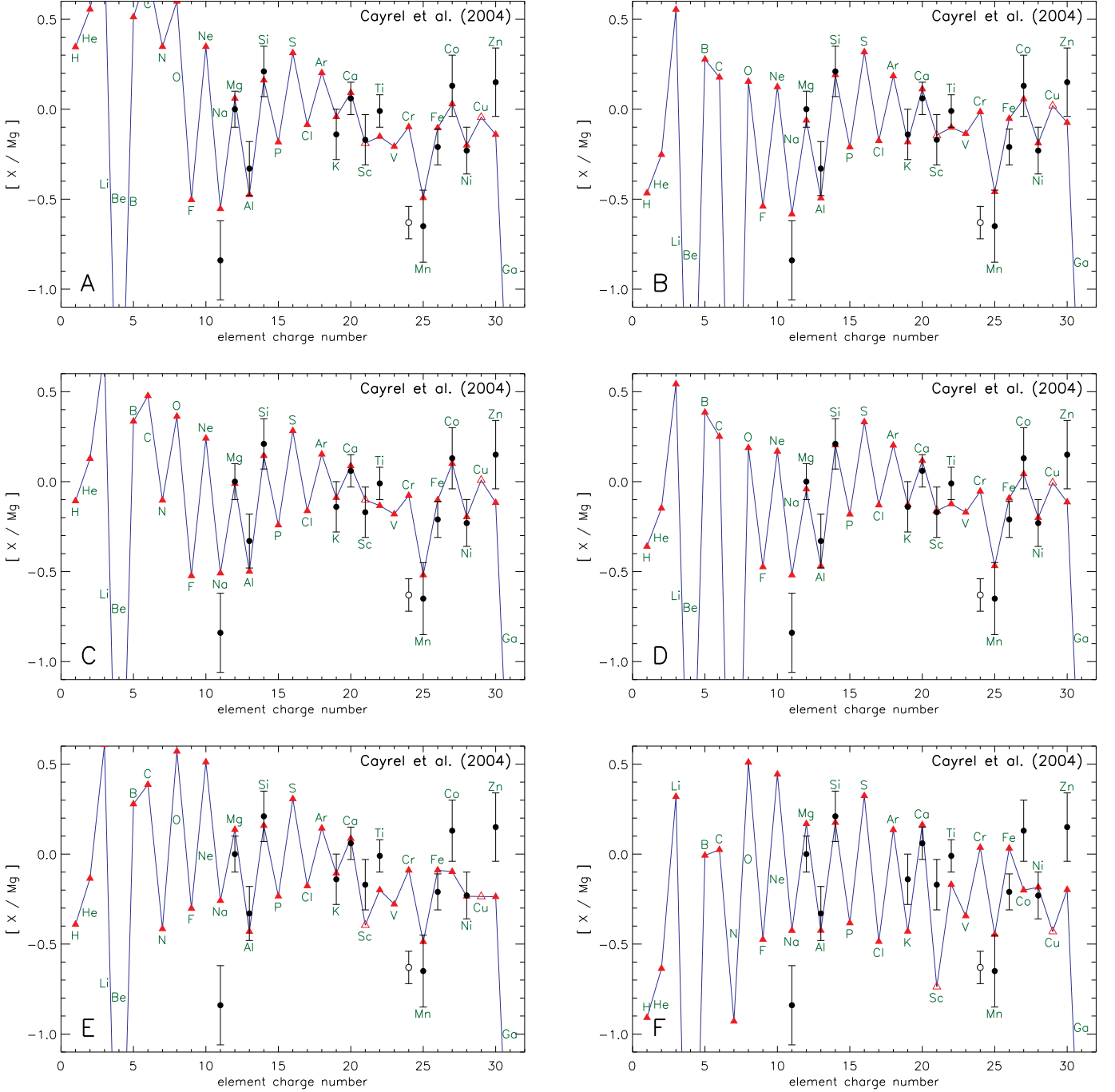


FIG. 12.— Fits to Cayrel et al. (2004). Cr is ignored (*hollow circle*). Cu (no data from by Cayrel et al.) and Sc may have other nucleosynthesis contributions and we treat them only as theoretical lower limits (*hollow triangles*). A list of fits and their properties is given in Table 17. **Panel A:** Gauss IMF fit with $M = 11.0 M_{\odot} \pm 0.3$ dex (truncated at $10 M_{\odot}$), $E = 0.6$ B, $E^{\text{exp}} = -1$, mixing = 0.0398, $\chi = 0.824$. **Panel B:** Best power-law IMF fit with $M = 11 - 15 M_{\odot}$, $\Gamma = -.650$, $E = 0.9$ B, $E^{\text{exp}} = -1$, mixing = 0.0158, $\chi = 0.732$ (overall best fit). **Panel C:** Best power-law IMF fit with fixed mass range and IMF power-law exponent: $M = 10 - 100 M_{\odot}$, $\Gamma = 1.35$, $E = 0.9$ B, $E^{\text{exp}} = -1$, mixing = 0.0158, $\chi = 0.753$ (overall best fit). **Panel D:** Best power-law IMF fit with fixed explosion energy: $M = 10 - 15 M_{\odot}$, $\Gamma = -0.65$, $E = 1.2$ B, $E^{\text{exp}} = 0$, mixing = 0.0158, $\chi = 0.740$ (overall best fit). **Panel E:** “Standard” IMF fit: $M = 10 - 100 M_{\odot}$, $\Gamma = 1.350$, $E = 1.2$ B, $E^{\text{exp}} = 0$, mixing = 0.1, $\chi = 1.695$. **Panel F:** High explosion energy case; IMF fit with fixed mass-dependent energy, full mass range and Salpeter IMF (mixing was allowed to float): $M = 10 - 100 M_{\odot}$, $\Gamma = 1.350$, $E = 1.8$ B, $E^{\text{exp}} = 1$, mixing = 0.1, $\chi = 2.287$.

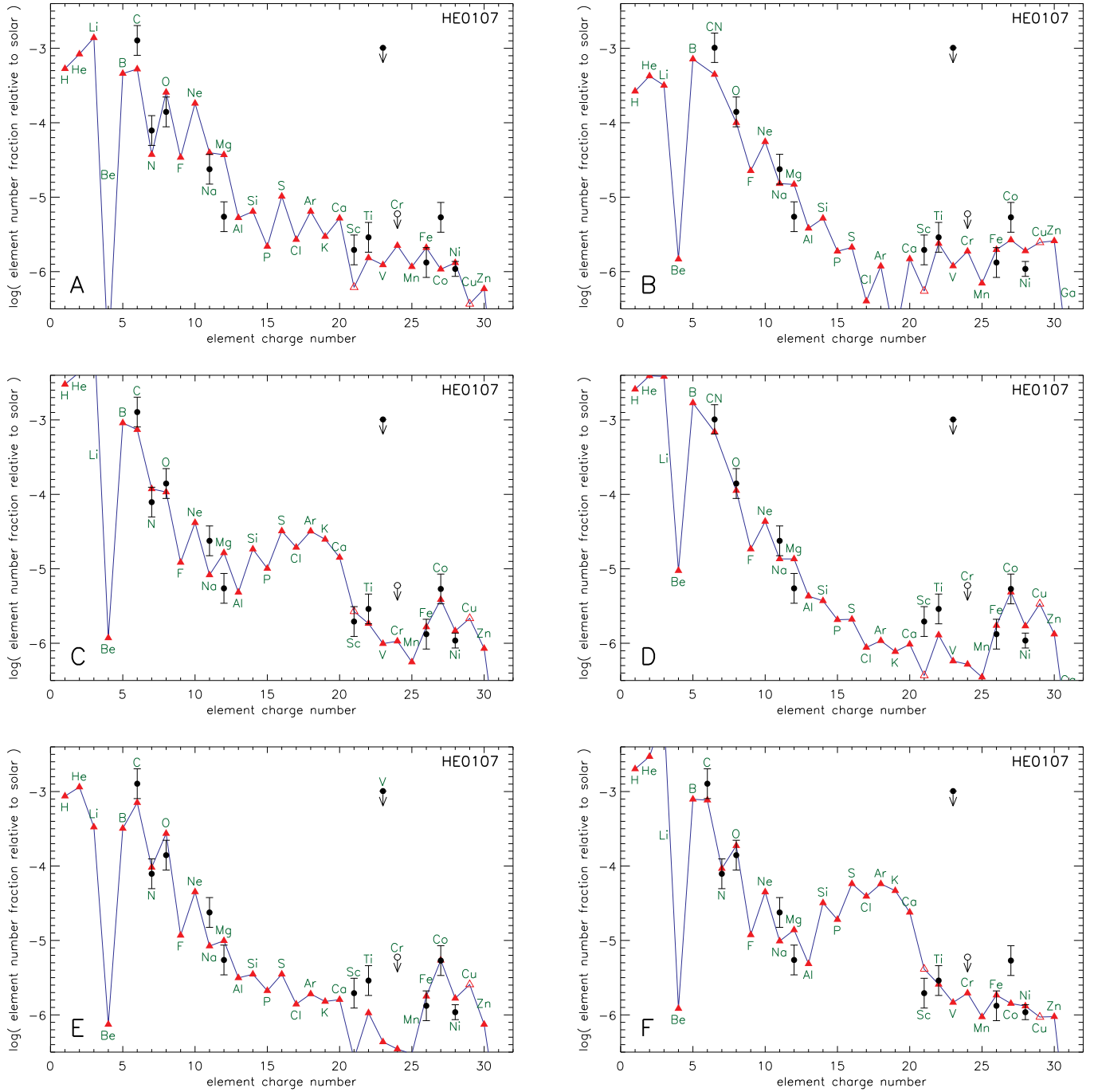


FIG. 13.— Fits to HE0107-5240 (Christlieb et al. 2007). Cr is ignored (*hollow circle*), but its upper limit is always above the fits shown. Cu (no data from HE0107) and Sc may have other nucleosynthesis contributions and we treat them only as theoretical lower limits (*hollow triangles*). A list of fits and their properties is given in Table 17. **Panel A:** Best single stars fit: $M = 20.5 M_{\odot}$, $E = 0.6 B$, $\text{mixing} = 0.0631$, $\chi = 3.845$. **Panel B:** Best single stars fit combining C+N: $M = 10.5 M_{\odot}$, $E = 0.3 B$, $\text{mixing} = 0.0063$, $\chi = 1.856$. Combining C+N+O does not give a better fit. **Panel C:** Gauss IMF fit with $M = 17 M_{\odot} \pm 0.1 \text{ dex}$, $E = 0.6 B$, $E^{\text{exp}} = 1.0$, $\text{mixing} = 0.0025$, $\chi = 1.571$. **Panel D:** Gauss IMF fit combining C+N with $M = 12 M_{\odot} \pm 0.025 \text{ dex}$, $E = 0.3 B$, $E^{\text{exp}} = 0.0$, $\text{mixing} = 0.0040$, $\chi = 1.359$. Combining C+N+O does not give a better fit. **Panel E:** IMF fit with $M = 10 - 40 M_{\odot}$, $\Gamma = -0.65$, $E = 0.3 B$, $E^{\text{exp}} = 1.0$, $\text{mixing} = 0.004$, $\chi = 1.752$. Combining C+N does not give a better fit, combining C+N+O gives allows a slightly better fit. **Panel F:** IMF fit with $M = 12 - 30 M_{\odot}$, $\Gamma = 1.350$ (Salpeter), $E = 0.6 B$, $E^{\text{exp}} = 1.0$, $\text{mixing} = 0.0251$, $\chi = 1.974$.

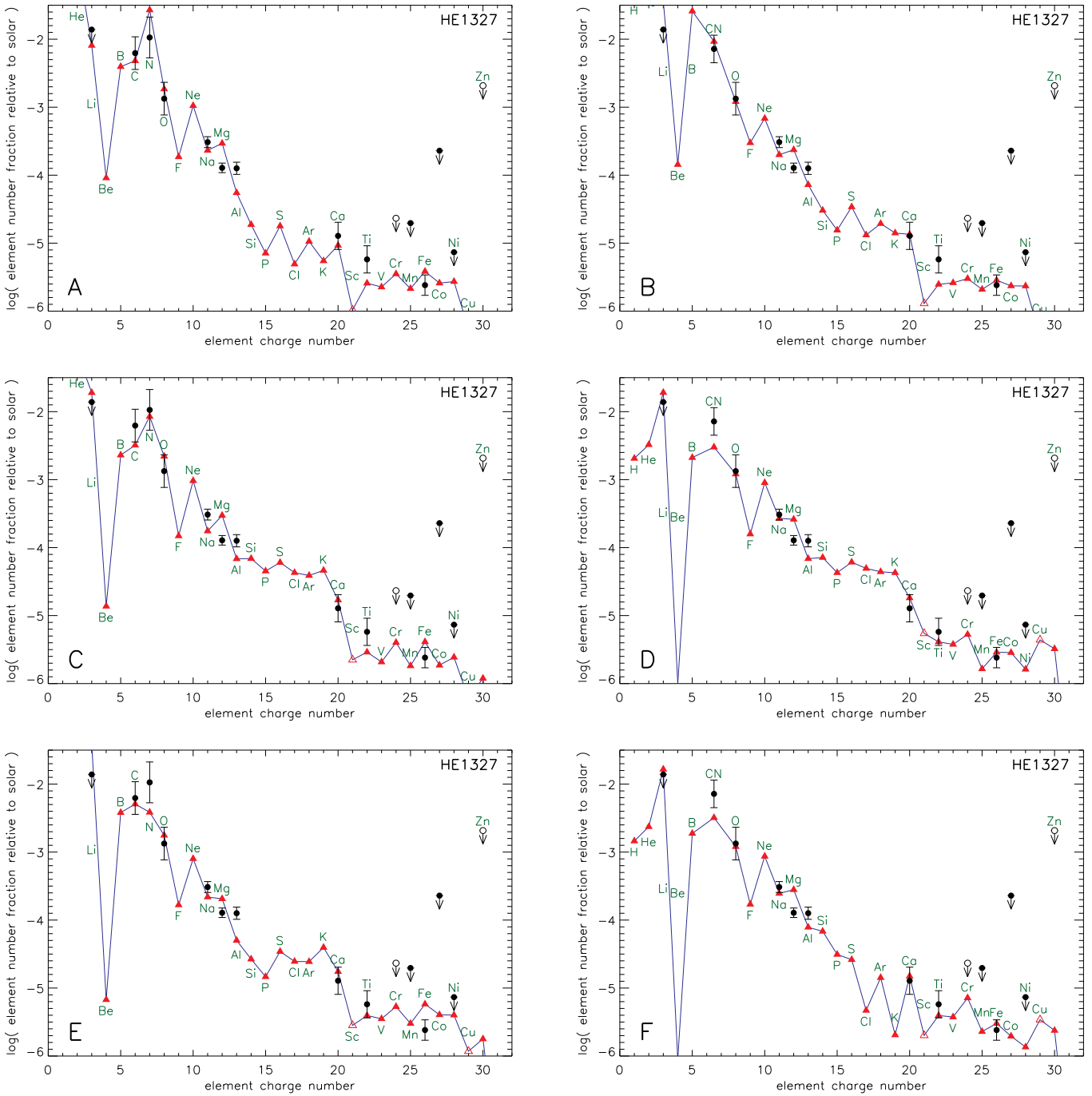


FIG. 14.— Fits to HE1327 (Aoki et al. 2006; Frebel et al. 2006). Cr and Zn are ignored, but their upper limit is always above the fits shown. Cu and Sc (both no data from HE1327) may have other nucleosynthesis contributions and we treat them only as theoretical lower limits (*hollow triangles*). A list of fits and their properties is given in Table 17. **Panel A:** Best single stars fit: $M = 21.5 M_{\odot}$, $E = 0.3 B$, $\text{mixing} = 0.0631$, $\chi = 4.051$. **Panel B:** Best single stars fit combining C and N: $M = 11.6 M_{\odot}$, $E = 0.3 B$, $\text{mixing} = 0.0158$, $\chi = 2.941$. Combining C+N+O does not allow a better fit than just combining C+N. **Panel C:** Gauss IMF fit with $M = 25.0 M_{\odot} \pm 0.05 \text{ dex}$, $E = 0.3 B$, $E^{\text{exp}} = 0.5$, $\text{mixing} = 0.0631$, $\chi = 4.072$. **Panel D:** Gauss IMF fit with $M = 15.0 M_{\odot} \pm 0.025 \text{ dex}$, $E = 0.9 B$, $E^{\text{exp}} = 0.5$, $\text{mixing} = 0.0063$, $\chi = 2.833$. Combining C+N+O does not find a better match than just combining C+N. **Panel E:** IMF fit with $M = 15 - 40 M_{\odot}$, $\Gamma = 1.350$, $E = 0.3 B$, $E^{\text{exp}} = -1.0$, $\text{mixing} = 0.0398$, $\chi = 3.620$. **Panel F:** IMF fit with $M = 13.5 - 17 M_{\odot}$, $\Gamma = 1.350$, $E = 0.9 B$, $E^{\text{exp}} = 0.0$, $\text{mixing} = 0.0040$, $\chi = 2.892$. Combining C+N+O does not allow a better fit than just combining C+N.

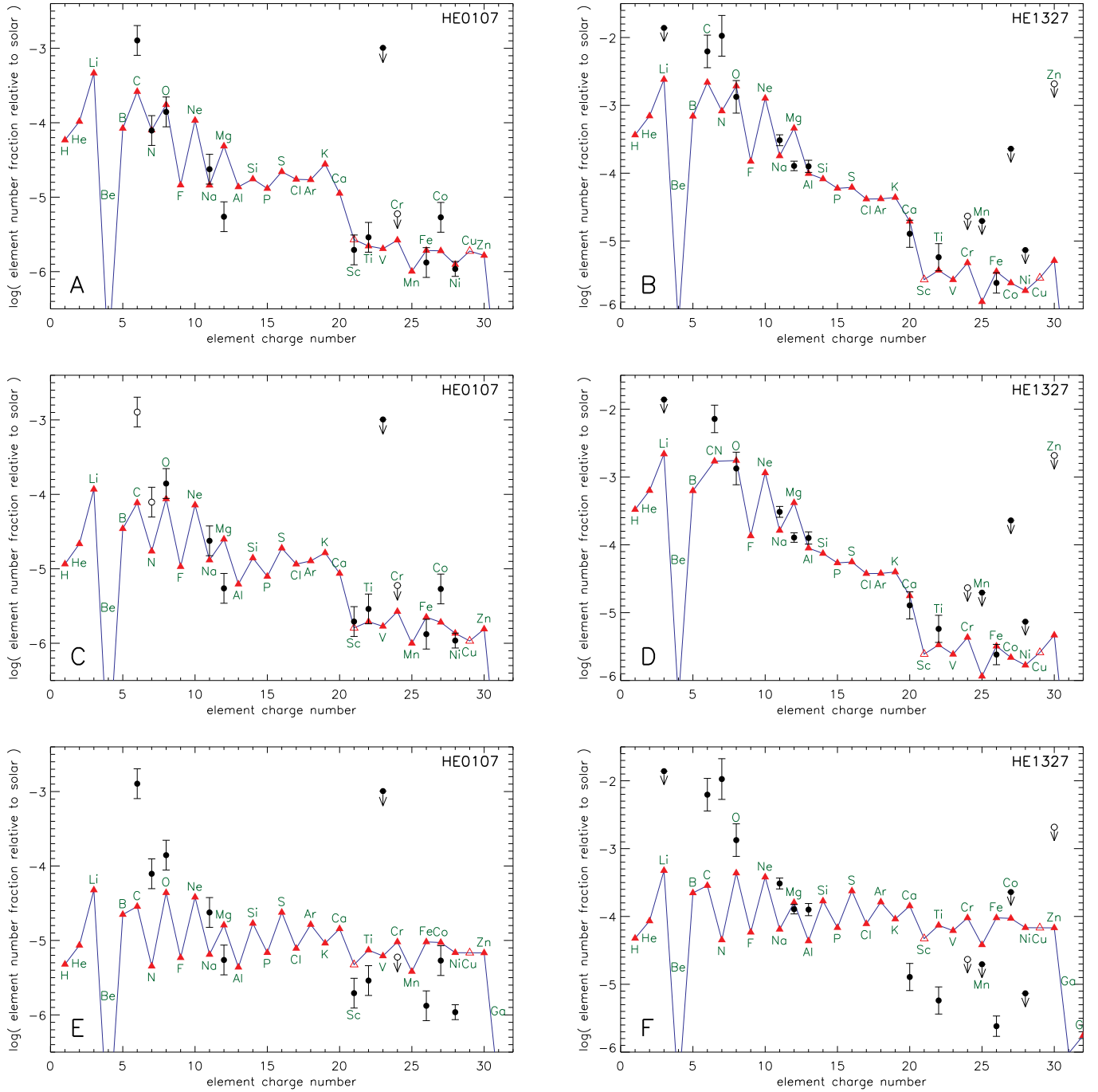


FIG. 15.— Fits with upper mass limit fixed to $100 M_{\odot}$ and fixed $\Gamma = 1.350$ for HE0107-5240 (Christlieb et al. 2007) (Panels A, C, and E) and HE1327-2326 (Aoki et al. 2006; Frebel et al. 2006) (Panels B, D, and F). For comparisons for the “standard” IMF, mixing, and energies are given in Panels E and F for HE0107 and HE1327 respectively. Cr is ignored, but except for the poor “standard” fits its upper limit is always above the fits shown here present. Cu and Sc (both no data from HE1327) may have other nucleosynthesis contributions and we treat them only as theoretical lower limits (hollow triangles). A list of fits and their properties is given in Table 17. **Panel A:** HE0107. IMF fit with $M = 13.5 - 100 M_{\odot}$, $\Gamma = 1.350$, $E = 0.9 B$, $E^{\text{exp}} = -0.5$, mixing = 0.0158, $\chi = 3.870$. Combining C+N or C+N+O does not allow better fits. **Panel B:** HE1327. IMF fit with $M = 20 - 100 M_{\odot}$, $\Gamma = 1.350$, $E = 1.2 B$, $E^{\text{exp}} = -1.0$, mixing = 0.0158, $\chi = 7.189$. Combining C+N or C+N+O gives $\chi \approx 0.5$ better fits. **Panel C:** HE0107. Ignoring carbon and nitrogen. IMF fit with $M = 15 - 100 M_{\odot}$, $\Gamma = 1.350$, $E = 1.2 B$, $E^{\text{exp}} = -0.5$, mixing = 0.01, $\chi = 2.399$. **Panel D:** HE1327. Combining C+N. IMF fit with $M = 20 - 100 M_{\odot}$, $\Gamma = 1.350$, $E = 1.2 B$, $E^{\text{exp}} = -1.0$, mixing = 0.0158, $\chi = 6.699$. Combining C+N+O improves the best fit found only slightly. **Panel E:** HE0107. “Standard” IMF and energies: $M = 10 - 100 M_{\odot}$, $\Gamma = 1.350$, $E = 1.2 B$, $E^{\text{exp}} = 0.0$, mixing = 0.1, $\chi = 19.809$. **Panel F:** HE1327. “Standard” IMF and energies: $M = 10 - 100 M_{\odot}$, $\Gamma = 1.350$, $E = 1.2 B$, $E^{\text{exp}} = 0.0$, mixing = 0.1, $\chi = 30.341$.